ISEL
INSTITUTO SUPERIOR DE ENGENHARIA DE LISBOA
DEPARTAMENTO DE ENGENHARIA QUÍMICA

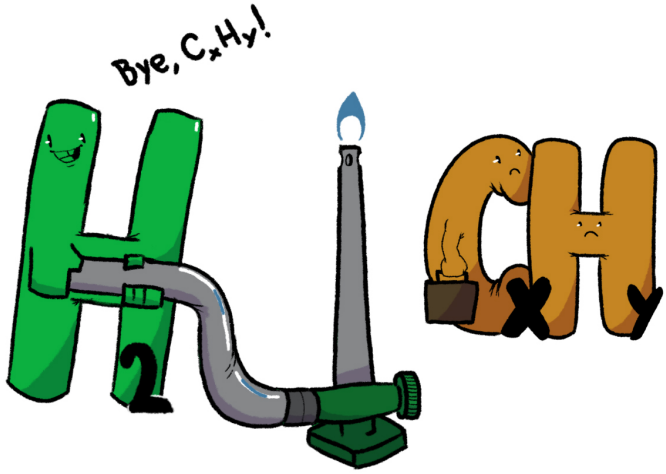

Premixed Hydrogen Combustion: Kinetic Predictions of Flame Behaviour

AILTON DONADONY FERNANDES GONÇALVES
(Licenciado em Engenharia Química e Biológica)

Trabalho Final de Mestrado para Obtenção do Grau de
Mestre em Engenharia Química e Biológica

Orientador:

Doutor Teodoro José Pereira Trindade

Júri:

Presidente: Doutor José Augusto Paixão Coelho

Vogais:

Doutor Teodoro José Pereira Trindade

Doutor Jaime Filipe Borges Puna

Doutor Rui Manuel Gouveia Filipe

Setembro 2022

From left to right: Jaime Puna (1^{st} arguer), José Coelho (President), Ailton Gonçalves (Candidate), Teodoro Trindade (Advisor) and Rui Filipe (2^{nd} arguer).

Success does not consist in never making mistakes
but in never making the same one a second time.
George Bernard Shaw

Acknowledgments

First of all, I want to thank God for all he gave and is giving me for my entire life. I'm grateful for the reception and continuous support from all the people who were with me since my arrival in ISEL. With you I laughed, I learned and grew up. Your friendships are precious and I really appreciated the time we've spent together. If you are reading this, know that you all are good friends.

I would like to thank Instituto Superior de Engenharia de Lisboa (ISEL) for the entire journey. These were years of many learnings that I am proud to say made me a more critical person and that will help me in the future.

A special acknowledgments to Professor Teodoro Trindade for his objective guidance and for his understanding way, giving me all the necessary support so that I could carry out this work.

A special thanks to Nathan Demoliner for taking the time to helping me with some algorithms in MATLAB and Maria Carolina Sequeira for making available for me the software TableCurve and helping with the development of the empirical equation.

I would like to thank all the people who were by my side during this course in the Master's, especially my close friends Patrícia Duarte, Joana Fernandes, Daniela Santos, Juliana Santos, Joana Pereira, my great friend Diogo Martins and my work partner and great advisor Bianca Moraes.

Special acknowledgments to my laboratory friend Tiago Cabrita and everyone I worked with at the Chemical Technology Laboratory, whether professors or my students. A big thank you to Professor Jaime Puna for the opportunity to have worked during this period at LTQ and for all his advice.

A huge thanks to my girlfriend Sofia Pinto who supported me for all this time and gave me all her love. I want to thank my family for all the support through my entire life. Without them I wouldn't be able to be where I am. I want to thank my parents for supporting my decision to move to Portugal and for all the effort they have made to make me more and more, a person richer in knowledge and humility. A special thank to my brother, for never letting me down, making jokes and being the best company since the beginning.

Resumo

Neste trabalho final de mestrado, pretendeu-se analisar a envolvente do hidrogénio como um portador de energia e combustível, com ênfase nas suas propriedades de combustão, análise aos radicais e espécies químicas, em misturas com outras espécies, nomeadamente metano (CH_4), dióxido de carbono (CO_2) e gás natural (NG). Os estudos foram feitos através de simulações numéricas, com os mecanismos cinéticos GRI-MECH 3.0, San Diego Mech, Qin Mech, AramcoMech_1.3 e Boivin Mech, realizadas no ambiente de programação *Python*, recorrendo a biblioteca *Cantera*. Foram realizados estudos sobre a temperatura adiabática de chama (T_b), a velocidade da chama laminar (S_L) e da estabilidade de chama e limites de operação. Estudou-se a influência de 4 parâmetros, composição do combustível, razão de equivalência (ϕ), temperatura da pré-mistura com ar (T_u) e a pressão do sistema (P). Observou-se comportamentos similares entre a temperatura adiabática de chama e a velocidade de chama relativamente à razão de equivalência, onde o valor máximo é alcançado na zona rica de mistura. Para a influência da temperatura da pré-mistura, observou-se que o seu acréscimo gera um aumento em T_b e S_L, enquanto o aumento da pressão gera um aumento na temperatura adiabática e um decréscimo na velocidade de chama. Quando se utilizam misturas de H_2 com CH_4 e CH_4/CO_2, observa-se que tanto a temperatura adiabática quanto a velocidade da chama apresentam decréscimos e seus valores máximos se aproximem da estequiometria. Foram propostas equações empíricas para descrever a temperatura adiabática das chamas de hidrogénio puro em função da razão de equivalência, temperatura da pré-mistura e pressão. Em relação à estabilidade de chama e limites de operação, avaliou-se a influência do teor em H_2 numa mistura de gás natural enriquecido com hidrogénio (HENG). Resultados mostram um acréscimo na estabilidade das chamas pela adição de H_2.

Palavras chave

Combustão do hidrogénio; Temperatura adiabática de chama; Velocidade de chama laminar; Mecanismos de combustão; Mistura de combustível.

Abstract

In this final master's work, it was intended to analyze the involvement of hydrogen as an energy carrier and fuel, with emphasis on its combustion properties, analysis to radicals and chemical species, in mixtures with other species, namely methane (CH_4), carbon dioxide (CO_2) and natural gas (NG). The studies were carried out through numerical simulations, with the kinetic mechanisms GRI-MECH 3.0, San Diego Mech, Qin Mech, AramcoMech_1.3 and Boivin Mech, performed in the programming environment *Python*, using the library *Cantera*. Studies were performed on the adiabatic flame temperature (T_b), the laminar flame speed (S_L) and the flame stability and operating limits. The influence of 4 parameters, fuel composition, equivalence ratio (ϕ), premix temperature with air (T_u) and the system pressure (P) were studied. Similar behaviour was observed between adiabatic flame temperature and flame speed with respect to the equivalence ratio, where the maximum value is reached in the rich mixing zone. For the influence of the premix temperature, it was observed that its increase generates an increase in T_b and S_L, while the increase in pressure generates an increase in adiabatic temperature and a decrease in flame speed. When using mixtures of H_2 with CH_4 and CH_4/CO_2, it is observed that both adiabatic temperature and flame speed show decreases, and their maximum values approach the stoichiometry. Empirical equations have been proposed to describe the adiabatic temperature of pure hydrogen flames as a function of equivalence ratio, premix temperature and pressure. Regarding flame stability and operating limits, the influence of H_2 content in a hydrogen-enriched natural gas (HENG) blend was evaluated. Results show an increase in flame stability by the addition of H_2.

Keywords

Hydrogen combustion; Adiabatic flame temperature; Laminar flame speed; Combustion mechanisms; Fuel blends

Symbology and Abbreviations

Latin symbology

A	[cm,mol,s]	Pre-exponential factor
a_{ij}	$[\mathrm{kg\,atom_i\,kg\,mol_j^{-1}}]$	Stoichiometric coefficient
b_i^0	$[\mathrm{kg\,atom_i\,kg^{-1}}]$	Assigned mass of atoms per mass of total reactant
b	[–]	Temperature exponent
C_p	$[\mathrm{J\,mol^{-1}\,K^{-1}}]$	Specific molar heat capacity
d	[m]	Diameter
D	$[\mathrm{m^2\,s^{-1}}]$	Diffusion coefficient
D^T	$[\mathrm{m^2\,s^{-1}}]$	Thermal diffusion coefficient
E_a	$[\mathrm{J\,mol^{-1}}]$	Activation energy
g_B	$[\mathrm{s^{-1}}]$	Blowoff gradient
g_F	$[\mathrm{s^{-1}}]$	Flashback gradient
g_j	$[\mathrm{J\,kmol_j^{-1}}]$	Chemical potential of species j
G	$[\mathrm{kJ\,mol^{-1}}]$	Gibbs free energy
H	$[\mathrm{kJ\,mol^{-1}}]$	Molar entalphy
k_f	[cm,mol,s]	Forward rate constant
n_j	[–]	Number of moles
P	[Pa] or [atm]	Pressure
R	$[\mathrm{J\,mol^{-1}\,K^{-1}}]$	Ideal gas constant
R_f	$[\mathrm{dm^3, mol, s}]$	Forward reaction rate
S	$[\mathrm{J\,mol^{-1}\,K^{-1}}]$	Molar entropy
S_L	$[\mathrm{m\,s^{-1}}]$	Laminar flame speed
T	[K]	Temperature
u_{av}	$[\mathrm{m\,s^{-1}}]$	Unburned gas average speed
Z_{rot}	[–]	Rotational relaxation number at 298 K

Greek symbology

ϕ	[–]	Equivalence ratio
Δ	[–]	Variation
μ	$[\mathrm{kg\,m^{-1}\,s^{-1}}]$	Dynamic viscosity
ν	$[\mathrm{m^2\,s^{-1}}]$	Kinematic viscosity
γ	$[\mathrm{W\,m^{-1}\,K^{-1}}]$	Thermal conductivity
ε/k_B	[K]	Lennard-Jones energy potential
σ	[Å]	Lennard-Jones collision diameter
η	[Debye]	Dipole moment
α	$[\mathrm{Å}^3]$	Polarizability or angle

Subscripts

$_{st}$	Stoichiometric
$_T$	Reference temperature
$_f$	Formation with entalphy/ Forward with rate constant or reaction rate
$_{298}$	Temperature of 298 K
$_b$	Burned (In the case of this work, adiabatically)
$_u$	Unburned
$_i$	Atom i
$_j$	Species j
$_{max}$	Maximum
$_{norm}$	Normalized
$_\infty$	High collision partner concentration
$_0$	Low collisin partner concentration

Superscripts

$^\circ$	Standard condition
^{T}	Thermal
$_L$	Laminar

Chemical symbology

CH_4	Methane
CO	Carbon monoxide
CO_2	Carbon dioxide
H	Hydrogen radical
H_2	Molecular hydrogen
H_2O	Water
HO_2	Hydroperoxyl radical
H_2O_2	Hydrogen peroxide
N_2	Molecular nitrogen
O	Oxygen radical
O_2	Molecular oxigen
OH	Hydroxide radical
Y	Collision partner

Abbreviations

ATR	Autothermal reforming
BDLR	Bio-derived liquids reforming
CCH	Cryo-compressed hydrogen
CH2	Compressed hydrogen
CNG	Compressed natural gas
COF	Covalent organic framework
COP21	21^{st} Conference of the Parties
ESRL	Earth System Research Laboratories
EU27+UK	Europe 27 countries + United Kingdom
GHG	Greenhouse gases
HDPE	High-density polyethylene
HENG	Hydrogen enriched natural gas
LH2	Liquid hydrogen
LHV	Lower heating value
LNG	Liquid natural gas
LOHC	Liquid organic hydrogen carriers
MEC	Microbial electrolysis cells
MOF	Metal organic framework
NASA	National Aeronautics and Space Adminstration
NG	Natural gas
NOAA	National Oceanic and Atmospheric Administration
N_{Re}	Reynolds number
NUI	National University of Ireland
P2G	Power-to-gas
PEM	Polymer membrane
PIM	Polymers of intrinsic micro-porosity
POX	Partial oxidation
RNC2050	Roadmap for Carbon Neutrality 2050
SHS	Self-propagating high-temperature synthesis
SOE	Solid oxide electrolyzers
SWCN	Single wall carbon nanotube
SR	Steam reforming
USD	United States Dollar

Contents

Contents xv

List of Figures xvii

List of Tables xxiii

1 Introduction 1

1.1 Framework . . . 1
1.2 Motivation . . . 4
1.3 Objective . . . 4
1.4 Thesis structure . . . 4

2 Overview 7

2.1 A brief introduction . . . 7
2.2 Production of hydrogen fuel . . . 7
2.3 Storage of hydrogen . . . 9
2.4 Transport of hydrogen . . . 14
2.5 End use of hydrogen . . . 17
2.6 Combustion . . . 18
2.7 Flame types . . . 19
2.8 Combustion stoichiometry . . . 20

3 Methodology 23

3.1 Combustion Kinetic . . . 23
3.1.1 GRI-MECH 3.0 . . . 23
3.1.2 San Diego Mech . . . 24
3.1.3 Qin Mech . . . 26
3.1.4 AramcoMech_1.3 . . . 26
3.1.5 Boivin Mech . . . 27
3.1.6 Thermodynamics data . . . 30
3.1.7 Species reactivity . . . 31
3.1.8 Transport data . . . 33

3.2 Adiabatic flame temperature . . . 34
3.3 Laminar flame speed . . . 35
3.4 Flame stability and operation limits . . . 37
3.5 Cantera . . . 39
3.6 Algorithm 1: Adiabatic flame temperature . . . 39
3.7 Algorithm 2: Laminar flame speed . . . 40
3.8 Algorithms 3 and 4: Density and viscosity . . . 42

4 Results and discussion **45**
4.1 Adiabatic flame temperature . . . 45
4.1.1 Equivalence ratio . . . 45
4.1.2 Mechanism exploited . . . 47
4.1.3 Pressure . . . 49
4.1.4 Unburned gas temperature . . . 50
4.1.5 Aggregate effect of pressure and unburned gas temperature . . . 53
4.1.6 Methane flames . . . 56
4.1.7 $CH_4/H_2/CO_2$ fuel blends . . . 61
4.1.8 Empirical equations . . . 66
4.2 Laminar flame speed . . . 73
4.2.1 Numerical code coefficients . . . 73
4.2.2 Kinetic mechanism validation . . . 74
4.2.3 Effect of pressure . . . 76
4.2.4 Effect of unburned gas temperature . . . 77
4.2.5 Methane flames . . . 78
4.2.6 Fuel blends of $H_2/CH_4/O_2/N_2$ . . . 80
4.3 Flame stability . . . 82
4.3.1 Natural gas flame . . . 82
4.3.2 Hydrogen enriched natural gas flame . . . 83

5 Conclusions and future work **87**
5.1 Conclusions . . . 87
5.2 Future work . . . 89

A Work Disclosure **91**

Bibliography **93**

List of Figures

1.1 Average atmospheric CO_2 concentration in ppm at the ground level. Source: Friedlingstein *et al.* . . . 2

1.2 Fossil CO_2 emission of the major emitting economies. Source: European Commission report. . . . 2

1.3 Fossil CO_2 emission in Portugal by sector of economy. Bars are refereed to the left axis. Lines are refereed to right axis. Source: European Commission report. . . . 3

1.4 Hydrogen as a energy vector in Portugal, opportunities and goals. Source: Secretaria de Estado Adjunta e da Energia. . . . 3

2.1 Main production sources of hydrogen, 2006 worldwide data. Adapted from Khotari *et al.* . . . 9

2.2 List of actual H_2 storage technology types. Adapted from Moradi *et al.* . . . 10

2.3 Type IV vessel for hydrogen gas storage. Source: Gerboni *et al.* . . . 11

2.4 Linde-Hampson cycle used for H_2 liquefaction. Source: Ratnakar *et al.* . . . 12

2.5 Hydrogen tube trailer vessel for road transport (Type I). Source: Gerboni *et al.* . . . 15

2.6 Kawasaki prototype of ocean transportation of hydrogen fuel. Source: Gerboni *et al.* . . . 16

2.7 Pipeline steel embrittlement caused by operation with molecular hydrogen. Source: Iannuzzi *et al.* . . . 16

2.8 Examples of flame types for gas fuels. Source: Ahmed PhD thesis. . . . 20

3.1 Representation of ln (k) vs 1/T using the kinetic data from GRI-MECH 3.0, San Diego Mech, AramcoMech_1.3 and Boivin Mech for two H_2/O_2 combustion reactions. . . . 29

3.2 Thermodynamic data extracted from AramcoMech_1.3. First set of 7 constants (lines 2 and 3) belongs to the 1000-6000 K interval, the second set of 7 constants (lines 3 and 4) belongs to the 200-1000 K interval. Last constant is the value of $\Delta_f H_{298}/R$. . . . 31

3.3 Elements and species representation in GRI-MECH 3.0. 31
3.4 Collection of reaction data with reaction blueprint, stoichiometry and data used in Arrhenius equation. Extracted from GRI-MECH 3.0. A (cm, mol, s), b $(-)$, E_a $(\mathrm{cal\,mol^{-1}})$. 31
3.5 Falloff reaction specifications extracted from GRI-MECH 3.0 . Line 1 sets the equation. On line 2, k_f represents $k_{f\infty}$ and the three values on brackets are Arrhenius equation parameters with high Y concentration Line 3 sets the values from Arrhenius equation with low Y concentration. Line 4 sets troe parameters and line 5 the collision partners efficiencies. 33
3.6 Laminar flame speed equals normal component of unburned gas velocity (u_{av}). Adapted from Turns *et al.* 36
3.7 Example of a laminar flat-flame burner. Source: Kee *et al.* 36
3.8 Representation of numerical solution by mesh refining. 37
3.9 Glassman stability diagram highlights the operation limits of Bunsen burner. 38

4.1 GRI-MECH 3.0 mechanism: effect of premixture equivalence ratio in adiabatic flame temperature of $H_2/O_2/N_2$ flames at 1 atm and 300 K. 46
4.2 GRI-MECH 3.0 mechanism: concentration of selected radicals in burned gas of $H_2/O_2/N_2$ flames at 1 atm and 300 K of unburned gas temperature. **(a)** Concentration of OH, H radicals (left axis) and O radical (right axis). **(b)** Concentration of HO_2 radical (left axis) and species H_2O_2 (right axis). 47
4.3 Adiabatic flame temperatures of $H_2/O_2/N_2$ flames (1 atm and 300 K of unburned gas temperature). Lines: kinetic simulation results using GRI-MECH 3.0, San Diego, AramcoMech_1.3, Boivin; Symbols: bibliographic reference data. 47
4.4 Comparison of radicals molar fraction between GRI-MECH 3.0, San Diego Mech, AramcoMech_1.3 and Boivin Mech. Conditions: $H_2/O_2/N_2$ flames at 1 atm and 300 K of unburned gas temperature. **(a)** OH radical. **(b)** H radical. 48
4.5 GRI-MECH 3.0 mechanism: effect of pressure (0.5 to 20 atm) in the adiabatic flame temperature of $H_2/O_2/N_2$ premixture, at 300 K of unburned gas temperature.. 49
4.6 GRI-MECH 3.0 mechanism: effect of pressure, from 0.5 to 20 atm in radicals molar fraction of $H_2/O_2/N_2$ premixed flames, at 300 K of unburned gas temperature. **(a)** OH radical. **(b)** H radical. **(c)** O radical. 50

4.7 GRI-MECH 3.0 mechanism: effect of unburned gas temperature (250 to 500 K), in the adiabatic temperature of $H_2/O_2/N_2$ flames at 1 atm. Normalization was performed by dividing flame temperature at any ϕ by the flame temperature at ϕ of 0.3. 51

4.8 GRI-MECH 3.0 mechanism: specific heat capacity of the burned gases of $H_2/O_2/N_2$ flames, $\phi = 1$ and 1 atm. 52

4.9 GRI-MECH 3.0 mechanism: effect of unburned gas temperature, ranging from 250 to 500 K, on $H_2/O_2/N_2$ premixture at 1 atm, on the burned gas concentration of: **(a)** OH radical. **(b)** O radical. **(c)** H radical. 53

4.10 GRI-MECH 3.0 mechanism: effect of pressure (up to 60 atm) on $T_{b.max}$ and ϕ_{max}, with an unburned gas temperature of 300 K, using a $H_2/O_2/N_2$ premixture. (●) $T_{b.max}$, (▼) ϕ_{max}, (- - -) fitting by equation (24) and (- - -) fitting by equation (25). 54

4.11 GRI-MECH 3.0 mechanism: effect of unburned gas temperature and pressure on the maximum adiabatic flame temperature, using a $H_2/O_2/N_2$ premixture. **(a)** Maximum flame temperature, **(b)** Equivalence ratio of maximum adiabatic flame temperature. 55

4.12 GRI-MECH 3.0 mechanism: effect of T_u and pressure on the rate of change in the lean ($0.3 < \phi < 0.75$) and rich ($1.2 < \phi$ 1.5) for a H_2/air premixture. **(a)** Rate of change on lean condition, **(b)** rate of change on rich condition. 56

4.13 GRI-MECH 3.0 mechanism: comparison between the adiabatic flame temperatures of CH_4/air and H_2/air premixtures, at 1 atm and premixture temperature of 300 K. 57

4.14 GRI-MECH 3.0 mechanism: effect of pressure and unburned gas temperature on the adiabatic flame temperature for $CH_4/O_2/N_2$ premixed flames. **(a)** Effect of pressure, **(b)** effect of unburned gas temperature. 58

4.15 GRI-MECH 3.0 mechanism: effect of pressure on radicals molar fraction for a $CH_4/O_2/N_2$ premixture, at 300 K of unburned gas temperature. **(a)** OH radical. **(b)** H radical. **(c)** O radical. 59

4.16 GRI-MECH 3.0 mechanism: effect of pressure on the burned gas concentration of CO_2 and CO for a $CH_4/O_2/N_2$ premixed flame and unburned gas temperature of 300 K. 60

4.17 GRI-MECH 3.0 mechanism: effect of unburned gas temperature on radicals fraction in burned gases for a $CH_4/O_2/N_2$ premixture, at 1 atm. **(a)** OH radical. **(b)** H radical. **(c)** O radical. 60

4.18 GRI-MECH 3.0 mechanism: effect of unburned gas temperature on the concentration of CO_2 and CO in the burned gases. for a $CH_4/O_2/N_2$ flame at 1 atm. 61

4.19 Adiabatic flame temperatures distribution of air premixed ternary fuel mixtures of $H_2/CH_4/CO_2$, at 1 atm and T_u = 300 K, under three equivalence ratio conditions: (a) lean, (b) stoichiometric, and (c) rich. Data computed using GRI-Mech 3.0. 63

4.20 Adiabatic flame temperature of $H_2/CH_4/CO_2$ fuel blends premixed with air at stoichiometric equivalence ratio. Effect of pressure and unburned gases temperature. 64

4.21 Comparison of adiabatic flame temperature at 300 K and 1 atm generated by GRI-MECH 3.0 and polynomials equation (26) to (29). (—) GRI-MECH 3.0, (- -) equation (26), (- -) equation (27), (- -) equation (28), (- -) equation (29). 67

4.22 Predictions of adiabatic flame temperature of $H_2/O_2/N_2$ flames, with the unburned gas temperature of 300 K, and 1 atm. (—) GRI-MECH 3.0, (- -) equation (29), (- -) equation (30). 69

4.23 Predictions of adiabatic flame temperature of $H_2/O_2/N_2$ premixture, with an unburned gas temperature from 300 to 500 K, at 1 atm. Continuous line (—) are data computed by GRI-MECH 3.0, dashed lines (- - -) are predictions from equation (30). 70

4.24 Effect of pressure, from 1 to 20 atm, on the adiabatic flame temperature, for $H_2/O_2/N_2$ flames, unburned gas temperatures from 300 to 500 K. **(a)** T_u = 300 K, **(b)** T_u = 400 K, **(c)** T_u = 500 K. Continuous line (—) are results from GRI-MECH 3.0, dashed lines (- - -) are results from equation (30). . 71

4.25 Mean and maximum deviations in the predictions of adiabatic temperature of $H_2/O_2/N_2$ flames between the values generated by kinetic calculations using GRI-MECH 3.0 and equation (30), ϕ = 1.0. **(a)** Mean temperature deviation (K), **(b)** maximum temperature deviation (K). 72

4.26 GRI-MECH 3.0 mechanism: effect of main numerical code coefficients on the computed values of laminar flame speed (normalized), for a $H_2/O_2/N_2$ flame, unburned gas temperature of 300 K, at 1 atm. Equivalence ratio of 0.7, 1.0 and 1.3. Coefficients tested: **(a)** Width, **(b)** Slope and **(c)** Curve. 74

4.27 Laminar flame speed, of $H_2/O_2/N_2$ flames with unburned gas temperature of 300 K, at 1 atm. Lines: kinetic simulation results. Symbols: bibliographic data. 75

4.28 GRI-MECH 3.0 mechanism: distribution of laminar flame speed and adiabatic flame temperature of $H_2/O_2/N_2$ flame, unburned gas temperature of 300 K, at 1 atm, where: (—) is the laminar flame speed (left axis) and (—) is the adiabatic flame temperature (right axis). 76

4.29 Effect of pressure, from 0.5 to 20 atm, on the laminar flame speed, using Boivin and GRI-MECH 3.0, for a $H_2/O_2/N_2$ flame, with unburned gas temperature of 300 K, in function of equivalence ratio, where: **(a)** ϕ and P vs S_L. **(b)** 0.5 atm comparison. Lines: kinetic simulation results. Symbols: bibliographic reference data. 77

4.30 GRI-MECH 3.0 mechanism: effect of unburned gas temperature (from 300 to 443 K), at 1 atm, using a $H_2/O_2/N_2$ premixture. Lines: kinetic simulation results. Symbols: bibliographic data. 78

4.31 Laminar flame speed of a $CH_4/O_2/N_2$ premixture, with an unburned gas temperature of 300 K, at 1 atm. Lines: kinetic simulation results. Symbols: published experimental data. 79

4.32 GRI-MECH 3.0 mechanism: comparison between the values of $\phi_{SL.max}$ and ϕ_{max}, from a premixture of $CH_4/O_2/N_2$, with an unburned gas temperature of 300 K, at 1 atm, where: (—) is the laminar flame speed (left axis) and (—) is the adiabatic flame temperature (right axis). 80

4.33 Laminar flame speed of a CH_4/H_2 (50/50 molar)$/O_2/N_2$ flame, using GRI-MECH 3.0, Qin Mech and San Diego Mech with an unburned gas temperature of 300 K at 1 atm. Lines: kinetic simulation results. Symbols: Bibliographic reference data. 80

4.34 Glassman diagram for a $CH_4/O_2/N_2$ flame, T_u of 300 K, 1 atm, at stoichiometry. Blue stripped area shows the stability limits; Grey solid area is the optimum area. 83

4.35 Compilation of Glassman diagrams for a HENG/air flame, T_u of 300 K, 1 atm. Equivalence ratio tested: 0.7, 1.0 and 1.3; H_2 content tested: 0.0, 20.0 and 40.0 %. Blue stripped area shows the stability limits; Grey solid area is the optimum area. 85

A.1 iFEQB 2020/2021 poster. 91

A.2 iFEQB 2021/2022 poster. 92

List of Tables

2.1 Hydrogen storage capacity of different construction materials. 13

2.2 Storage technologies of molecular hydrogen. Comparison of their main advantages and disadvantages. Source: Ma *et al.* 14

2.3 Selected applications of natural gas and hydrogen fuels. 18

2.4 Stoichiometric fuel/air ratios for different fuels. 21

3.1 $H_2/O_2/N_2$ reactions path, pre-exponential factor (A), temperature exponent (b) and activation energy (E_a) extracted from GRI-MECH 3.0. 23

3.2 $H_2/O_2/N_2$ reactions path, pre-exponential factor (A), temperature exponent (b) and activation energy (E_a) extracted from San Diego Mech. 25

3.3 $H_2/O_2/N_2$ reactions path, pre-exponential factor (A), temperature exponent (b) and activation energy (E_a) extracted from AramcoMech_1.3. 26

3.4 $H_2/O_2/N_2$ reactions path, pre-exponential factor (A), temperature exponent (b) and activation energy (E_a) extracted from Boivin Mech. 28

3.5 Values of A [cm,mol,s], b [-] and E_a [cal mol^{-1}] for GRI-MECH 3.0, San Diego Mech, AramcoMech_1.3 and Boivin Mech. 29

3.6 Transport data from kinetic mechanism, with the species molecular formula and the values of the constants needed to compute transport data. Adapted from CHEMKIN. 34

3.7 Default value of width, ratio, slope and curve from algorithm 3.2. 41

4.1 GRI-MECH 3.0 mechanism: computed data of $T_{b.max}$ and ϕ_{max}, of $H_2/O_2/N_2$ flames, for pressures of 0.5 to 20 atm, unburned gas temperature of 300 K. . 49

4.2 GRI-MECH 3.0 mechanism: maximum adiabatic flame temperatures and maximum adiabatic temperature equivalence ratio, using a $H_2/O_2/N_2$ premixture, unburned gas temperature in range of 250 to 500 K, at 1 atm. . . . 52

4.3 GRI-MECH 3.0 mechanism: computed data of $T_{b.max}$ and ϕ_{max}, of $CH_4/O_2/N_2$ flames, for pressures of 0.5 to 20 atm, unburned gas temperature of 300 K. . 58

4.4 Summary of results from section 4.1. 65

4.5 Coefficients a_0 to g_0 of equations (26) to (29), related errors (K) and values of $\Delta\phi_{max}$, for a premixed $H_2/O_2/N_2$ flame at 1 atm and unburned gas temperature of 300 K. 67

4.6 Coefficients a_n to g_n (n = 1 to 3) of equation (30), for a premixed $H_2/O_2/N_2$ flame. Values were tested for ϕ from 0.3 to 1.5, T_u from 250 to 500 K and pressure from 0.5 to 20 atm. 69

4.7 Numerical results of $S_{L.max}$, using Boivin Mech, San Diego Mech, GRI-MECH 3.0 and Qin Mech. $H_2/O_2/N_2$ flame, unburned gas temperature of 300 K at 1 atm. $\phi_{SL.max}$ obtained for all mechanisms was 1.65. 75

4.8 GRI-MECH 3.0 mechanism: values of $S_{L.max}$ ($m\,s^{-1}$) and $\phi_{SL.max}$, with unburned gas temperatures of 300, 373 and 443 K, at 1 atm, with a $H_2/O_2/N_2$ premixture. 78

4.9 Values of $S_{L.max}$ and $\phi_{SL.max}$ for different kinetic mechanisms, with a premixture of $CH_4/O_2/N_2$, unburned gas temperature of 300 K at 1 atm. . . . 79

4.10 Values of $S_{L.max}$ and $\phi_{SL.max}$ simulated by GRI-MECH 3.0, San Diego Mech, Qin Mech, for CH_4/H_2 (50/50 molar)$/O_2/N_2$ flame, unburned gas temperature of 300 K, at 1 atm. 81

4.11 Summary of results from section 4.2. 81

4.12 GRI-MECH 3.0 mechanism: simulation values of equivalence ratio, laminar flame speed, flashback and blowoff gradients, dynamic viscosity and density from the unburned gas mixture. Conditions: $CH_4/O_2/N_2$ flame, T_u = 300 K, at 1 atm. 82

4.13 GRI-MECH 3.0 mechanism: simulation values of equivalence ratio, H_2 content on HENG, laminar flame speed, flashback and blowoff gradients, dynamic viscosity and density from the unburned gas mixture. Conditions: HENG/air flame, T_u = 300 K, at 1 atm. 84

Chapter 1

Introduction

1.1 Framework

The current global energy scenario is very dependent on the use of non-renewable raw materials, which has had a great impact, namely climate change, on the entire planet. The necessity to find a new energy carrier with low-carbon emission brought with it the perfect scenario for the use of hydrogen (H_2), but the implementation of the technology comes with a lot of challenges [1]. The significance of hydrogen is recognized because, among other things, it is an energy carrier with a high energy density, making it a viable alternative for intense industrial operations, storing chemical energy generated from renewable sources, and permitting the rise of other renewable-based fuels (e.g. synthetic fuels for maritime transport and aviation) [2]. The hydrogen-based-energy technologies form a direct alternative to electricity-based systems. In the near future, the choice between them is expected to be based in technical improvements of the current and future technologies [3].

Governments worldwide are making great effort to decarbonize their economy in order to curb the effects of climate change. On 12 December 2015, a list of 196 countries signed the Paris Agreement at 21^{st} Conference of the Parties (COP21) in Paris, including Portugal. Its goal is to limit global warming to below 2 °C compared to pre-industrial levels [4]. Despite the good intention of the Conference, since then, carbon dioxide (CO_2) concentration in atmosphere continued to rise, as shown in figure 1.1.

A major part of CO_2 emissions comes from non-renewable sources such as fossil fuels (mainly coal, oil and gas), in energy use (flaring, heating, *etc*), industrial processes (cement, chemicals, *etc*) and human activities (transportation and livestock). According with data in figure 1.2, since the beginning of the XXI century, the emission of CO_2 increased drastically in China and it started to grow in India as well. In contrast, in Europe (EU27+UK) and Japan, the fossil CO_2 emission reduced in the last decade [5–7].

Total fossil CO_2 emissions decreased in the last few years, with good numbers like a reduction of 9.6 to 8.7 % between 2015 and 2019. The sharp decrease in coal and oil

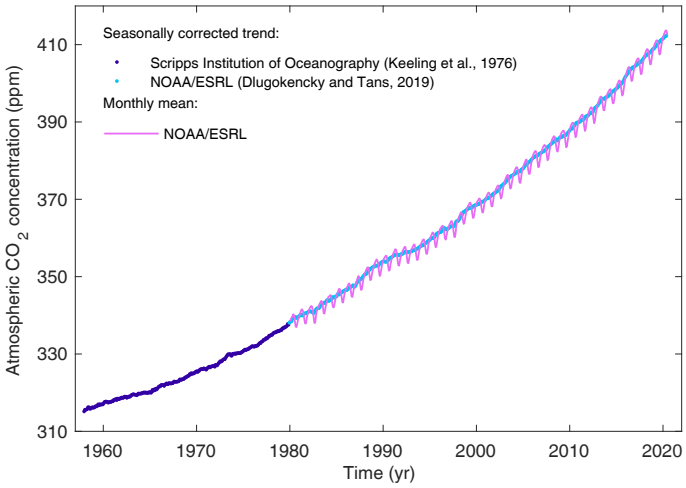

Figure 1.1 Average atmospheric CO_2 concentration in ppm at the ground level. Source: Friedlingstein *et al.* [8].

consumption contributed to a reduction of 4.2 % in CO_2 coming from combustion emission. Portugal had a decrease 6.8 % of CO_2 discharge, most of it as a consequence of moving away from coal and other liquid fossil fuel to less carbon intense energy sources. Major fuel emissions in Portugal come from the power industry and transport sectors, with some contribution from the industrial combustion, as shown in figure 1.3. Also, the emissions of CO_2 in Portugal has decreased since the sign of COP21. Some part of this comes from the diminution of the country population in the past years [5].

In 2016, Portugal set the goal of becoming carbon neutral by 2050, after developing the Roadmap for Carbon Neutrality 2050 (RNC2050). In 2018, renewables accounted for 30.3 % of gross final energy consumption (up 10.8 % from 2005), making Portugal the 6^{th} country in the European Union with the highest level of renewables incorporation. The

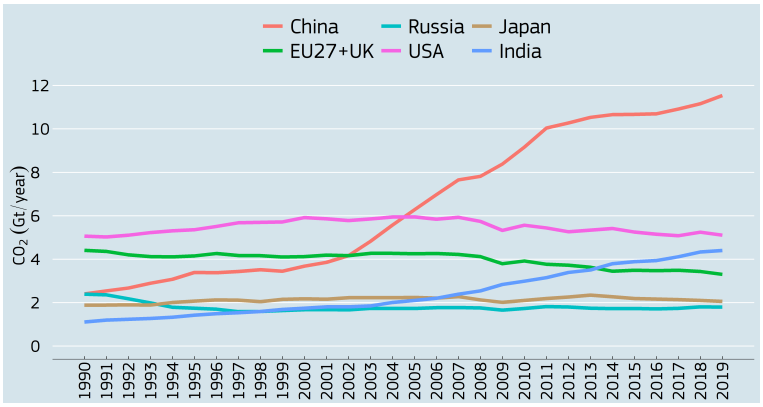

Figure 1.2 Fossil CO_2 emission of the major emitting economies. Source: European Commission report [5].

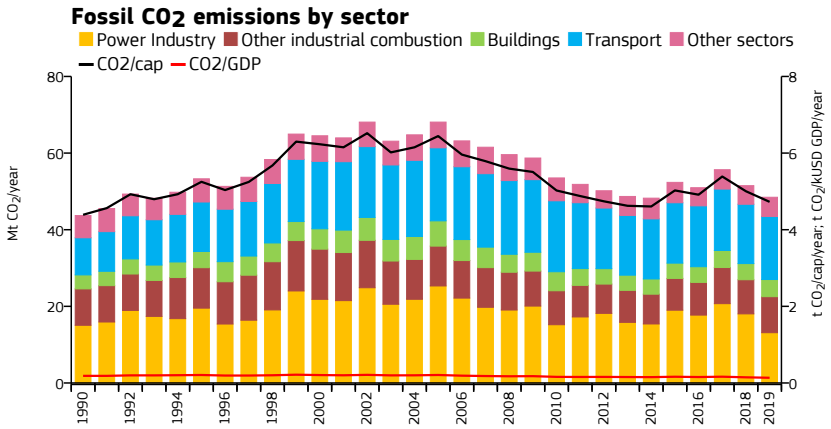

Figure 1.3 Fossil CO_2 emission in Portugal by sector of economy. Bars are refereed to the left axis. Lines are refereed to right axis. Source: European Commission report [5].

implementation of hydrogen economy can be seen as an opportunity to make it a fundamental vector for decarbonization of portuguese national economy towards carbon neutrality, while promoting innovation and development in the area. Figure 1.4 shows how portuguese government sees an opportunity in the hydrogen economy. All sectors seem to benefit from that change, with most important ones from energetic and transportation sectors. It also creates new opportunities of innovation, research and development, putting Portugal as pioneer in Europe and leading towards the transition [2].

Use of H_2 as a fuel reduces the emissions of greenhouse gases (GHG), but H_2 economy can have some problems, as the leakage of H_2 and increase of water (H_2O) vapor in the stratosphere can impact atmosphere as a whole in many ways [3, 9]. Large scale emission of H_2 could enhance the problem of climate change and/or influence the chemical composition

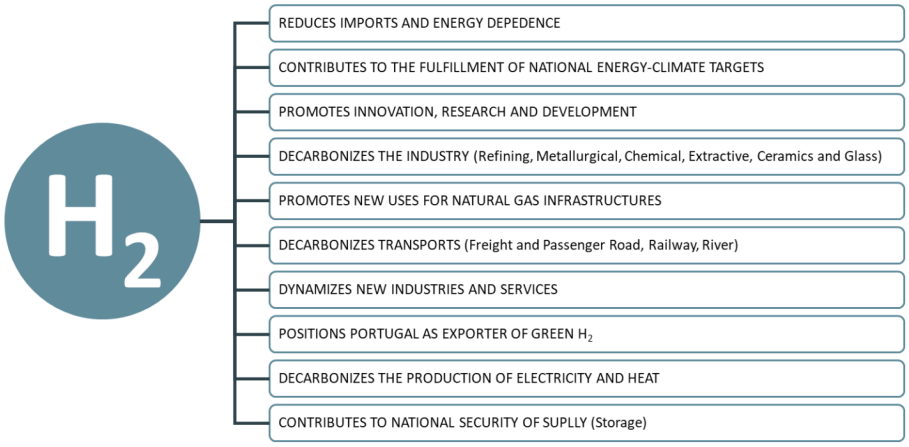

Figure 1.4 Hydrogen as a energy vector in Portugal, opportunities and goals. Source: Secretaria de Estado Adjunta e da Energia [2].

of the atmosphere, as the oxidation of it is a source of stratospheric H_2O. As a result, increasing the source of H_2 in the atmosphere should moisten the stratosphere unless it is offset by an equally robust rise in the rates of processes that destroy hydrogen. This would cause lower stratospheric cooling and ozone (O_3) chemistry to be disrupted, as O_3 chemistry is dependent on heterogeneous reactions involving hydrochloric acid (HCl) and chlorine nitrate ($ClNO_3$) on H_2O ices. [10–13].

1.2 Motivation

Nowadays the world is trying to abandon fossil fuels and follow a green path. The transition can be performed using bio fuels and hydrogen. With all of this going on, and the opportunity to work in such an important area as combustion, and contribute to a better understanding of the properties of the hydrogen flame, the choice of this topic for the final master's thesis proved to be a very impactful option. It can contribute to a better understanding of the hydrogen combustion, flame properties, and burners adaptation to hydrogen economy. Furthermore, my own preference for the field of chemical engineering simulation and programming was a deciding factor in selecting this topic.

1.3 Objective

The objective of this work was to investigate detailed combustion kinetic mechanisms of pure H_2 and mixture with others fuels, such as biogas and natural gas. Flame temperature and flame speed are the parameters used to evaluate fuel performance. This work aims to estabilish the necessary changes in the current equipments that use other types of fuel, like stoves, burners, heaters, vehicles, to adapt them to the new green fuel to be introduced in Portugal, or even in the Europe, as well as design miniaturized energy systems.

1.4 Thesis structure

The way that this master's thesis is structured, aims to give the reader a easy time to gain a better understanding of the topic of hydrogen and its properties. It's divided in 5 chapters, which will be detailed:

- **Chapter 1 - Introduction:** In the first chapter, a brief introduction about how H_2 enters in the present world scenario is showed. After that, the plan to limit global

warming signed in COP21 and CO_2 emission through the years is presented. Hydrogen economy in Portugal with its opportunities and potential advantages, along with some problems that can be faced is presented as the last part of framework. In this chapter, motivation and objective of the master thesis are also presented.

- **Chapter 2 - Overview:** The first part of overview presents 4 important topics about hydrogen, that being its production, transportation, storage and its final use, where present technologies are addressed. After that, a brief explanation about type of flames and its particularities is shown, followed by a brief topic about stoichiometry in combustion and equivalence ratio.

- **Chapter 3 - Methodology:** In the methodology chapter, the first part is about all the kinetic mechanisms used in this work, while also explaining the three parts that kinetic mechanisms are composed, that being thermodynamics, reaction and transport sections. Also, a explanation on how adiabatic flame temperature, laminar flame speed and flame stability are calculated in the simulator, followed by a brief explanation of the scripts used.

- **Chapter 4 - Results and discussion:** In this chapter, results obtained with numerical simulations are shown and discussed. The first part is about the adiabatic flame temperature and the influence of 4 parameters in it, that being equivalence ratio, pressure, unburned gas temperature and composition. Compositions tested were pure hydrogen, hydrogen with methane and hydrogen with biogas. The second part is about the laminar flame speed and the influence of the same 4 parameters in it, while also testing the influence of some simulation parameters in the results. Empirical equations were proposed and validated. The flame stability results are also shown in this chapter.

- **Chapter 5 - Conclusions:** In the fifth and final chapter, the conclusions of the work are presented. The conclusions are about the most important topics from the Results and discussion section, those being adiabatic flame temperature, laminar flame speed, and flame stability and operation limits. Also, future works are suggested to complement and improve this work.

Chapter 2

Overview

2.1 A brief introduction

This chapter provides an overview of four key aspects of the hydrogen as an energy carrier: production, storage, transportation, and usage. This is crucial to demonstrate how modern technologies are in various areas, as well as to provide information for a clear understanding of the issues involved. A quick explanation of what combustion is, flame types, combustion stoichiometry, and how it influences most of the calculations covered in subsequent parts will be presented in the final part of this section.

2.2 Production of hydrogen fuel

Nowadays, the production of H_2 is mostly made from fossil fuel processing such as natural gas (NG), although some non-fuel processing paths can be used as well. A major challenge the industry is facing is the scale up of hydrogen production. Because of that, some researchers claim that H_2 should be produced from a large range of feedstock, not depending on just one major source [14]. This is because certain places find it easier to use a particular technology than others. Thermal processing is simple in nations with vast reserves of fossil fuels, while biological processing is simple in countries with large volumes of forest leftovers. Actual hydrogen production technologies can be divided into four major process types: thermal, electrolytic, photoelectrochemical, and biological.

Thermal processes are based on the release of H_2 molecules from raw materials, coming from fossil fuels, such as hydrocarbons and natural gas, coal or even from renewable sources like biomass and bioethanol [14, 15]. Some of the thermal processes used to produce H_2 are steam reforming (SR), partial oxidation (POX), autothermal reforming (ATR), bio-derived liquids reforming (BDLR), and coal and biomass gasification [15, 16].

The electrolytic process produces hydrogen of higher purity when compared to thermal processes, although the process water used must be purified [14]. This process accom-

modates three alternative technologies: the alkaline electrolysis (the most widely used), polymer membrane (PEM) and solid oxide electrolyzers (SOE) [17]. When compared among them, SOE is the most electrically efficient, but has some challenges like corrosion, sealing, thermal cycling and chrome migration. When comparing PEM and alkaline electrolysis, results shows that the former one tends to be more efficient, although the technology is more expensive, while the later one has lower capital cost. Alkaline electrolysis is the most developed and used process but has the lowest average efficiency between all 3 [16].

The photoelectrochemical technology is at an early stage of development. It uses electromagnetic energy to split water molecules into H_2 and oxygen (O_2) [14, 15]. Photoelectrochemical uses a cell based on semiconductors as photoelectrodes, separated by a membrane in a cell immersed in an aqueous electrolyte solution. N-type semiconductors act as photoanode, while p-type semiconductors as photocathode, and they can be used in conjunction or with a metal conductor. Electrons are stimulated and rise from the valence band to the conduction band when the photoanode is exposed to light with a higher energy than its energy bandgap. Then, they flow through the external circuit to the metal cathode or photocathode [18]. Currently the photoelectrochemical hydrogen production process is in an early stage of development. Research for pure hybrid and unique solar hydrogen systems are on full speed, with the goal of determining the technology's limits, potential enhancements, and performance [19].

The biological path uses biomass to produce H_2 in a green path. Biological activities catalyzed by microorganisms in an aqueous environment under atmospheric pressure and at ambient temperature are in contrast to electrolysis and thermochemical processes. These procedures can be used in areas where there is a readily available source of biomass or another suitable waste material, lowering energy costs, and cost of transporting the initial raw material. Biological hydrogen production can be divided into five technologies: direct biophotolysis, indirect biophotolysis, biological water-gas conversion, photofermentation and dark fermentation. In all processes, enzymes, particularly nitrogenase and hydrogenase, are involved and the hydrogen produced is a byproduct of the metabolism from anaerobic microorganisms [20]. Some studies were made reviewing the production of H_2 by fermentation and showed favored results [14, 21]. Other studies about the use of wastewater in bio refineries using microbial electrolysis cells (MEC) were made. Early results shows that it can reduce the cost of wastewater treatment while providing benefits with the production of H_2, but this technology needs to be studied more [22].

Around 96 % of the H_2 produced worldwide come from thermal processes, while the remaining 4 % are produced by water electrolysis [23]. The other process technology have actually a negligible importance. Figure 2.1 shows the feedstock distribution in hydrogen production.

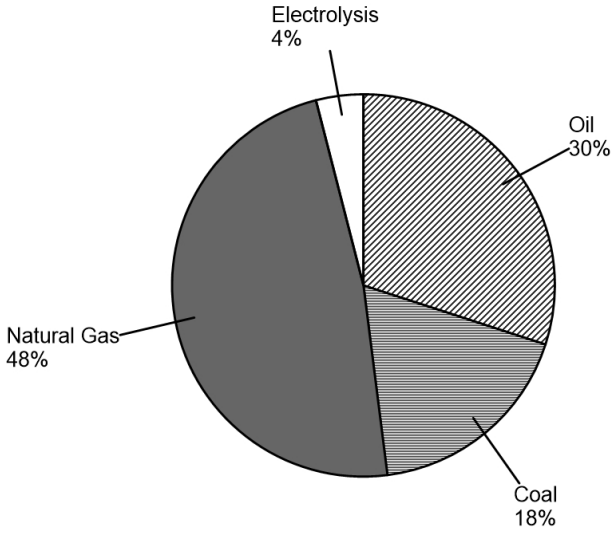

Figure 2.1 Main production sources of hydrogen, 2006 worldwide data. Adapted from Khotari *et al.* [24].

A potential green hydrogen method relies on generating electricity for an electrolyzer from solar or wind energy. In that route, zero CO_2 is emitted to the atmosphere, however, the solar panel that is utilized to collect the sunlight is somewhat pricey. A geothermal path can also be used, where steam coming from reservoirs of hot water found below earth's surface is used to rotate a turbine that activates a generator to produce electricity. It could also be used in conjunction with a PEM electrolyzer to produce hydrogen in a green path. The accessibility of these thermal resources is one of the key barriers to geothermal energy utilization [25, 26].

2.3 Storage of hydrogen

After being produced, the hydrogen must be stored, for future use. There are two storage technologies: material-based and the physical-based technologies. The former is based on the sorption of molecular hydrogen on chemical compounds, while the later one is based on physical transformation or compression of H_2 and storing it on a vessel. Figure 2.2 shows a scheme that represents actual storage technologies, where material-based can be divided into physical and chemical sorption, while physical-based can be divided in liquid H_2, cold/cryo-compressed and compressed gas [27]. Hydrogen is mainly stored

in compressed gas state (from 35 to 70 MPa [28]) and low-temperature liquid (at 20.25 K and 101.3 kPa [29]). These storage conditions result in high storage and transportation costs, which can make H_2 less competitive compared to other fuels [30]. This is due to the high energy consumption during compression and liquefaction. Worldwide, the most used technology in refueling stations is in compressed gas form, at stationary, transport and bulk transportation [31, 32].

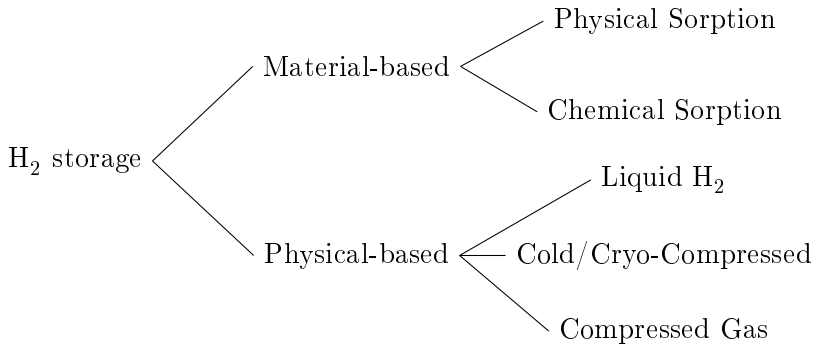

Figure 2.2 List of actual H_2 storage technology types. Adapted from Moradi *et al.* [27].

Compressed gas H_2 is the most known and convenient technology. Compressed H_2 can be stored in a variety of forms. For lightweight capacities, like in vehicles, carbon fiber composite pressure vessels are used, with pressures ranging from 20 to 100 MPa. For high capacity storage, metal vessels are used, and also underground such as salt caverns, aquifer and human-made cavities can also be a potential site to be used [31, 33, 34]. There are four generic types of pressure vessels to store hydrogen.

- **Type I:** Made of metal, are the most conventional and cheaper. Can contain maximum pressure of 50 MPa.
- **Type II:** Made of metal, usually steel, and composite material. The cost is around 50% higher than type I and is lighter. Pressure is not limited.
- **Type III:** Mainly composed by carbon fiber composite, with a thin aluminum liner. Reliable for pressures up to 45 MPa. The cost is twice the one of Type II, and is considerable lighter.
- **Type IV:** Made of polymer like high-density polyethylene (HDPE). Is the lighter among all vessel types and can withstand pressures up to 100 MPa. The major problem of this vessel type is its high cost [27, 35, 36]. Figure 2.3 shows an example of a type IV vessel.

For low pressure storage (up to 50 MPa), steel vessels are a good option, due to low cost compared with composite ones, who are indicated to be used for higher pressures. Storage of hydrogen in compressed gas form has an economic advantage. Nowadays, liquefaction of hydrogen process consumes 30 to 40 % of fuel lower heating value (LHV) [37], while the process of high pressure gas compression consumes approximately 5 to 20 % of H_2 LHV [38].

Figure 2.3 Type IV vessel for hydrogen gas storage. Source: Gerboni *et al.* [39].

Liquid hydrogen storage achieve higher energy density than compressed storage. Because it is denser than compressed H_2, it results in compact refueling stations, which is perfect for existing stations that deal with space limitations. On the other hand, the energy consumption to make the liquefaction is really high, around $10\,\mathrm{kWh\,kg_{H_2}^{-1}}$ [31, 37]. To liquefy the hydrogen, a Linde-Hampson based cycle is used, which is combination of compression, expansion and throttling. Figure 2.4 shows a diagram representing the liquefaction method cited. It requires hydrogen to be in temperatures around 20 K, with the benefit of not being at high pressures (atmospheric pressure) [40]. The storage is made using cryogenic vessels, which are also used during its transportation, being achieved by vacuum insulated inner pressure with an external casing [31].

Cryo-compressed hydrogen (CCH) is a technology that brings the best parts of compressed gas and liquid H_2. It has been proposed by many sources, including for example german automotive company BMW [42]. In this method, H_2 is stored in pressure vessels at cryogenic temperatures, around 20 K and pressures between 25 to 35 MPa [43]. When pressure is above 1.3 MPa hydrogen becomes a supercritical fluid maintaining high density. Storage density of CCH is said to be about $87\,\mathrm{kg_{H_2}\,m^{-3}}$ at 21 K and 24 MPa, which is higher when compared to liquid hydrogen ($70\,\mathrm{kg_{H_2}\,m^{-3}}$) and compressed gas ($39\,\mathrm{kg_{H_2}\,m^{-3}}$) at room temperature and 70 MPa [40, 44]. Also, it has lower boil-off loss when compared to liquid storage [45], offers quick and efficient refueling and high safety level [27]. This

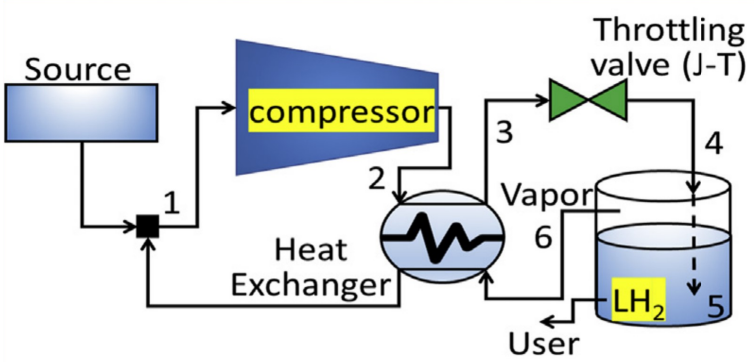

Figure 2.4 Linde-Hampson cycle used for H_2 liquefaction. Source: Ratnakar *et al.* [41].

method of storage is said to be suffering of heat leakage more than compressed gas and liquid hydrogen systems. Also, the power consumption falls between the other two, and the embrittlement[1] problem is also verified in this form of storage [40].

As mentioned, material-based technologies can be divided in two techniques: physical sorption and chemical sorption. Those materials should have certain characteristics, such as rapid kinetics, good reversibility, low price and high storage capacities [31, 47, 48].

Physical sorption is basically a physical bonding of H_2 in the adsorbent surface by very weak van der Waals forces [49], occurs quickly at low temperatures and does not cover any chemical reaction. Materials used are carbon nanostructures (like graphene, carbon nanotubes, C_{60} buckyballs), metal organic framework (MOF), covalent organic framework (COF), polymers of intrinsic microporosity (PIM) and zeolites. All materials have a limited capacity to store hydrogen, which presents several obstacles to be overcome along with the requirement that they need to be maintained at low temperatures. [31, 40, 50]. Table 2.1 shows the volumetric capacity from the adsorbents said before.

Chemical sorption occurs when hydrogen molecules split into atoms and form chemical bonds, sharing electrons with the absorption site [27, 31], with much stronger interaction compared to physical sorption, which makes harder to reverse the reaction [55]. Some materials used in this storage technology are ionic, covalent and complex hydrides and some other liquid organic hydrogen carriers (LOHC).

Chemical hydrides are compounds of H_2 and non-metal. Some examples of chemical hydrides are ammonia (NH_3), ammonia borane (NH_3BH_3), diborane (B_2H_6). Those chemical hydrides are very attractive because they have high hydrogen storage density,

[1] The word 'embrittlement' refers to the loss of macroscopic ductility and the brittle look of fracture surfaces, when examined at low magnification [46].

Table 2.1 Hydrogen storage capacity of different construction materials. Source: [40, 51–54]

Material	Capacity	Observations	Reference
MOF	$0.021\,kg_{H_2}\,L^{-1}$	-	[40]
COF	$0.063\,kg_{H_2}\,L^{-1}$	-	[51]
Graphene	$0.135\,kg_{H_2}\,L^{-1}$	-	[52]
Carbon nanotube	$0.068\,kg_{H_2}\,L^{-1}$	SWCN†	[53]
Zeolite§	$0.071\,kg_{H_2}\,L^{-1}$	77 K and 1.5 MPa	[54]

† Single wall carbon nanotube.

§ Zeolite X.

around $107\,kg_{H_2}\,L^{-1}$ for NH_3, for example, and also has hydrogen release easiness, a major problem of metal hydrides (MH_X) that will be discussed further [40, 56, 57]. Although, they are reversible, so they left-over by-product (spent material) must be removed from the tank for off-board regeneration and has the by-product removal issue [58].

Metal hydrides are produced reacting H_2 with a metal or metal alloy (M). Several materials can absorb H_2 under low temperatures and pressure. Examples are lithium (Li), boron (B), magnesium (Mg), and aluminium (Al) [58, 60]. It seems to be the safest method for storing hydrogen, due to low operating temperature and endothermic H_2 release, but suffer of the disadvantage of weight for on-board storage and really slow kinetics for H_2 release, low reversibility, and high dehydrogenation temperatures [40, 61–64]. Chemical and metal hydrides store from 10 to 20 % of H_2 content in weight [65].

LOHC are one of the most promising types of chemical sorption storage types. Hydrogen makes covalent chemical bonds with hydrogen-lean molecules, such as cycloalkanes, N-substituted heterocyles, 1,2-BN-heterocycles, methanol (CH_3OH) and formic acid (CH_2O_2) [27, 40]. Molecular H_2 is released from these molecules by catalytic dehydrogenation [66]. LOHC are very attractive, because they can be used at ambient conditions, are carbon free and the liquid solvent can be recovered and then reused. On other hand LOHC has low storage capacity [27]. LOHC have a capacity to store from 5 to 6 % of hydrogen content in weight [65]. Other types of chemical sorption are the complex metal hydrides and multi component storage. Table 2.2 shows a resume of the advantages and disadvantages of the storage methods mentioned before.

Table 2.2 Storage technologies of molecular hydrogen. Comparison of their main advantages and disadvantages. Source: Ma *et al.* [59].

Storage method	Advantages	Disadvantages
Compressed gas	Mature technology	Risk of high-pressure leakage, requiring high-strength, and economical materials.
Liquid	High storage density	Cooling technology consumes high energy and requires special double wall design and materials with good heat insulation.
Cryo-compressed	High capacity[†]	Immature technology, high requirements for materials, and poor economy.
Physical sorption	Fast kinetics	Low storage capacity, must be maintained at low temperatures.
Chemical sorption	Carbon free[§]	Slow kinetics, has left-over product, high temperatures to dehydrogenation, LOHC has low storage capacity.

[†] High weight and volume capacity.

[§] Can be used in ambient condition, chemical hydrides have high storage density.

2.4 Transport of hydrogen

Hydrogen needs to be transported to its destination (consumption or storage sites). There are a variety of ways to do it. Depending on the destination and infrastructure, on land H_2 can be transported via road or rail transportation, on any of the states cited in section 2.3. Also, transportation via pipelines is an alternative for short distances. Ocean transportation is also an alternative being studied for the near future when talking about long distances [67].

Pipeline transportation of hydrogen is said to be very limited and derived from natural gas technology, as existing pipelines are made of ordinary steels used in normal construction. There have been no reported issues with the use of these pipelines [39]. Operating pressures vary depending on the network, but are typically between 0.34 and 10 MPa, usually around 1 to 2 MPa. Their diameter can range from 10 to 300 mm, usually above 250 mm [39].

On land hydrogen transportation is carried out using pressure-proofed seamless vessel, where it can be in gas or liquid state, using trucks or railways. This type of transport can be used when pipeline infrastructure is not available or if the place where the H_2 is needed doesn't have a local production. Compressed gaseous hydrogen is generally transported using gas cylinders or gas tubes, with pressures ranging from 20 to 50 MPa, using gas trailers. Those cylinders, normally with the capacity of 2000 L, are bundled in modules, and the trailer with steel cylinders carries approximately 25 000 L of H_2 [39].

Figure 2.5 Hydrogen tube trailer vessel for road transport (Type I). Source: Gerboni *et al.* [39].

Some lighter materials are also being used to manufacture the cylinders, made of composite materials. A cylinder made of carbon fiber over HDPE, for example, can carry up to 39 600 L of H_2, at the same pressures of the steel cylinders. Figure 2.5 shows a trailer with a pack of cylinders of type I [39, 68].

Liquid hydrogen is transported using cryogenic tanks, with temperatures below 20 K. It is mentioned by Moradi *et al.* that this method is economically interesting for high H_2 demands, above 500 $kg_{H_2}\,day^{-1}$ and for mid distances (approximately 1000 km), which is an improvement if compared to the referred distance for compressed gas (320 km) [27, 68, 69]. Trucking liquid hydrogen is more economical because a liquid tanker truck is able to carry 5 to 6 times more mass of H_2 than a gaseous tube trailer (800 kg from compressed gas versus 4000 to 5000 kg on liquid state) [69, 70].

Ship transportation is a topic that actually is under investigation. Some studies shows that ocean transportation of hydrogen should be made in liquid state, in spherical tanks with a capacity of 40 000 m^3. An example of a ship developed by Kawasaki Heavy industries is shown in figure 2.6 [39].

A problem faced by pipeline transportation is related to degradation on pipeline steel. Some studies point out that H_2 can cause some catastrophic failures, inducing cracking on the pipelines, stress-oriented hydrogen induced cracking and sulfide stress corrosion cracking (this applies to H_2 produced from thermal processes). Hydrogen causes an embrittlement on the steel alloy, caused by the ingress of atomic hydrogen (H) into interstitial

Figure 2.6 Kawasaki prototype of ocean transportation of hydrogen fuel. Source: Gerboni *et al.* [39].

spaces. It can occur by the adsorption of molecular hydrogen from atmosphere, around the pipeline, production processes that introduces H into the steel and the presence of some hydrogen producing species, such as hydrogen sulfide (H_2S) [71–73]. Figure 2.7 shows a pipeline steel embrittlement caused by hydrogen operation. Embrittlement effects are reduced when pipeline pressure is kept low, which is why common steels are still used today. It is possible to mix hydrogen with natural gas and use the existing natural gas network to avoid incurring unnecessary investment expenditures. When the volume proportion of hydrogen is less than 20 % (which translates to 5 to 7 % energy content), ordinary materials can be used without major consequence [39].

One of the various problems faced when transporting hydrogen in liquid state are the boil-off during delivery. Around 0.3 % of the volume transported of the liquid hydrogen is lost during change from the cylinder to its destination, and it is caused by the high volatility [68]. The difference of temperature between the hydrogen and ambient temperature is really high (around 273 K), which is a major concern, because some security problems may occur and the integrity of the workers can be at risk. To prevent any harm, the adoption

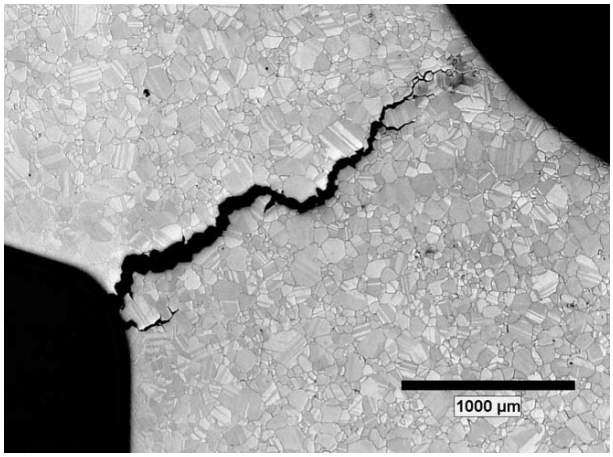

Figure 2.7 Pipeline steel embrittlement caused by operation with molecular hydrogen. Source: Iannuzzi *et al.* [74].

of some protection systems, like hydrogen detection sensors, inert atmosphere (to prevent flame propagation for example) and protection equipment should be adopted [39, 68, 75].

2.5 End use of hydrogen

It is known that hydrogen has a variety of uses in today's world. Particularly, H_2 has a major role as the new energy vector in the industry, transport, energy storage, electricity production and heating sectors [23, 76, 77]. Nowadays, hydrogen application is dominated by industrial applications, mainly being used on oil refining, on Fischer-Tropsch reaction, production of ammonia via Haber-Bosch process, urea, methanol and steel production via direct reduction of iron ore [76, 78–80].

As a fuel, hydrogen is used as a rocket fuel, for example by the National Aeronautics and Space Administration (NASA) and SpaceX, in liquid H_2 state. NASA began using it the 1950's, where they also were the first to use hydrogen fuel cells to power up electrical systems on spacecraft [81].

On transport, hydrogen is used in vehicles. The main goal is to have a domestic production of hydrogen, so it can be used in a fuel cell, for high efficiency, zero-emission electric vehicles [81]. Various applications for hydrogen and fuel cells include distributed or combined heat and power, backup power, systems for storing and enabling renewable energy, portable power, auxiliary power for trucks, aircraft, rail, and ships, specialty vehicles such as forklifts, and passenger and freight vehicles such as cars, trucks, and buses [82]. Similar applications of natural gas and H_2 in transport sector is listed on table 2.3.

There are multiple technologies in varying levels of development that allow the temporal shifting of electrical energy over time intervals ranging from hours to days, but none of them can store this energy on a week-month time scale. As a solution to this problem, hydrogen is introduced. A process called power-to-gas (P2G) can be used, where an excess electrical energy is converted into molecular hydrogen. This is possible due to the fact that all excess of electrical energy can be used to power electrolysis and produce hydrogen, a chemical way to store excess energy, which can in appropriate time, be converted again to electricity in a fuel cell [77].

Half of global final energy consumption and a third of global energy-related carbon dioxide emissions are attributed to heat generation in buildings and industries [84]. This heating can be performed for example, with fuel cells (because of the electrical efficiency advantage). In homes, hydrogen can be used with those fuel cells, direct flame combustion boilers, catalytic boilers and gas-powered heat pumps. In the case of boilers, hydrogen

Table 2.3 Selected applications of natural gas and hydrogen fuels: where CNG and LNG stands respectively for compressed and liquified natural gas, and CH2 and LH2 also stands for compressed and liquified hydrogen. Shaded cells corresponds to valid applications [83].

Application	Natural Gas		Hydrogen	
	CNG	LNG	CH2	LH2
Light duty vehicles				
Buses				
Med duty trucks				
Heavy duty trucks				
Rail				
Marine				
Aviation				

would be used as a fuel instead of NG. In the catalytic boiler, H_2 passes through a highly reactive metal catalyst, where an exothermic reaction takes place to produce heat, and this results in low NO_x emissions [85, 86]. On the gas-powered heat pump, H_2 could be used to generate heat through combustion, to provide sufficient energy for a phase change on the working fluid being used in the system [84].

2.6 Combustion

Throughout its existence, humanity has been fascinated by combustion. Currently, combustion of liquids (such as gasoline and hydrocarbon fuels), solids (such as coal and wood), and gases (such as natural gas and hydrogen) provides roughly 90 % of global energy [87, 88]. Combustion can be defined as "group of chemical reactions between substances, usually including oxygen and usually accompanied by the generation of heat and light in the form of flame" [89]. Combustion is significant because it converts chemically stored energy into heat that may be utilized in a variety of ways [90]. There are a lot of applications and study of combustion in different areas, for example:

- Power Generation, for example to produce electricity, for transportation purposes of automobiles, aircrafts, rocket motors for space and missile propulsion, etc;
- Household and industrial heating;

- Process industry for production of engineering materials, like fabrication of ceramic materials by self-propagating high-temperature synthesis (SHS) process;
- Safety protections for unwanted combustion;
- Pollutant emission control of combustion products, namely nitrogen oxides (NO_x), sulfur oxides (SO_x), carbon monoxide (CO), soot, coke, etc;
- Enhancement of combustion efficiencies [88].

Hydrocarbon fuel combustion process produces CO_2, CO in case of incomplete combustion, water, and other sub products. A single step global chemical reaction for burning hydrocarbons in air can be written as equation (1).

$$C_xH_y + (x + y/_4)(O_2 + 3.728N_2) \longrightarrow y/_2H_2O + xCO_2 + (x + y/_4)3.728N_2 \quad (1)$$

On the other hand, hydrogen combustion in air only generates water as a product species, and it can be written as equation (2).

$$2\,H_2 + O_2 + 3.728N_2 \longrightarrow 2\,H_2O + 3.728N_2 \quad (2)$$

As CO_2 is not produced by hydrogen fuel, it has a major role to contribute on carbon dioxide emission reduction, which dovetails with the environmental goals for the next years.

2.7 Flame types

The way the fuel and oxidant are mixed in a burner, as well as their flow rates, can produce several sorts of flames. Premixed gas flames are formed when fuel gas and air are mixed before entering the burner. Diffusion flames are formed when the fuel and oxidant mix after exiting the burner. Flames can also be divided based on their flow regime. If the gas average velocity is low, the entering gaseous flow of fuel and air, as well as the flame, will be laminar. On the other hand, if the gas average velocity is high, resulting in a high Reynolds number (N_{Re}), the flow regime can be called as turbulent. Flames can be classified as laminar premixed, laminar diffusion, turbulent premixed, or turbulent diffusion. [87, 90, 91]. Figure 2.8 shows the four types of flames described above.

Examples of laminar premixed flames are Bunsen flame and flat flame, while examples of turbulent premixed flames are spark-ignited gasoline engine and low NO_x stationary gas turbine. Wood fire and candle are examples of laminar diffusion flames, while pulverized

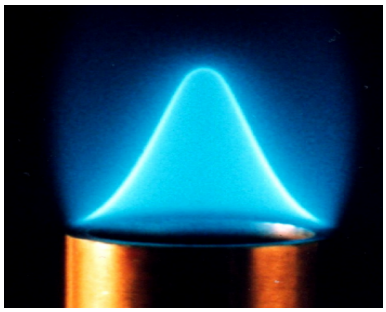

(a) Laminar premixed flame

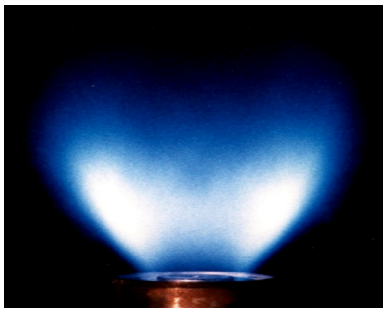

(b) Turbulent premixed flame

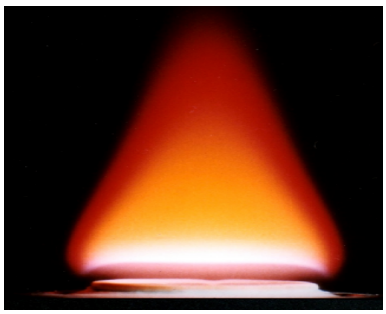

(c) Laminar diffusion flame

(d) Turbulent diffusion flame

Figure 2.8 Examples of flame types for gas fuels. Source: Ahmed PhD thesis [92].

coal combustion and aircraft turbine are examples of turbulent diffusion flames. A flame of a specific fuel-air mixture is defined by three primary parameters: burning velocity (or flame speed), flame temperature, and flammability limit, all of which are influenced by pressure, temperature, and equivalence ratio [91].

2.8 Combustion stoichiometry

The relative amount of oxidizer required to totally burn the fuel is known as the stoichiometric quantity. When more than the stoichiometric amount of oxidizer is supplied, the premixture is said to be fuel lean, or merely lean. When less than the stoichiometric amount of oxidizer is supplied, the premixture is said to be fuel rich. Simple atomic species balances are used to calculate the stoichiometric oxidizer (or air) to fuel ratio, assuming that the fuel interacts to generate the final fully oxidized set of products [90]. The ratio between the number of moles of fuel per moles of oxidizer is called fuel-oxidant ratio (n_F/n_O). The stoichiometric condition varies for the different fuels, and so, the equivalence ratio (ϕ) is a way to normalize that stoichiometry.

The equivalence ratio is said to be the quotient between actual value of fuel-oxidant ratio and stoichiometric value of the same, that is called $(n_F/n_O)_{st}$. So equivalence ratio

is calculated by equation (3).

$$\phi = \frac{(n_F/n_O)}{(n_F/n_O)_{st}} \tag{3}$$

From equation (3), it is possible to notice that when ϕ is greater than 1, the mixture is said to be fuel-rich, when ϕ lower than 1, the mixture is said to be fuel-lean, while for a value of $\phi = 1$, a stoichiometric mixture is achieved. Table 2.4 shows the stoichiometric ratio for different fuels.

Table 2.4 Stoichiometric fuel/air ratios for different fuels.

Fuel	H_2	H_2/CO (50%)	CH_4	C_2H_6	C_3H_8	C_4H_{10}
$(n_F/n_O)_{st}$	2.00	2.00	0.50	0.29	0.20	0.15

Equation (3) can be derived to use air (n_A) as the oxidant mixture, as shown on equation (4).

$$\phi = \frac{\varphi\ n_F}{0.2094\ n_A} \tag{4}$$

The φ corresponds to $(n_0/n_F)_{st}$, the stoichiometric coefficient of O_2 for complete fuel oxidation. Equation (4) can also be derived to comprise a fuel mixture of n components, as shown on equation (5), where the 0.2094 coefficient corresponds the average molar fraction of O_2 in air at sea level [93].

$$\phi = \frac{\sum_{i=1}^{n}\ \varphi_i\ n_{Fi}}{0.2094\ n_A} \tag{5}$$

Chapter 3

Methodology

3.1 Combustion Kinetic

Combustion kinetics describes the chemical species transformations along the burning process. Kinetic combustion mechanisms are the key part of this work. It contains species, associated with a range of reaction steps, which the number of reactions depends on the kinetic mechanism detailing. Those steps are characterized by kinetic constant data and a compilation of thermodynamics and transport properties. Kinetic mechanisms used in this work were GRI-MECH 3.0, San Diego Mech, Qin Mech, AramcoMech_1.3 and Boivin Mech.

3.1.1 GRI-MECH 3.0

GRI-MECH 3.0 is a kinetic oxidation mechanism for modeling natural gas combustion, which includes the generation of nitric oxide (NO) and the chemistry of reburn [94]. GRI-MECH 3.0 has 325 reactions and 53 species. It uses 24 of those reactions and 9 species strictly for $H_2/O_2/N_2$ mixture, which are listed on table 3.1. GRI-MECH 3.0 goal is intended to produce good basic kinetics as well as the best integrated modeling prediction of basic combustion parameters. Studies using GRI-MECH 3.0 can be found on references [95–99].

Table 3.1 $H_2/O_2/N_2$ reactions path, pre-exponential factor (A), temperature exponent (b) and activation energy (E_a) extracted from GRI-MECH 3.0.

	Reaction	$A\ [cm, mol, s]$	$b\ [-]$	$E_a\ [\mathrm{cal\,mol^{-1}}]$
(1)	$2O+Y \rightleftharpoons O_2+Y$	1.200×10^{17}	-1.000	0.00
(2)	$O+H+Y \rightleftharpoons OH+Y$	5.000×10^{17}	-1.000	0.00
(3)	$O+H_2 \rightleftharpoons H+OH$	3.870×10^{4}	2.700	6260.00

Continued on next page

Table 3.1 – *Continued from previous page*

	Reaction	$A\ [cm, mol, s]$	$b\ [-]$	$E_a\ [\mathrm{cal\,mol^{-1}}]$
(4)	$O+HO_2 \rightleftharpoons OH+O_2$	2.000×10^{13}	0.000	0.00
(5)	$O+H_2O_2 \rightleftharpoons OH+HO_2$	9.630×10^{6}	2.000	4000.00
(6)	$H+O_2+Y \rightleftharpoons HO_2+Y$	2.800×10^{18}	-0.860	0.00
(7)	$H+2O_2 \rightleftharpoons HO_2+O_2$	2.080×10^{19}	-1.240	0.00
(8)	$H+O_2+H_2O \rightleftharpoons HO_2+H_2O$	11.26×10^{18}	-0.760	0.00
(9)	$H+O_2 \rightleftharpoons O+OH$	2.650×10^{16}	-0.670	17041.00
(10)	$2H+Y \rightleftharpoons H_2+Y$	1.000×10^{18}	-1.000	0.00
(11)	$2H+H_2 \rightleftharpoons 2H_2$	9.000×10^{16}	-0.600	0.00
(12)	$2H+H_2O \rightleftharpoons H_2+H_2O$	6.000×10^{19}	-1.250	0.00
(13)	$H+OH+Y \rightleftharpoons H_2O+Y$	2.200×10^{22}	-2.000	0.00
(14)	$H+HO_2 \rightleftharpoons O+H_2O$	3.970×10^{12}	0.000	671.00
(15)	$H+HO_2 \rightleftharpoons O_2+H_2$	4.480×10^{13}	0.000	1068.00
(16)	$H+HO_2 \rightleftharpoons 2OH$	0.840×10^{14}	0.000	635.00
(17)	$H+H_2O_2 \rightleftharpoons HO_2+H_2$	1.210×10^{7}	2.000	5200.00
(18)	$H+H_2O_2 \rightleftharpoons OH+H_2O$	1.000×10^{13}	0.000	3600.00
(19)	$OH+H_2 \rightleftharpoons H+H_2O$	2.160×10^{8}	1.510	3430.00
(20)	$2OH(+Y) \rightleftharpoons H_2O_2(+Y)$	7.400×10^{13}	-0.370	0.00
(21)	$2OH \rightleftharpoons O+H_2O$	3.570×10^{4}	2.400	-2110.00
(22)	$OH+HO_2 \rightleftharpoons O_2+H_2O$	1.450×10^{13}	0.000	-500.00
(23)	$OH+H_2O_2 \rightleftharpoons HO_2+H_2O$	2.000×10^{12}	0.000	427.00
	Duplicated	1.700×10^{18}	0.000	29410.00
(24)	$2HO_2 \rightleftharpoons O_2+H_2O_2$	1.300×10^{11}	0.000	-1630.00
	Duplicated	4.200×10^{14}	0.000	12000.00

3.1.2 San Diego Mech

San Diego Mech was developed in the University of California-San Diego under the philosophy of minimizing the number of species and reactions for the scope of combustion rather than seek for completeness, trying to include all the possible information and generating uncertainties to the results. It is a detailed kinetic mechanism tailored

for many combustion processes from C_0 to C_4 hydrocarbons, with 268 reactions and 57 species [100]. From the complete mechanism, 20 reactions and 9 species are used to describe the combustion of $H_2/O_2/N_2$ mixture, which are listed on table 3.2. Studies using San Diego Mech can be found on references [101–104].

Table 3.2 $H_2/O_2/N_2$ reactions path, pre-exponential factor (A), temperature exponent (b) and activation energy (E_a) extracted from San Diego Mech.

	Reaction	A $[cm, mol, s]$	b $[-]$	E_a $[\mathrm{cal\,mol^{-1}}]$
(1)	$H+O_2 \rightleftharpoons OH+O$	3.520×10^{16}	-0.700	17069.79
(2)	$H_2+O \rightleftharpoons OH+H$	5.060×10^{4}	2.670	6290.63
(3)	$H_2+OH \rightleftharpoons H_2O+H$	1.170×10^{9}	1.300	3635.28
(4)	$H_2O+O \rightleftharpoons 2OH$	7.000×10^{5}	2.330	14548.28
(5)	$2H+Y \rightleftharpoons H_2+Y$	1.300×10^{18}	-1.000	0.00
(6)	$H+OH+Y \rightleftharpoons H_2O+Y$	4.000×10^{22}	-2.000	0.00
(7)	$2O+Y \rightleftharpoons O_2+Y$	6.170×10^{15}	-0.500	0.00
(8)	$H+O+Y \rightleftharpoons OH+Y$	4.710×10^{18}	-1.000	0.00
(9)	$H+O_2(+Y) \rightleftharpoons HO_2(+Y)$	4.650×10^{12}	0.440	0.00
(10)	$HO_2+H \rightleftharpoons 2OH$	7.080×10^{13}	0.000	294.93
(11)	$HO_2+H \rightleftharpoons H_2+O2$	1.660×10^{13}	0.000	822.90
(12)	$HO_2+H \rightleftharpoons H_2O+O$	3.100×10^{13}	0.000	1720.84
(13)	$HO_2+O \rightleftharpoons OH+O2$	2.000×10^{13}	0.000	0.00
(14)	$HO_2+OH \rightleftharpoons H_2O+O2$	7.000×10^{12}	0.000	-1094.65
	Duplicated	4.500×10^{14}	0.000	10929.73
(15)	$2OH(+Y) \rightleftharpoons H_2O_2(+Y)$	9.550×10^{13}	-0.270	0.00
(16)	$2HO_2 \rightleftharpoons H_2O_2 + O_2$	1.030×10^{14}	0.000	11042.07
	Duplicated	1.940×10^{11}	0.000	-1408.94
(17)	$H_2O_2+H \rightleftharpoons HO_2+H_2$	2.300×10^{13}	0.000	7950.05
(18)	$H_2O_2+H \rightleftharpoons H_2O+OH$	1.000×10^{13}	0.000	3585.09
(19)	$H_2O_2+OH \rightleftharpoons H_2O+HO_2$	1.740×10^{12}	0.000	1434.03
	Duplicated	7.590×10^{13}	0.000	7272.94
(20)	$H_2O_2+O \rightleftharpoons HO_2+OH$	9.630×10^{6}	2.000	3991.40

3.1.3 Qin Mech

Qin Mech is a modified GRI-MECH 3.0 mechanism that comprises not only H_2, C_1 and C_2 fuels, but also from C_3 to C_6 hydrocarbon molecules. This kinetic mechanism has a total of 463 reactions, where some of them extracted from GRI-MECH 3.0. From the total reactions, 258 of them are for C_3 hydrocarbon, with a major focus on propane combustion. The C_3 component of the mechanism include reactions of all relevant isomeric forms of C_3H_n with $2 \leq n \leq 8$. Qin Mech has 34 additional species when compared to GRI-MECH 3.0 [105].

3.1.4 AramcoMech_1.3

AramcoMech_1.3 is a chemical kinetic mechanism that characterizes the kinetic and thermochemical properties of a wide range of C_1 to C_4 based hydrocarbon and oxygenated fuels under a variety of experimental circumstances [106]. This kinetic mechanism comprises 253 species and has a total of 1542 reactions, being the most extensive between all mechanisms studied here. There are 24 reactions and 11 species comprising the combustion of $H_2/O_2/N_2$ mixture, which are listed on table 3.3. The Combustion Chemistry Centre at National University of Ireland (NUI) Galway developed it. Starting with a C_1 sub-mechanism, AramcoMech_1.3 was developed in a hierarchical method from the bottom up, adding larger carbon species such as ethane, ethylene, acetylene, higher C_1-C_4 and oxygenated species as it grew. This mechanism has been verified using a wide range of experimental data, including shock tubes, rapid compression machines, flames, and jet-stirred and plug-flow reactors [106]. Studies using AramcoMech_1.3 mechanism can be found on references [107–111].

Table 3.3 $H_2/O_2/N_2$ reactions path, pre-exponential factor (A), temperature exponent (b) and activation energy (E_a) extracted from AramcoMech_1.3.

	Reaction	A $[cm, mol, s]$	b $[-]$	E_a $[\mathrm{cal\,mol^{-1}}]$
(1)	$H+O_2 \rightleftharpoons O+OH$	1.040×10^{14}	0.000	15286.00
(2)	$O+H_2 \rightleftharpoons H+OH$	5.080×10^{4}	2.670	6292.00
(3)	$OH+H_2 \rightleftharpoons H+H_2O$	4.380×10^{13}	0.000	6990.00
(4)	$O+H_2O \rightleftharpoons OH+OH$	2.970×10^{6}	2.020	13400.00
(5)	$H_2+Y \rightleftharpoons H+H+Y$	4.577×10^{19}	-1.400	104400.00
(6)	$O+O+Y \rightleftharpoons O_2+Y$	6.165×10^{15}	-0.500	0.00

Continued on next page

Table 3.3 – *Continued from previous page*

	Reaction	$A\ [cm, mol, s]$	$b\ [-]$	$E_a\ [\mathrm{cal\,mol^{-1}}]$
(7)	$O+H+Y \rightleftharpoons OH+Y$	4.714×10^{18}	-1.000	0.00
(8)	$H+OH+Y \rightleftharpoons H_2O+Y$	3.500×10^{22}	-2.000	0.00
(9)	$H+O_2(+Y) \rightleftharpoons HO_2(+Y)$	4.650×10^{12}	0.440	0.00
(10)	$H+O_2(+AR) \rightleftharpoons HO_2(+AR)$	4.650×10^{12}	0.440	0.00
(11)	$H+O_2(+He) \rightleftharpoons HO_2(+He)$	4.650×10^{12}	0.440	0.00
(12)	$HO_2+H \rightleftharpoons 2OH$	7.079×10^{13}	0.000	295.00
(13)	$H_2+O_2 \rightleftharpoons H+HO_2$	5.176×10^{5}	2.433	53502.00
(14)	$HO_2+O \rightleftharpoons OH+O_2$	3.250×10^{13}	0.000	0.00
(15)	$HO_2+OH \rightleftharpoons H_2O+O_2$	2.456×10^{13}	0.000	-497.00
(16)	$HO_2+HO_2 \rightleftharpoons H_2O_2+O_2$	1.300×10^{11}	0.000	-1630.00
(17)	$HO_2+HO_2 \rightleftharpoons H_2O_2+O_2$	3.658×10^{14}	0.000	12000.00
(18)	$H_2O_2(+H_2O) \rightleftharpoons OH+OH(+H_2O)$	2.000×10^{12}	0.900	48749.00
(19)	$H_2O_2(+Y) \rightleftharpoons OH+OH(+Y)$	2.000×10^{12}	0.900	48749.00
(20)	$H_2O_2+H \rightleftharpoons H_2O+OH$	2.410×10^{13}	0.000	3970.00
(21)	$H_2O_2+H \rightleftharpoons H_2+HO_2$	2.150×10^{10}	1.000	6000.00
(22)	$H_2O_2+O \rightleftharpoons OH+HO_2$	9.550×10^{6}	2.000	3970.00
(23)	$H_2O_2+OH \rightleftharpoons H_2O+HO_2$	1.740×10^{12}	0.000	318.00
(24)	$H_2O_2+OH \rightleftharpoons H_2O+HO_2$	7.590×10^{13}	0.000	7269.00

3.1.5 Boivin Mech

Boivin Mech was developed as a result of a PhD thesis [112], where the author simplified part of San Diego Mech that describes hydrogen combustion. It started from 21 reversible elementary reactions, involving 9 species, and Boivin reduced mechanism ending with 12 reactions and 9 species, which are listed on table 3.4. The simplification was done by comparing the structure of flames and the homogeneous autoignition histories obtained by San Diego Mech and the reduced mechanism proposed. The result is a kinetic mechanism that can describe premixed and nonpremixed flames, autoignition and detonations under conditions of practical interest. Studies using Boivin Mech can be found on references [113–115].

Table 3.4 $H_2/O_2/N_2$ reactions path, pre-exponential factor (A), temperature exponent (b) and activation energy (E_a) extracted from Boivin Mech.

	Reaction		A $[cm, mol, s]$	b $[-]$	E_a $[\mathrm{kJ\,mol^{-1}}]$
(1)	$H+O_2 \rightleftharpoons OH+O$	k_f	3.52×10^{16}	-0.700	71.42
		k_b	7.04×10^{13}	-0.260	0.60
(2)	$H_2+O \rightleftharpoons OH+H$	k_f	5.06×10^{4}	2.670	26.32
		k_b	3.03×10^{4}	2.630	20.23
(3)	$H_2+OH \rightleftharpoons H_2O+H$	k_f	1.17×10^{9}	1.300	15.21
		k_b	1.28×10^{10}	1.190	78.25
(4)	$H+O_2+Y \longrightarrow HO_2+Y$	k_0	5.75×10^{19}	-1.400	0.00
		k_∞	4.65×10^{12}	0.440	0.00
(5)	$HO_2+H \longrightarrow 2OH$		7.08×10^{13}	0.000	1.23
(6)	$HO_2+H \rightleftharpoons H_2+O_2$	k_f	1.66×10^{13}	0.000	3.44
		k_b	2.69×10^{12}	0.360	231.86
(7)	$HO_2+OH \longrightarrow H_2O+O_2$		2.89×10^{13}	0.000	2.08
(8)	$H+OH+Y \rightleftharpoons H_2O+Y$	k_f	4.00×10^{22}	-2.000	0.00
		k_b	1.03×10^{23}	-1.750	496.14
(9)	$2H+Y \rightleftharpoons H_2+Y$	k_f	1.30×10^{18}	-1.000	0.00
		k_b	3.04×10^{17}	-0.650	433.09
(10)	$2HO_2 \longrightarrow H_2O_2+O_2$		3.02×10^{12}	0.000	5.80
(11)	$HO_2+H_2 \longrightarrow H_2O_2+H$		1.62×10^{11}	0.610	100.14
(12)	$H_2O_2+Y \longrightarrow 2OH+Y$	k_0	8.15×10^{23}	-1.900	207.62
		k_∞	2.62×10^{19}	-1.390	214.74

The kinetic mechanisms shown before are different from each other. Each one of those mechanisms are structured with different elements, species, number of reactions. This is because each mechanism has its scopes and the methods used to derive it differ from each other. The kinetic mechanisms also differ from each other on the values of pre-exponential factor, temperature exponent and activation energy. Table 3.5 shows the values of the pre-exponential factor, temperature exponent and activation energy from 2 reactions that

are common to all mechanisms. Its noticeable that each kinetic mechanism uses different values for those variables, with exception o b.

Table 3.5 Values of A [cm,mol,s], b [-] and E_a [cal mol^{-1}] for GRI-MECH 3.0, San Diego Mech, AramcoMech_1.3 and Boivin Mech.

	$HO_2+H \rightleftharpoons 2OH$			$2HO_2 \rightleftharpoons H_2O_2 + O_2$		
Mechanism	A	b	E_a	A	b	E_a
GRI-MECH 3.0	0.840×10^{14}	0.00	635.00	1.30×10^{11}	0.00	-1630.00
San Diego Mech	7.080×10^{13}	0.00	294.93	1.94×10^{11}	0.00	-1408.94
AramcoMech_1.3	7.079×10^{13}	0.00	295.00	1.300×10^{11}	0.00	-1630.00
Boivin Mech	7.080×10^{13}	0.00	294.26	3.020×10^{12}	0.00	1387.56

A representation of the results generated by each kinetic mechanism is shown on figure 3.1. The kinetic mechanisms can generate similar or different results, depending on the kinetic values entered into them. In addition, different reactions have more or less influence on the overall speed of reactions, and this depends on the techniques used to construct the mechanism. Looking at each reaction that makes up the kinetic mechanism individually is not correct, but looking at the result generated by the entire mechanism is the correct way to verify if it fits the study in case.

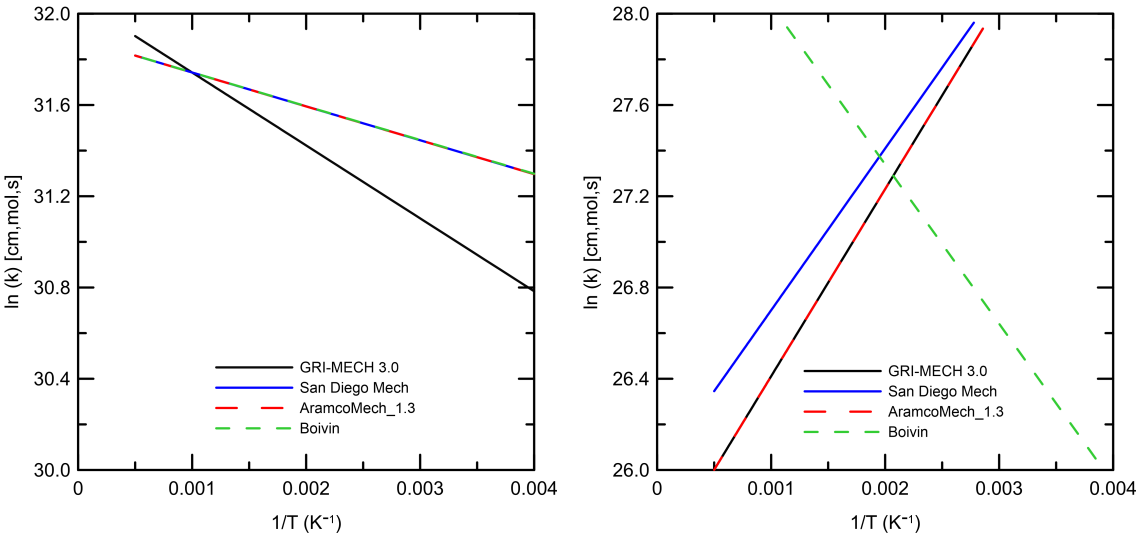

(a) $HO_2+H \rightleftharpoons 2OH$ **(b)** $2HO_2 \rightleftharpoons H_2O_2 + O_2$

Figure 3.1 Representation of ln (k) vs 1/T using the kinetic data from GRI-MECH 3.0, San Diego Mech, AramcoMech_1.3 and Boivin Mech for two H_2/O_2 combustion reactions.

3.1.6 Thermodynamics data

The combustion process calculation requires energy balances. These balances are done using species thermodynamic data used to calculate parameters like heat capacity (C_p), enthalpy (H) and entropy (S), and those relation with temperature. Calculations are carried out with equations (6-8), that are known as NASA polynomials [94, 116]. Such polynomials appeared like an approach to smooth out measurement scatter of the data acquired and a compact manner to publish a ton of data in a world when computers were not even envisioned [117].

$$\frac{C_p^\circ}{R} = a_1 + a_2 T + a_3 T^2 + a_4 T^3 + a_5 T^4 \tag{6}$$

$$\frac{H_T^\circ}{RT} = a_1 + a_2 \frac{T}{2} + a_3 \frac{T^2}{3} + a_4 \frac{T^3}{4} + a_5 \frac{T^4}{5} + \frac{a_6}{T} \tag{7}$$

$$\frac{S_T^\circ}{R} = a_1 lnT + a_2 T + a_3 \frac{T^2}{2} + a_4 \frac{T^3}{3} + a_5 \frac{T^4}{4} + a_7 \tag{8}$$

C_p°: specific molar heat capacity at standard condition, in $\mathrm{J\,mol^{-1}\,K^{-1}}$;

R: ideal gas constant, $8.314\,\mathrm{J\,mol^{-1}\,K^{-1}}$;

T: temperature in K;

H_T°: molar enthalpy at standard condition, in $\mathrm{kJ\,mol^{-1}}$;

S_T°: molar entropy at standard condition, in $\mathrm{J\,mol^{-1}\,K^{-1}}$;

a_n: specific coefficients for a species imported to NASA polynomials ($n = 1$ to 7).

Equation (7) is derived from another correlation, where the enthalpy of formation ($\Delta_f H_{298}^\circ$) of species j at the reference temperature of 298 K is added to the integration of the specific heat capacity, from reference temperature (bottom limit) to a given temperature (upper limit). Equation (9) shows that correlation.

$$H_T^\circ = \Delta_f H_{298}^\circ + \int_{298}^{T} C_p^\circ dT \tag{9}$$

The values of C_p°, H_T° and S_T° are divided by R (and by T in the case of enthalpy) to obtain dimensionless values. The coefficients a_n are divided in two ranges of temperature, one from 200 to 1000 K and 1000 to 6000 K, so the data obtained are better fitted. An example of a thermodynamic data used for H_2, O_2 and H_2O are shown on figure 3.2 [117].

```
THERMO
   300.000  1000.000  5000.000
H2                TPIS78H   2    0    0    0G   200.000  6000.00  1000.00      1
 2.93286575E+00 8.26608026E-04-1.46402364E-07 1.54100414E-11-6.88804800E-16    2
-8.13065581E+02-1.02432865E+00 2.34433112E+00 7.98052075E-03-1.94781510E-05    3
 2.01572094E-08-7.37611761E-12-9.17935173E+02 6.83010238E-01 0.00000000E+00    4
O2                RUS 89O   2    0    0    0G   200.000  6000.00  1000.00      1
 3.66096065E+00 6.56365811E-04-1.41149627E-07 2.05797935E-11-1.29913436E-15    2
-1.21597718E+03 3.41536279E+00 3.78245636E+00-2.99673416E-03 9.84730201E-06    3
-9.68129509E-09 3.24372837E-12-1.06394356E+03 3.65767573E+00 0.00000000E+00    4
H2O               L 5/89H   2 O  1    0    0G   200.000  6000.00  1000.00      1
 0.26770389E+01 0.29731816E-02-0.77376889E-06 0.94433514E-10-0.42689991E-14    2
-0.29885894E+05 0.68825500E+01 0.41986352E+01-0.20364017E-02 0.65203416E-05    3
-0.54879269E-08 0.17719680E-11-0.30293726E+05-0.84900901E+00-0.29084817E+05    4
```

Figure 3.2 Thermodynamic data extracted from AramcoMech_1.3. First set of 7 constants (lines 2 and 3) belongs to the 1000-6000 K interval, the second set of 7 constants (lines 3 and 4) belongs to the 200-1000 K interval. Last constant is the value of $\Delta_f H_{298}/R$ [106].

3.1.7 Species reactivity

The elements, chemical species, reaction blueprints, stoichiometry and Arrhenius kinetic parameters makes the species reactivity on the kinetic mechanisms. A representation of how elements and species are organized in the chemical mechanisms is show on figure 3.3.

```
ELEMENTS
O   H   C   N   AR
END
SPECIES
H2          H           O           O2          OH          H2O         HO2         H2O2
C           CH          CH2         CH2(S)      CH3         CH4         CO          CO2
HCO         CH2O        CH2OH       CH3O        CH3OH       C2H         C2H2        C2H3
C2H4        C2H5        C2H6        HCCO        CH2CO       HCCOH       N           NH
NH2         NH3         NNH         NO          NO2         N2O         HNO         CN
HCN         H2CN        HCNN        HCNO        HOCN        HNCO        NCO         N2
AR          C3H7        C3H8        CH2CHO      CH3CHO
```

Figure 3.3 Elements and species representation in GRI-MECH 3.0 [94].

Data given in reaction section are pre-exponential factor (A), that is dependent on reaction order, temperature exponent (b) and activation energy (E_a). Figure 3.4 shows how those parameters are written in the kinetic mechanism.

```
                                A          b          Ea
H+HO2=O+H2O                 3.970E+12    0.000    671.00
H+HO2=O2+H2                 4.480E+13    0.000   1068.00
H+HO2=2OH                   0.840E+14    0.000    635.00
H+H2O2=HO2+H2               1.210E+07    2.000   5200.00
H+H2O2=OH+H2O               1.000E+13    0.000   3600.00
```

Figure 3.4 Collection of reaction data with reaction blueprint, stoichiometry and data used in Arrhenius equation. Extracted from GRI-MECH 3.0. A [$cm\,mol\,s$], b [$-$], E_a [$\mathrm{cal\,mol^{-1}}$] [94].

The simplest reaction type is a homogeneous reaction with a pressure-independent rate coefficient and mass action kinetics. A homogeneous reaction can be written as equation (10), where A and B are the reactants, C and D are the products of a reversible reaction.

$$\mathrm{A} + \mathrm{B} \rightleftharpoons \mathrm{C} + \mathrm{D} \tag{10}$$

The forward rate constant k_f is then defined as a modified Arrhenius function, as shown on equation (11).

$$k_f = AT^b e^{-E_a/RT} \tag{11}$$

The forward reaction rate is calculated as shown on equation (12), where [A] and [B] are the concentrations of the reactants A and B respectively.

$$R_f = [\mathrm{A}][\mathrm{B}]k_f \tag{12}$$

Chemical reactions can also be defined as three-body reactions, falloff reactions, or chemically-activated reactions. A collision partner (Y) in three-body reactions takes away excess energy to stabilize the molecule. Different species may have different degrees of effectiveness as a collision partner and the efficiency of a collision partner is defined in the kinetic mechanism. Three-body reactions can be written as equation (13), where A and B are the reactant species, AB the product species and Y a collision partner.

$$\mathrm{A} + \mathrm{B} + \mathrm{Y} \rightleftharpoons \mathrm{AB} + \mathrm{Y} \tag{13}$$

The forward reaction rate (R_f) of a three-body reaction is written as equation (14).

$$R_f = [\mathrm{A}][\mathrm{B}][\mathrm{Y}]k_f \tag{14}$$

Falloff reactions have a first-order in [Y] at low pressures, like in Three-Body, but as the concentration of the same increases, it becomes zero-order in [Y]. The dissociation/association reactions of polyatomic molecules are an example of this. The expression for the rate coefficient for a falloff reaction is written as equation (15), where k_{f0} is the forward rate constant with low collision partner concentration, and $k_{f\infty}$ is the forward rate constant with high collision partner concentration. Falloff reactions can also be defined as troe falloff-reaction, which have some modifications on the equation [118].

$$k_f([\mathrm{Y}]) = \frac{k_{f0}[\mathrm{Y}]}{1 + \dfrac{k_{f0}[\mathrm{Y}]}{k_{f\infty}}} \tag{15}$$

A falloff reaction is set in the kinetic mechanism as shown on figure 3.5.

```
falloff_reaction( "2 OH (+ Y) <=> H2O2 (+ Y)",
         kf = [7.40000E+13, -0.37, 0],
         kf0   = [2.30000E+18, -0.9, -1700],
         falloff = Troe(A = 0.7346, T3 = 94, T1 = 1756, T2 = 5182),
         efficiencies = " AR:0.7  C2H6:3  CH4:2  CO:1.5  CO2:2  H2:2  H2O:6 ")
```

Figure 3.5 Falloff reaction specifications extracted from GRI-MECH 3.0 . Line 1 sets the equation. On line 2, k_f represents $k_{f\infty}$ and the three values on brackets are Arrhenius equation parameters with high Y concentration Line 3 sets the values from Arrhenius equation with low Y concentration. Line 4 sets troe parameters and line 5 the collision partners efficiencies [94].

Due to collisional stabilization of a reaction intermediate in chemically-activated reactions, the rate decreases as the pressure rises. Chemically-activated reactions, like falloff reactions, are described by combining a low-pressure and a high-pressure rate expression. The forward rate constant is stated as proportional to the low-pressure rate constant in this case can be written as equation (16) [119].

$$k_f(T, \frac{k_{f0}[\mathrm{Y}]}{k_{f\infty}}) = k_0 \left(\frac{1}{1 + \frac{k_{f0}[\mathrm{Y}]}{k_{f\infty}}} \right) \tag{16}$$

An example of a three-body reaction is the reaction (1) from GRI-MECH 3.0 and an example a troe falloff-reaction is the reaction (20) from GRI-MECH 3.0 (table 3.1).

3.1.8 Transport data

The analysis of species mass diffusion coefficient (D), dynamic viscosity (μ), thermal conductivity (γ), and thermal diffusion coefficient (D^T) is required to characterize the molecular transport of species, momentum, and energy in a multicomponent reactive environment. These are molecular properties of a substance that show the rate at which particular momentum, heat, or mass is transported per unit volume [120, 121]. A representation of how transport data is organized is shown on table 3.6.

The transport data is organized in 7 columns, where in the first one, the species name is given, in the second one the geometry is given. This geometry can be 0 if the species is a single atom, 1 if the species is linear an 2 if it is nonlinear. In the third column the value of Lennard-Jones potential well depth is indicated ($\varepsilon/\mathrm{k_B}$), the fourth column holds the values of Lennard-Jones collision diameter (σ) in angstrom (Å), the fifth column represents the values of dipole moment (η) in Debye, the sixth column hold the values of polarizability (α) in $\mathrm{Å}^3$ and the final column has the values of rotational relaxation collision number Z_{rot} at

Table 3.6 Transport section from kinetic mechanism, with the species molecular formula and the values of the constants needed to compute transport data. Adapted from CHEMKIN [120].

Species	Geometry	ε/k_B	σ	η	α	Z_{rot}
H_2	1	38.000	2.920	0.000	0.790	280.000
O_2	1	107.400	3.458	0.000	1.600	3.800
H_2O	2	572.400	2.605	1.844	0.000	4.000

298 K. The calculations performed to find the values of those transport properties are too extensive to be explained in this section, but they can be found on CHEMKIN transport manual [120].

3.2 Adiabatic flame temperature

The adiabatic flame temperature (T_b) is defined as the temperature attained by the burned gas mixture when all the heat generated by the chemical reaction is released and the chemical equilibrium is reached [122]. The adiabatic flame temperature can be influenced by several parameters, namely, the inlet gas temperature in the burner, also called unburned gas temperature (T_u), pressure (P), fuel type and composition, and the unburned mixture equivalence ratio. In this study, only adiabatic flame temperatures under constant pressure were evaluated.

Adiabatic flame temperature calculations were performed, by finding the composition of the burned gas in the state of chemical equilibrium, and then performing a heat balance to the system. To calculate the composition of the gas in equilibrium, a minimization of Gibbs free energy (G) is performed, maintaining constant the enthalpy and the pressure. Enthalpy is kept constant because it is considered that all the energy generated by the combustion is only used to heat the flame, so an adiabatic process. The pressure is maintained constant because the flame is said to be located in a open environment, so the available volume is not a constraint.

For a mixture of number of species (NS), Gibbs free energy can be calculated as the sum of the number of moles of species j (n_j) multiplied by the chemical potential of the same species (g_j), as it is represented by equation (17).

$$G = \sum_{j=1}^{NS} g_j n_j \tag{17}$$

The minimization of Gibbs free energy is subject to constraints, such as showed in equation (18), where a_{ij} is said to be the stoichiometric coefficient ($\mathrm{kg\,atom}_i$ of element i per $\mathrm{kg\,mol}_j$ of species j) and b_i° is assigned mass of atoms from element i per mass of total reactant ($\mathrm{kg\,atom}_i.\mathrm{kg}^{-1}$). It means that the total mass of a certain atom of the reactants must be same of the products. Also, the number of moles from one compound can not be negative.

$$\sum_{j=1}^{NS} a_{ij} n_j - b_i^\circ = 0 \tag{18}$$

A series of assumptions and other deductions were made to achieve the final equations, as it can be seen on NASA article published in 1994 [123]. It is said in that article that the equations required to obtain composition in chemical equilibrium are not all linear in the composition variables, so a iteration method was adopted. This iteration method is used in the current work and all the information about the equations can be found on the NASA article cited before.

3.3 Laminar flame speed

The propagation rate of the normal flame front relative to the unburned mixture is known as laminar flame speed (S_L), and it is affected by fuel composition, unburned gas temperature, pressure and premixture equivalence ratio. It is an important quality for a premixed flame since it encapsulates the core information of the combustible hydrocarbon mixture's diffusivity, reactivity, and exothermicity. On a practical level, laminar flame speed is linked to the combustor's burning rate, which can affect combustion efficiency and emissions. Values for laminar flame speeds can be utilized as direct validation objectives for chemical kinetic models or as indirect validation targets for turbulent combustion models [124].

The practical measurement of the laminar flame speed can be performed in several ways, those being the burner method [125], cylindrical tube method [126], soap bubble method [127], closed spherical bomb method [128] and flat-flame burner method [129]. The former one is widely used to measure the laminar flame speed for its simplicity. The speed of the flame must match the normal component of unburned gas average speed (u_{av}) at each point in order for it to remain stationary. By knowing it, one can measure the angle α between the normal component and the inner flame cone (figure 3.6), and use equation (19) to calculate the laminar flame speed.

$$S_L = u_{av}\ sin\ \alpha \tag{19}$$

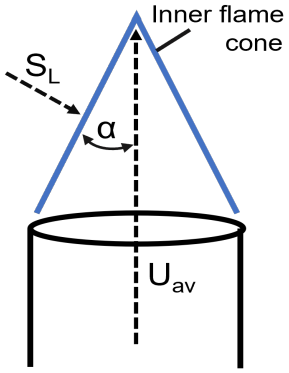

Figure 3.6 Laminar flame speed equals normal component of unburned gas velocity (u_{av}). Adapted from Turns *et al.* [90].

The later one is the said to offer the simplest flame front and to generate the most accurate results [130]. In the numerical simulations carried out, the uni dimensional flat flame burner method was chosen, as the calculation used are easier to simulate. In this method, a porous metal disk or a series of small tubes with 1 mm or less is placed in the exit of the flow tube, creating then a flat flame. The unburned gas flow is adjusted to avoid a cone owing (higher unburned gas velocity than flame speed) and flashback (lower unburned gas velocity than flame speed) [130]. An illustration of a premixed flat-flame burner is shown on figure 3.7.

The numerical solution to this problem is developed by creating the environment called FreeFlame. In this method, a domain of type IdealGasFlow named 'flame' set to free flow, will be created to represent the flame. The three domains comprising the stack are stored as self.inlet, self.flame, and self.outlet. The domain size is defined by the width, as it defines a grid on the interval $[0, z]$ with internal points determined automatically by the solver.

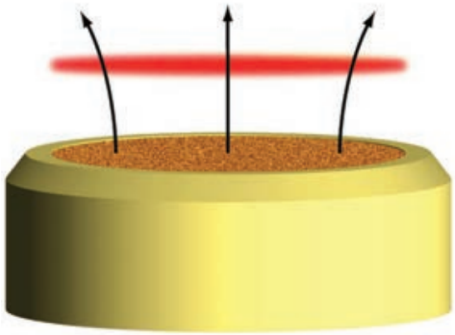

Figure 3.7 Example of a laminar flat-flame burner. Source: Kee *et al.* [131].

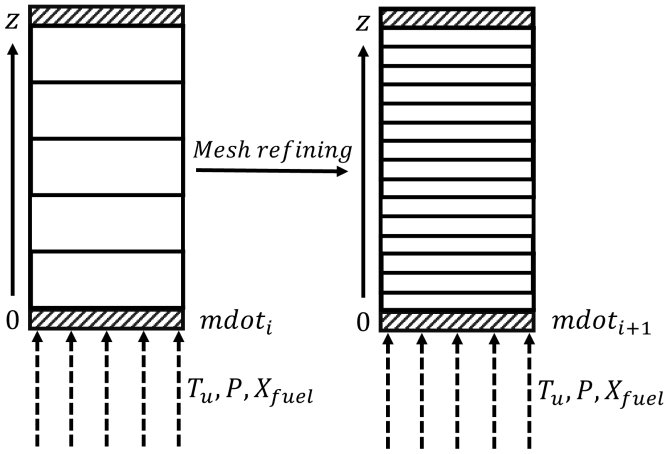

Figure 3.8 Representation of numerical solution by mesh refining.

The solver will arbitrate a value for the input flow rate of the unburned gases and solve a series of equations predefined by the model. If the criteria are not satisfied, a new iteration is performed, where the mesh of the domain is refined to obtain a better resolution, as is schematized on figure 3.8. This process is repeated until the point where the criteria are satisfied. Then the value of $\dot{m}$ is determined and the laminar flame speed is evaluated at the cold boundary, $S_L = \dot{m}''/\rho$, where ρ is the density of the unburned gases ($\mathrm{kg\,m^{-3}}$). Additional information can be found at *Cantera* website [119, 131].

3.4 Flame stability and operation limits

A relevant topic is related to the operating limits, stability, and design of burners in which H_2 containing fuels will be used. It is important to design Bunsen type burners such as cooking stoves, as well as other combustion systems that uses laminar flames. The design of those burners is done based on Glassman diagrams [130], which is illustrated in figure 3.9.

This method of finding the operation limits for a Bunsen burner is followed with some constraints. First, an accurate Bunsen flame cone cannot form unless the average premixed gas velocity is at least twice S_L. Furthermore, if the average velocity is five times S_L, the fuel penetrates the Bunsen cone tip, according to experimental results. Secondly, the gradients of flashback and blowoff have to be considered. Flashback occurs when the flame enters and propagates through the burner tube or port without being quenched, while the condition in which the flame is not attached to the burner tube or port but is stabilized at a distance from the port is referred to as blowoff. Finally, as the flow characteristic in this study must be laminar, the Reynolds number (N_{Re}) must be lower

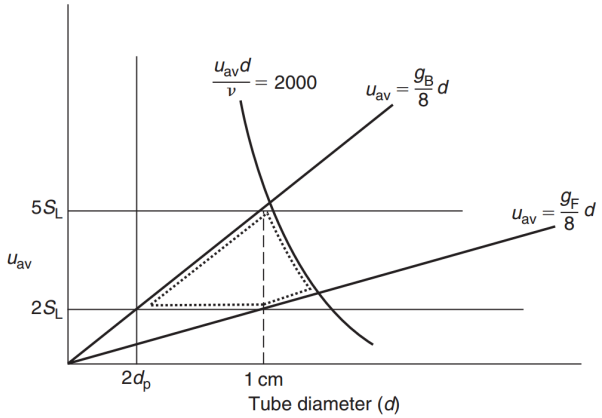

Figure 3.9 Glassman stability diagram highlights the operation limits of Bunsen burner [130].

than 2000, otherwise the flow becomes turbulent. When all the constraints are met, a plot of the unburned gas average velocity vs the tube diameter is made and the dashed area (figure 3.9) will generate the operation zone [90, 130]. Equation (20) takes into account the flashback and blowoff gradients.

$$u_{av} = \frac{g_{(B,F)}}{8} d \tag{20}$$

Where u_{av} is the average velocity in $(\mathrm{m\,s^{-1}})$, $g_{B,F}$ is the flashback and blowoff gradients and d is the Bunsen burner diameter in (m). It takes into account the instability generated by the flashback and blowoff.

Blowoff (g_B) and flashback (g_F) gradients in $(\mathrm{s^{-1}})$ are calculated following equations (21) and (22) and takes into account hydrogen $(X_{\mathrm{H_2}})$ content in a mixture with $\mathrm{CH_4}$ and the equivalence ratio.

$$g_B = (249\,X_{\mathrm{H_2}} + 6036)\,\phi + (-160\,X_{\mathrm{H_2}} - 4050) \tag{21}$$

$$g_F = (-127\,X_{\mathrm{H_2}} - 3807)\,\phi^2 + (257\,X_{\mathrm{H_2}} + 7729)\,\phi + (-144\,X_{\mathrm{H_2}} - 3461) \tag{22}$$

The laminar flow boundary is calculated with equation (23), and takes into account that laminar regime is obtained with a N_{Re} lower than 2000 [132].

$$\frac{u_{av}\,d}{\nu} = 2000 \tag{23}$$

Where ν is the kinematic viscosity in $(\mathrm{m^2\,s^{-1}})$. Kinematic viscosity is defined as the quotient between dynamic viscosity and density $(\nu = \frac{\mu}{\rho})$.

An optimum burner operation point/area can also be obtained, depending on the system characteristics. This point is usually around 1 cm when using fuel gases. The optimum operation point/area will provide the most flow velocities fluctuation without causing instability [130, 133].

3.5 Cantera

All simulations were carried out using *Cantera*, an open-source suite of tools for problems involving chemical kinetics, thermodynamics, and transport processes [119]. *Cantera* is a library that can be used in several program language, that being *Python*, MATLAB or in applications written in C/C++ or Fortran 90. *Cantera* is currently used in combustion, detonations, electrochemical energy conversion and storage, fuel cells, batteries, aqueous electrolyte solutions, plasma, and thin film deposition, among other applications.

Cantera community offers a large number of premade algorithms as example, and they are divided subgroups, that being thermodynamics, kinetics, transport, reactors networks, one-dimensional flames, multiphase mixtures and surface chemistry. All simulations in this work were performed under *Python* environment. Adiabatic flame temperature and laminar flame speed calculations were carried out using *Cantera*, with shared algorithms by *Cantera* community [119]. The algorithms used in this work were adiabatic.py on section 4.1 and adiabatic_flame.py on section 4.2, where the former one is used to compute the adiabatic flame temperature and the later one to calculate the laminar flame speed. Other algorithms where also used to calculate the specific heat capacity, density and dynamic viscosity.

3.6 Algorithm 1: Adiabatic flame temperature

The algorithm used to calculate the adiabatic flame temperature, running in *Python* environment was used, and it can be found as Algorithm 3.1. In this algorithm, 4 important parameters can be manipulated, namely the unburned gas temperature (K), pressure (Pa), the reaction mechanism, and premixture composition (moles). Other simulation parameters can also be manipulated. To solve the problem, Gibbs minimization energy method is used, because it generates feasible results. The parameters held constant were entalphy (H) and pressure (P), meaning that no energy is lost (adiabatic conditions) and the volume of the system changes to maintain constant pressure.

The output file is a sheet with data containing a range of ϕ, defined on the algorithm, and the respective adiabatic flame temperatures and species molar fraction.

```
1  """ Adiabatic flame temperature and equilibrium composition for a fuel/
       air mixture as a function of equivalence ratio, including formation
        of solid carbon."""
2  import cantera as ct
3  import numpy as np
```

```
4     import sys
5     import csv
6     ######################################################################
7     # Edit these parameters to change the initial temperature, the pressure
          , and the phases in the mixture.
8     Tu = 300.0
9     P = 101325.0
10    # phases
11    gas = ct.Solution('gri30.cti')
12    carbon = ct.Solution('graphite.xml')
13    # the phases that will be included in the calculation, and their
          initial moles
14    mix_phases = [(gas, 1.0), (carbon, 0.0)]
15    # gaseous fuel species
16    fuel_species = 'H2:1.0, CH4:1.0, CO2:1.0'
17    # equivalence ratio range
18    npoints = 1200
19    phi = np.linspace(0.3, 1.5, npoints)
20    ######################################################################
21    mix = ct.Mixture(mix_phases)
22    # create some arrays to hold the data
23    tad = np.zeros(npoints)
24    xeq = np.zeros((mix.n_species,npoints))
25    for i in range(npoints):
26    # set the gas state
27    gas.set_equivalence_ratio(phi[i], fuel_species, 'O2:1.0, N2:3.728')
28    # create a mixture of 1 mole of gas, and 0 moles of solid carbon.
29    mix = ct.Mixture(mix_phases)
30    mix.T = Tu
31    mix.P = P
32    # equilibrate the mixture adiabatically at constant P
33    mix.equilibrate('HP', solver='gibbs', max_steps=1000)
34    tad[i] = mix.T
35    print('At phi = {0:12.4g}, Tad = {1:12.4g}'.format(phi[i], tad[i]))
36    xeq[:,i] = mix.species_moles
```

Algorithm 3.1 Python adiabatic flame temperature code.

3.7 Algorithm 2: Laminar flame speed

To calculate the laminar flame speed, a code running in *Python* environment was used, and the algorithm used is presented as Algorithm 3.2. The parameters that can be

Table 3.7 Default value of width, ratio, slope and curve from algorithm 3.2.

Parameter	Width (m)	Ratio	Slope	Curve
Value	0.03	3.00	0.06	0.12

manipulated are the unburned gas temperature (K), pressure (Pa), the reaction mechanism, and premixed gas composition (moles). The numerical parameters of the calculation method that can be manipulated are width, ratio, slope and curve, all having some effect on the final result. Width is the domain size where the calculations are performed. Ratio is the amount of additional points that will be added if the ratio of the spacing on either side of a grid points exceed the value set (value must be greater than 2). Slope is defined ans the maximum difference in value between two adjacent points, scaled by the maximum difference in the profile, and it adds points in regions of high slope (value between 0.0 and 1.0). Curve is the maximum difference in slope between two adjacent intervals, scaled by the maximum difference in profile, and it adds points in regions of high curvature (value between 0.0 and 1.0). The default values of those parameters can be seen on table 3.7.

Other important parameters are the transport models. They are usually solved using two methods, with the first one being 'Mix', a model that implements a mixture-average formulation, and 'Multi' that is a model that used multicomponent properties. In general results generated by 'Multi' transport model are more accurate, but takes more time calculate. The algorithm use both methods, the 'Mix' as a first approach and 'Multi' as a refinement.

The output file is a sheet with the values of grid position, the velocity at a certain grid value, the temperature at a certain grid value and the species molar fraction. The first value of velocity is the laminar flame speed.

```
"""A freely-propagating, premixed flat flame with multicomponent
    transport properties."""
import cantera as ct
# Simulation parameters
p = ct.one_atm  # pressure [Pa]
Tu = 300.0  # unburned gas temperature [K]
# premixed gas composition
reactants = 'H2:2.8, CH4:0.0, O2:1.0, N2:3.728'
width = 0.03  # m
loglevel = 0  # amount of diagnostic output (0 to 8)
```

```
    # IdealGasMix object used to compute mixture properties, set to the
        state of the upstream fuel-air mixture
    gas = ct.Solution('gri30.cti')
    gas.TPX = Tu, p, reactants
    # Set up flame object
    f = ct.FreeFlame(gas, width=width)
    f.set_refine_criteria(ratio=3, slope=0.06, curve=0.12)
    f.show_solution()
    # Solve with mixture-averaged transport model
    f.transport_model = 'Mix'
    f.solve(loglevel=loglevel, auto=True)
    # Solve with the energy equation enabled
    f.save('h2_adiabatic.xml', 'mix', 'solution with mixture-averaged
        transport')
    f.show_solution()
    print('mixture-averaged flamespeed = {0:7f} m/s'.format(f.velocity[0]))
    # Solve with multi-component transport properties
    f.transport_model = 'Multi'
    f.solve(loglevel) # don't use 'auto' on subsequent solves
    f.show_solution()
    print('multicomponent flamespeed = {0:7f} m/s'.format(f.velocity[0]))
    f.save('h2_adiabatic_flamespeed.xml','multi', 'solution with
        multicomponent transport')
    # write the velocity, temperature, density, and mole fractions to a CSV
         file
    f.write_csv('gri_flamespeed_1.0_300K_100%H2.csv', quiet=False)
```

Algorithm 3.2 Python laminar flame speed code.

3.8 Algorithms 3 and 4: Density and viscosity

Other algorithms were also used to obtain the values of specific heat capacity, density and dynamic viscosity. Those following scripts were personally developed for this work. Algorithm 3.3 is a simple algorithm that gives C_p in function of a range of temperatures, while algorithm 3.4 gives ρ and μ. In both algorithms, the inputs are fuel composition and stoichiometry of the reactants, unburned gas temperature (K) and pressure (Pa). The output file of algorithm 3.3 is a file with a range of temperatures and specific heat capacities ($\mathrm{kJ\,kmol^{-1}\,K^{-1}}$), while the output of algorithm 3.4 is a simple cell with the values of density ($\mathrm{kg\,m^{-3}}$) and viscosity ($\mathrm{kg\,m^{-1}\,s^{-1}}$).

```
import cantera as ct
import numpy as np
import csv
#Gas mechanism
gas1 = ct.Solution('gri30.xml')
#step size
step=10
#Initial temperature
Ti=1500
#Final temeprature
Tf=2500
#Number of steps
npoints = Tf
h2 = np.zeros(npoints)
Temp = np.zeros(npoints)
for i in range(Ti, Tf, step):
#Temprature and pressure setup
gas1.TP = i, 1*ct.one_atm
#Composition setup
gas1.X = 'H2:2.0, O2:1.0, N2:3.728'
#Equilibrate (opcional)
#gas1.equilibrate('TP', solver='gibbs', max_steps=1000)
h2[i] = gas1.cp_mole/1000
Temp[i] = i
print('At Temp(K) = {0:12.4g}, Cp(kJ/kmol*K) = {1:12.4g}'.format(Temp[i
    ], h2[i]))
```

Algorithm 3.3 Python specific heat capacity code.

```
import cantera as ct
#Gas mechanism
gas1 = ct.Solution('gri30.yaml')
#Gas composition, temperature and pressure
gas1.TPX = 300, 101325, 'H2:2.0, O2:1.0, N2:3.728'
#Equilibrate (optional)
#gas1.equilibrate('TP')
#Rquest the output density and viscosity
x=gas1.density_mass
y=gas1.viscosity
gas1()
```

Algorithm 3.4 Python density and viscosity code.

Chapter 4

Results and discussion

4.1 Adiabatic flame temperature

This first section from the results will show the influence of some parameters, namely equivalence ratio (ϕ), pressure (P), unburned gas temperature (T_u), as well as the composition of fuel on the adiabatic flame temperature (T_b). Kinetic mechanisms tested were GRI-MECH 3.0, San Diego Mech, AramcoMech_1.3 and Boivin Mech. Pressures used varied from 0.5 to 20 atm, unburned gas temperature from 250 to 500 K, using fuels of pure H_2, pure CH_4, a fuel blend of H_2/biogas, with a hydrogen fraction from 0 to 100 %. Oxidizer used in this work is air, with a composition of 20.94 % of O_2 and 78.08 % of N_2 [93]. In the final part of this section, a set of empirical equations were proposed, converging to a final form after some tests. The algorithm used in this work were algorithms 3.1 and 3.3

4.1.1 Equivalence ratio

The equivalence ratio has a big impact on the flame temperature and show some interesting behaviours. This study was carried out using GRI-MECH 3.0, with a unburned gas temperature of 300 K, at 1 atm using a $H_2/O_2/N_2$ premixture. Typical data of the effect of ϕ on the values of T_b of premixed gas flames are presented in figure 4.1.

While flame is at lean condition, the flame temperature increases along with the increase of ϕ. In rich condition, the flame temperature decreases when the value of ϕ increase. These results match what is expected [130], because when the system is in the lean condition, the heat generated by the combustion is also used to heat up the excess of O_2/N_2 in the premixture. In the rich condition, there is not enough oxygen to completely oxidize the fuel, so there are less energy released.

The maximum adiabatic flame temperature ($T_{b.max}$) of a fuel is not located at stoichiometry, but slightly shifted into the rich zone, which is due to dissociation reactions. Dissociation reactions occurs when a diatomic element split into radicals and to do so, part of the energy released in the combustion is absorbed, which lowers the temperature. This

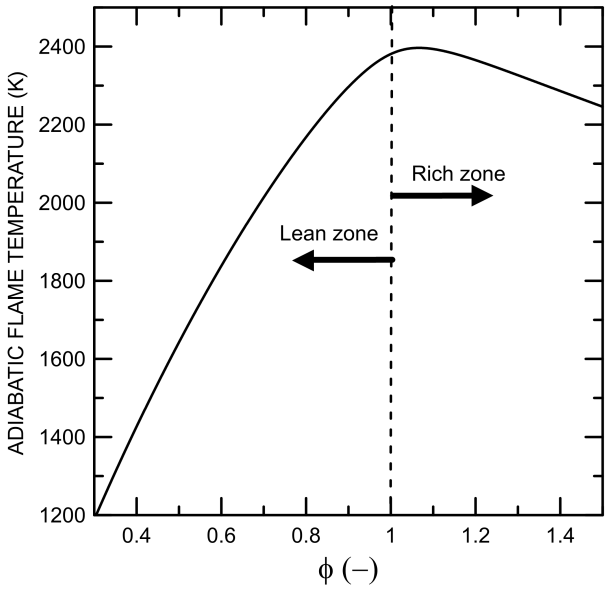

Figure 4.1 GRI-MECH 3.0 mechanism: effect of premixture equivalence ratio in adiabatic flame temperature of $H_2/O_2/N_2$ flames at 1 atm and 300 K.

effect is even more visible near the stoichiometric value, where dissociation is even greater [134]. The equivalence ratio, where adiabatic flame temperature is at maximum is called ϕ_{max}. The maximum adiabatic flame temperature obtained was 2396 K, with a value of ϕ_{max} of 1.06.

The rate of change of adiabatic flame temperature in function of ϕ on lean condition, with $0.3 < \phi < 0.75$, has a value of 2007 K/ϕ unit using hydrogen flame, which is considerably higher than the rate of change on rich condition, with ϕ between 1.2 and 1.5, and it has a value of 401.09 K/ϕ unit. So, adiabatic flame temperature cools down easily on lean condition than on rich.

The equivalence ratio also influences the concentration of radicals that are produced during combustion, with the most important ones being O, OH, H, HO_2, also the species H_2O_2. For $H_2/O_2/N_2$ flames the most significant radicals exhibit a maximum concentration around stoichiometry (figure 4.2). Maximum concentrations were observed at lean condition for oxygenated species and on rich condition for non-oxygenated species, which is expected, since on lean condition there is an excess of oxygen, while on rich condition there is an excess of hydrogen. The highest concentrations were obtained by radicals H, O and OH. For the oxygenated species, maximum concentrations were observed at $\phi = 0.93$, 0.95, 0.83 and 0.87 for O, OH, HO_2 and H_2O_2, while for the non-oxygenated species, the maximum concentration was obtained with a ϕ of 1.23.

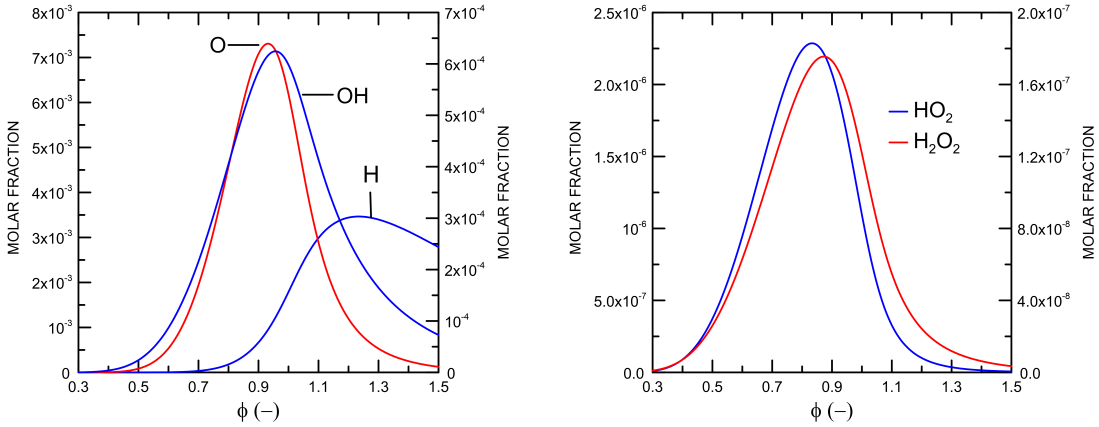

(a) Radicals OH, H and O

(b) Radical HO_2 and species H_2O_2

Figure 4.2 GRI-MECH 3.0 mechanism: concentration of selected radicals in burned gas of $H_2/O_2/N_2$ flames at 1 atm and 300 K of unburned gas temperature. **(a)** Concentration of OH, H radicals (left axis) and O radical (right axis). **(b)** Concentration of HO_2 radical (left axis) and species H_2O_2 (right axis).

4.1.2 Mechanism exploited

To validate numerical results, a direct comparison with experimental values collected in literature was used. The comparison was performed using a fuel premixture of hydrogen in air, at 1 atm and unburned gas temperature of 300 K. Each kinetic mechanism has a scope, some focusing on hydrocarbons combustion, others on hydrocarbon and hydrogen and some only on hydrogen. This study was done varying the value of the equivalence ratio, from 0.3 to 1.5 and observing the influence on the adiabatic flame temperature. The results obtained are shown on figure 4.3.

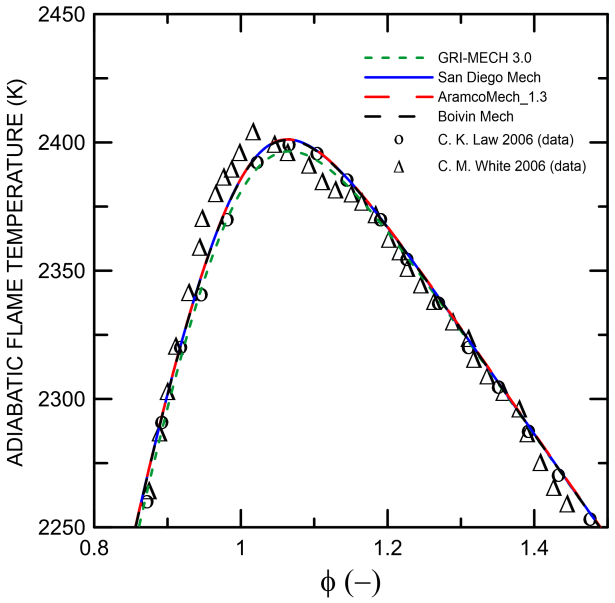

Figure 4.3 Adiabatic temperatures of $H_2/O_2/N_2$ flames (1 atm and 300 K). Lines: kinetic simulation results using GRI-MECH 3.0 [94], San Diego [100], AramcoMech_1.3 [106], Boivin Mech [112]; Symbols: bibliographic reference data [134, 135].

Results obtained, using the mechanisms GRI-MECH 3.0, AramcoMech_1.3, San Diego and Boivin, shows that simulation data are aligned to those obtained by experiment. The tested mechanisms are apt to predict the adiabatic flame temperature of a hydrogen/air premixture, throughout the tested ϕ range (0.3 to 1.5). When comparing the maximum adiabatic flame temperature, one observe that almost no difference is noticed. AramcoMech_1.3 generated the highest value, 2401 K, while GRI-MECH 3.0 generated the lowest, 2396 K, representing only a difference of 5 K, which is negligible. The value of ϕ_{max} obtained for all tested kinetic mechanism was 1.06, showing good agreement between all.

Another comparison was made between the kinetic mechanisms to observe the results concerning the species concentration. Results are shown on figure 4.4. When one compare the results for OH radical, its possible to notice that the concentrations are the same for all mechanisms tested, with exception of GRI-MECH 3.0, that has a small deviation, about 1.18×10^{-3}. When one compare the results for H radical, its possible to notice that the concentrations are the same for all mechanisms tested, showing good agreement between them. With all those analysis into account, GRI-MECH 3.0 was chosen to carry out the numerical simulations. The choice is due to the fact that GRI-MECH 3.0 is the kinetic mechanism most tested by the scientific community and because it satisfies all the studies that will be presented in this work.

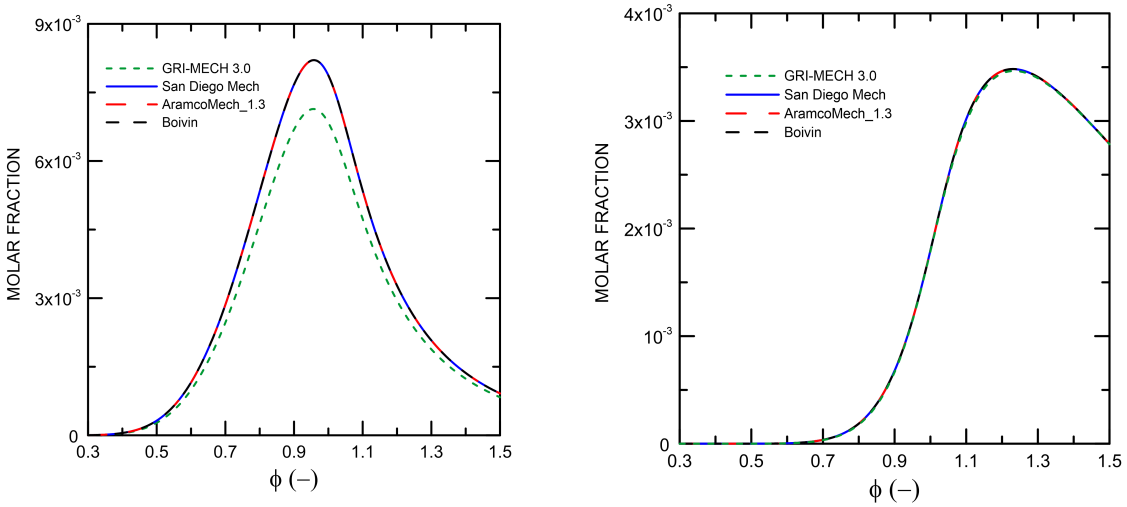

(a) OH radical

(b) H radical

Figure 4.4 Comparison of radicals molar fraction between GRI-MECH 3.0, San Diego Mech, AramcoMech_1.3 and Boivin Mech. Conditions: $H_2/O_2/N_2$ flames at 1 atm and 300 K of unburned gas temperature. **(a)** OH radical. **(b)** H radical.

4.1.3 Pressure

The influence of pressure on the T_b of $H_2/O_2/N_2$ flames was tested. The study was carried out under pressures ranging from 0.5 to 20 atm. The value of ϕ, ranging from 0.5 to 1.5, with a unburned gas temperature of 300 K, using GRI-MECH 3.0. Results are presented in figure 4.5.

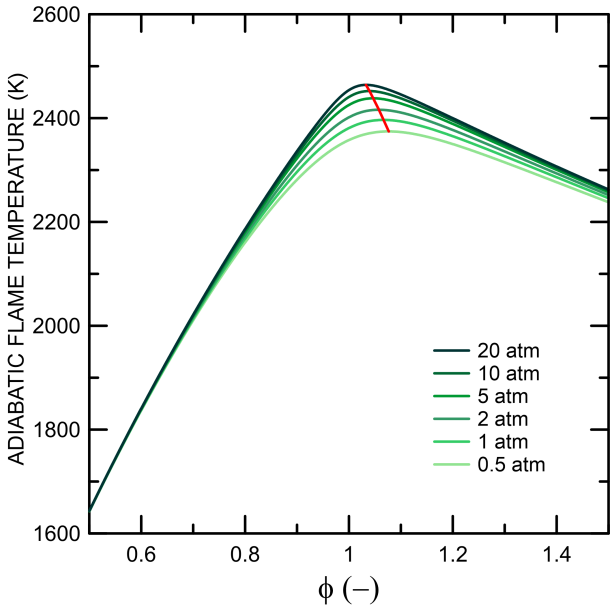

Figure 4.5 GRI-MECH 3.0 mechanism: effect of pressure (0.5 to 20 atm) in the adiabatic flame temperature of $H_2/O_2/N_2$ premixture, at 300 K of unburned gas temperature..

Results obtained for the values of $T_{b.max}$ and ϕ_{max} are presented in table 4.1. The increase of pressure increases the flame temperature. For values of ϕ located in the lean zone, lower than 0.7, the effect of pressure cannot be noticed, so under high oxidized conditions, there is no observed effect . For values of ϕ higher than 0.7 the flame temperature are much affected by pressure. In the rich condition, for values of ϕ above 1.2, is possible to notice that the curves comes near each other and tends to have an adiabatic flame temperature very close.

Table 4.1 GRI-MECH 3.0 mechanism: computed data of $T_{b.max}$ and ϕ_{max}, of $H_2/O_2/N_2$ flames, for pressures of 0.5 to 20 atm, unburned gas temperature of 300 K.

Pressure (atm)	0.5	1	2	5	10	20
$T_{b.max}$ (K)	2374	2396	2416	2438	2452	2464
ϕ_{max} (–)	1.07	1.06	1.05	1.04	1.03	1.03

The values of ϕ_{max} shifts towards the stoichiometric value when the pressure increases. Those results cited were expected, because as the pressure increases, the amount of dissociation decreases, and so less energy is lost to those type of reactions, which makes temperature to rise [130], and if there are less dissociation reactions, ϕ_{max} shifts to stoichiometry.

The effect of pressure in the radicals O, H and OH molar fraction is presented in figure 4.6. Results obtained shows that dissociation reaction really decreases with the increase of pressure, as molar fraction of each of the radicals decreases. Also, the value of ϕ where maximum molar fraction is achieved also decreases with pressure for all the radicals tested.

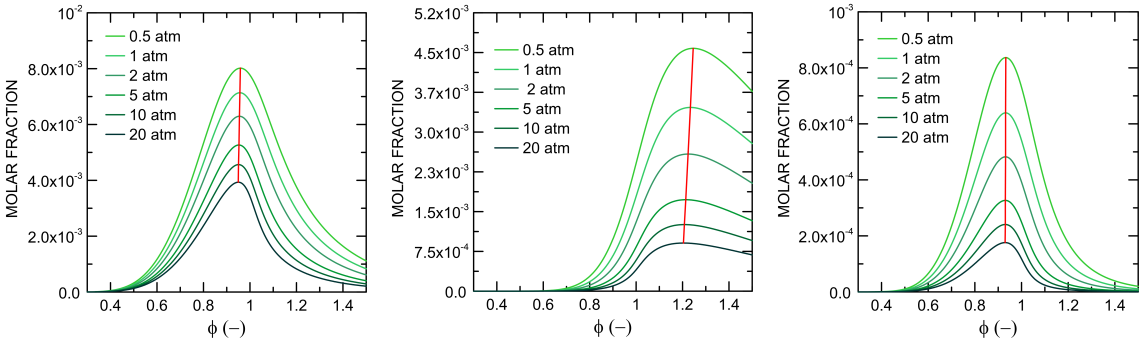

(a) Radical OH **(b)** Radical H **(c)** Radical O

Figure 4.6 GRI-MECH 3.0 mechanism: effect of pressure, from 0.5 to 20 atm in radicals molar fraction of $H_2/O_2/N_2$ premixed flames, at 300 K of unburned gas temperature. **(a)** OH radical. **(b)** H radical. **(c)** O radical.

4.1.4 Unburned gas temperature

In this section, the effect of unburned gas temperature (T_u) on the adiabatic flame temperature will be discussed. The study was done with GRI-MECH 3.0 as the kinetic mechanism, using a premixture of H_2/air, with a range of equivalence ratio between 0.3 and 1.5, at 1 atm and unburned gas temperature with a range between 250 to 500 K.

The results showing the effect of T_u on the adiabatic flame temperature are shown on figure 4.7a and normalized data are shown on figure 4.7b. As happened to pressure, when the unburned gas temperature increases, the adiabatic flame temperature also increases, although its impact occurs not only around stoichiometry, but in the entire range of ϕ tested. The reason for that behaviour rely on the extra amount of energy available due to the pre-heating of mixture, with a more pronounced effect on the lean condition rather than rich. When the equivalence ratio is 0.5, the adiabatic flame temperature is 1642 K,

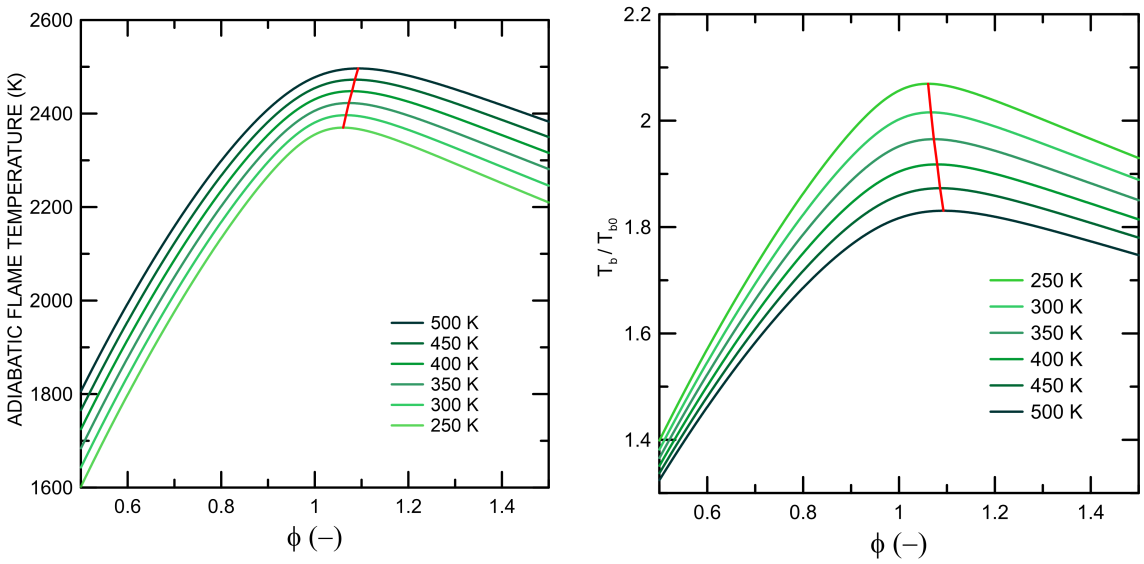

(a) Raw data

(b) Normalized data

Figure 4.7 GRI-MECH 3.0 mechanism: effect of unburned gas temperature (250 to 500 K), in the adiabatic temperature of $H_2/O_2/N_2$ flames at 1 atm. Normalization was performed by dividing flame temperature at any ϕ by the flame temperature at ϕ of 0.3.

for a unburned gas temperature of 300 K, while at 500 K, the value of the adiabatic flame temperature is 1806 K, representing a increase of 163 K. In the rich condition, the difference between the values of flame temperature decreases if compared to lean condition. If the flames temperatures from values of T_u = 300 and 500 K are compared, with ϕ = 1.5, the ΔT_b is 137 K. So, on the rich condition, the adiabatic flame temperature tends to increase less if compared to the lean condition, when the same change is made to the unburned gas temperature. This effect might happen because the molar fraction from the radicals tend to be higher in the rich condition, rather than on lean.

Maximum flame temperatures are observed at values of ϕ between 1.0 and 1.1, increasing along with the increase of T_u, reaching values of 2396 K for T_u of 300 K and 2496 K for T_u of 500 K, which means a increase of 100 K in $T_{b.max}$. On the other hand, as the unburned gas temperature increases, the values of ϕ_{max} also increases, shifting towards rich zone. For T_u of 250 K, maximum equivalence ratio has a value of 1.06, while for an unburned gas temperature of 500 K, ϕ_{max} has a value of 1.08. Table 4.2 summarizes the values of $T_{b.max}$ and ϕ_{max} in function of the unburned gas temperature.

A normalization was performed to analyze if adiabatic flame temperatures changes the same amount for all values of T_u. The normalization was done by dividing the flame temperature at any ϕ by the flame temperature at ϕ of 0.3. It is possible to notice that low values of T_u generates results with higher rate of change in the flame temperature, when

Table 4.2 GRI-MECH 3.0 mechanism: maximum adiabatic flame temperatures and maximum adiabatic temperature equivalence ratio, using a $H_2/O_2/N_2$ premixture, unburned gas temperature in range of 250 to 500 K, at 1 atm.

T_u (K)	250	300	350	400	450	500
$T_{b.max}$ (K)	2370	2396	2422	2448	2472	2496
ϕ_{max} (−)	1.06	1.06	1.07	1.07	1.08	1.08

comparing with higher values of T_u. Because of that, the difference of flame temperature near stoichiometry is lower when compared to values from the lean and rich conditions. This effect might happen because the amount of energy to increase the temperature by one unit (specific heat capacity) increases as the temperature increases. This effect can be observed on figure 4.8, where the results were obtained using algorithm 3.3..

It's noticeable that when the value of ΔT_u is 50 K, the difference observed in the values of ΔT_b won't be the same size, being lower than it. As the temperature rises, more energy is needed to increase the burned gas temperature by one unit, so the change of temperature in T_b is less than the initially expected. This, alongside the radical concentrations can justify why the result obtained is not the expected.

On figure 4.9, it is represented the burned gases molar fraction of the radicals OH, O and H in function of the equivalence ratio. The peaks for the oxygenated radicals occurs on the lean condition, while for the H radical, it occurs with a rich mixture. The molar fraction from all radicals increases alongside with the increase of T_u, which is the opposite to what

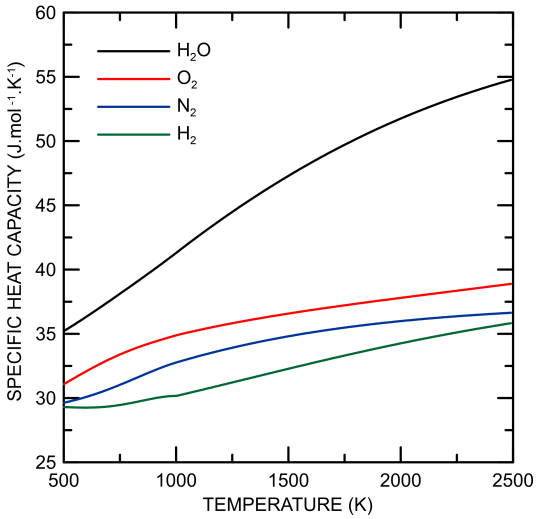

Figure 4.8 GRI-MECH 3.0 mechanism: specific heat capacity of the burned gases of $H_2/O_2/N_2$ flames, $\phi = 1$ and 1 atm.

happens to the increase of pressure. This might happen because the increment on the unburned gas temperature gives more energy to the occurrence of dissociation reactions.

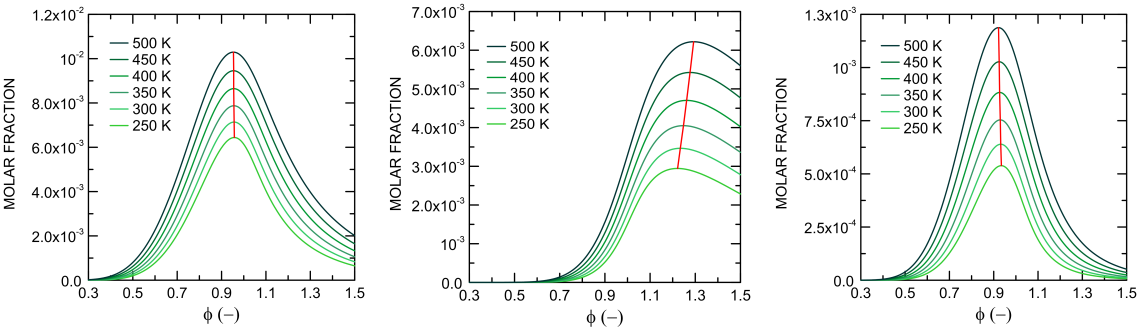

(a) Radical OH **(b)** Radical H **(c)** Radical O

Figure 4.9 GRI-MECH 3.0 mechanism: effect of unburned gas temperature, ranging from 250 to 500 K, on $H_2/O_2/N_2$ premixture at 1 atm, on the burned gas concentration of: **(a)** OH radical. **(b)** O radical. **(c)** H radical.

4.1.5 Aggregate effect of pressure and unburned gas temperature

In this section, the influence of pressure and unburned gas temperature in flame parameters will discussed. The results were computed using GRI-MECH 3.0, for a H_2/air premixture. The first analysis was based on the influence of pressure (ranging from 0.5 to 60 atm) in $T_{b.max}$ and ϕ_{max}, the second analysis on the combined effect of the unburned gas temperature (ranging from 250 to 500 K) and pressure (ranging from 0.5 to 20 atm) on the parameters cited before, and the final study is about the rate of change in the flame temperature in function of T_u (ranging from 250 to 500 K) and P (ranging from 0.5 to 20 atm) on the lean and rich conditions.

4.1.5.1 Influence of pressure on ϕ_{max}

First, an analysis of the maximum adiabatic flame temperature and ϕ_{max} in function of pressure was done, using H_2/air premixture, with a unburned gas temperature of 300 K, and GRI-MECH 3.0 as the kinetic mechanism. Results are shown on figure 4.10.

Pressure causes inverse effect on those parameters. For the maximum adiabatic flame temperature, there is an increase alongside the pressure, with a logarithmic growth. On the other hand, the values of ϕ_{max} decreases as pressure increases.

When working with low pressures, it is possible to observe a drastic change on both $T_{b.max}$ and ϕ_{max}, until a pressure of 10 atm. After that, for pressures between 10 and 40 atm, its possible to notice a moderated change on those parameters. For pressures

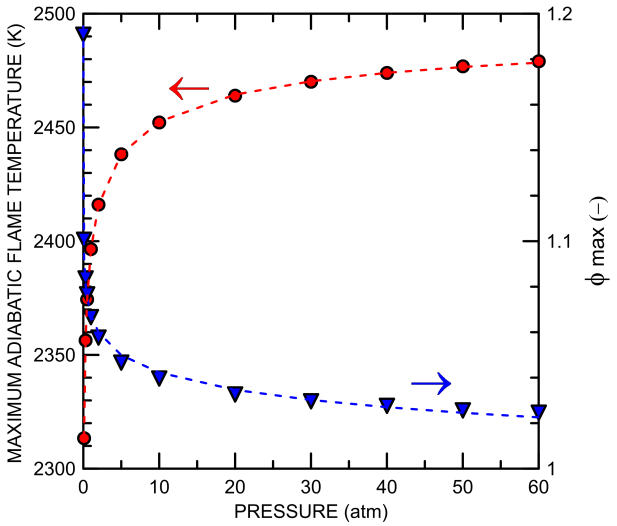

Figure 4.10 GRI-MECH 3.0 mechanism: effect of pressure (up to 60 atm) on $T_{b.max}$ and ϕ_{max}, with an unburned gas temperature of 300 K, using a $H_2/O_2/N_2$ premixture. (●) $T_{b.max}$, (▼) ϕ_{max}, (- - -) fitting by equation (24) and (- - -) fitting by equation (25).

higher than 40 atm, an increase in the value of $T_{b.max}$ is barely noticeable. It also happens with ϕ_{max}, as the values of ϕ_{max} tends to change very little, with near constant rate of change. The maximum flame temperature can be expressed as a function of pressure by the empirical equation (24), which has an average deviation of 0.27 K between GRI-MECH 3.0 and the proposed equation. The pressure input in the equation is in atm.

$$T_{b.max} = 2396.14 + 2.45\ (\ln P)^2 + 30.14\ \ln P \tag{24}$$

The effect of pressure on maximum equivalence ratio can be described by equation (25), which has an average deviation of 0.002 ϕ unit between GRI-MECH 3.0 and the proposed equation. The pressure input in the equation is in atm.

$$\phi_{max} = 1.0676 - 0.0110\ \ln P \tag{25}$$

4.1.5.2 Combined effect of unburned gas temperature and pressure

As shown in section 4.1.4, unburned gas temperature also has an effect on the values of ϕ_{max} and $T_{b.max}$. Results were obtained using GRI-MECH 3.0 as the kinetic mechanism. The combined results obtained using H_2/air premixture, with unburned gas temperature varying from 250 to 500 K and pressure from 0.5 to 20 atm is discussed here. Results are shown on figure 4.11.

Higher values of maximum flame temperatures are observed for high values of unburned temperature and pressure. It can be said that T_b is directly proportional to P and

T_u. Higher values of ϕ_{max} are also observed for high unburned gas temperatures, but decreases with pressure. A maximum value of 2592 K was observed at 20 atm and unburned gas temperature of 500 K. Maximum value of ϕ_{max} is 1.1, and its observed near vacuum and unburned gas temperature of 500 K. When operating at high pressures and temperatures, higher values of flame temperatures are achieved, with ϕ_{max} near stoichiometric value, implying that less fuel is used.

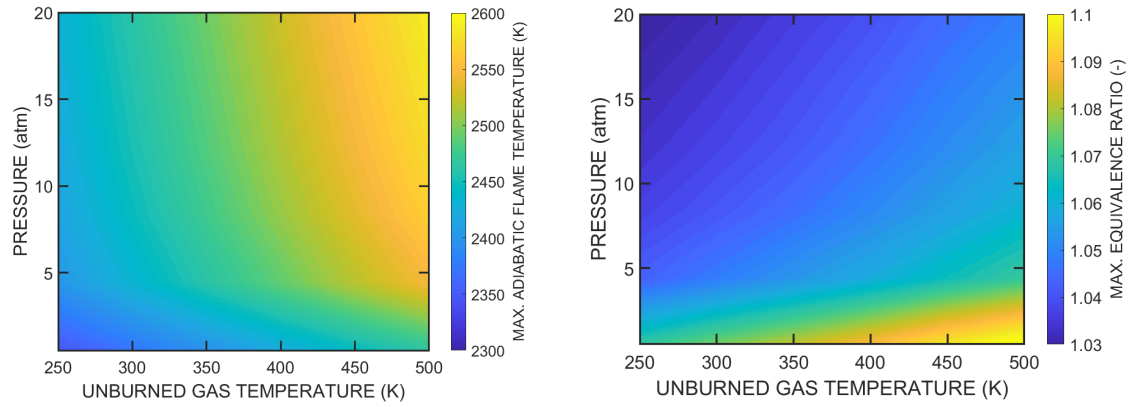

(a) $T_{b.max}$ **(b)** ϕ_{max}

Figure 4.11 GRI-MECH 3.0 mechanism: effect of unburned gas temperature and pressure on the maximum adiabatic flame temperature, using a $H_2/O_2/N_2$ premixture. **(a)** Maximum flame temperature, **(b)** Equivalence ratio of maximum adiabatic flame temperature.

4.1.5.3 Influence on the temperature rate of change

Adiabatic flame temperature changes with equivalence ratio, unburned gas temperature and pressure. A topic analyzed was the rate of change of T_b as a function of ϕ and its behaviour with other flame parameters, such as unburned gas temperature and pressure.

The rate of change on premixed H_2/air flames were separately analyzed in two regions: lean and rich. Results are shown in figure 4.12. The rate of change is calculated by dividing the change of temperature by the corresponding change on ϕ.

The rate of change has roughly constant value for ϕ between 0.3 and 0.75 in the lean regions and between 1.2 and 1.5 in the rich region. Higher rate of change can be achieved for lower unburned gas temperatures and higher pressures.

On lean condition, the rate of change starts from 1912 K/ϕ unit at 0.5 atm and T_u of 500 K, and have a maximum rate of change of 2041 K/ϕ unit at 20 atm and unburned gas temperature of 250 K. On rich condition, which has a negative rate of change, the values

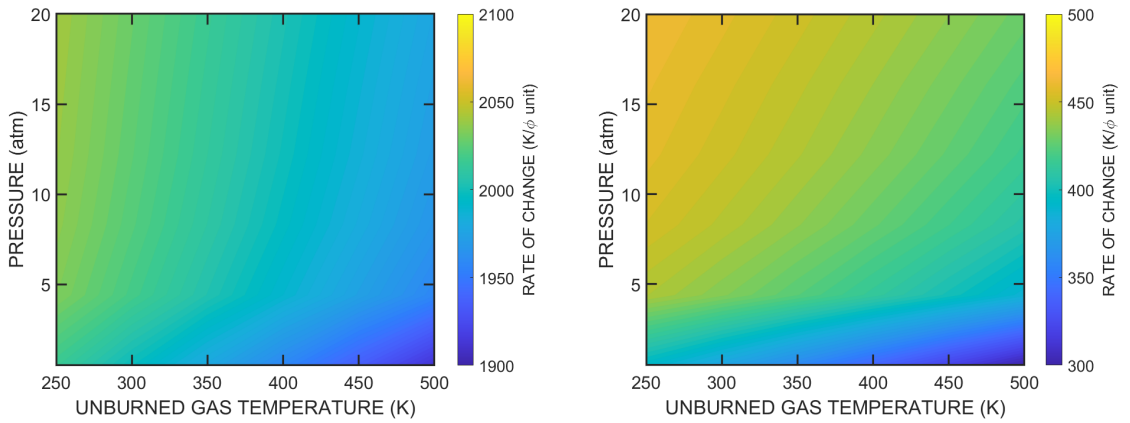

(a) Lean condition

(b) Rich condition

Figure 4.12 GRI-MECH 3.0 mechanism: effect of T_u and pressure on the rate of change in the lean ($0.3 < \phi < 0.75$) and rich ($1.2 < \phi$ 1.5) for a H_2/air premixture. **(a)** Rate of change on lean condition, **(b)** rate of change on rich condition.

starts from 300 K/ϕ unit for 0.5 atm and T_u of 500 K, and have a maximum rate of change of 463 K for 20 atm and T_u of 250 K.

Higher rates of change can be achieved at 300 K and with a increase on pressure. The rates of change on lean condition are really higher if compared to the rich one, about 4 times greater. This might be explained by the fact that the energy lost to heat O_2 in lean condition has more effect on the adiabatic flame temperature than the decrease of energy released due to incomplete combustion on the rich condition.

4.1.6 Methane flames

Methane is one of the most used energy carrier, being the main constituent in the natural gas and biogas. A series of studies concerning the combustion of a premixture composed by $CH_4/O_2/N_2$ were performed, using GRI-MECH 3.0 as the kinetic mechanism. First, the behaviour of the adiabatic flame temperature is shown and a comparison with $H_2/O_2/N_2$ flames is made. The effect of the unburned gas temperature, from 250 to 500 K, and pressure, from 0.5 to 20 atm is also shown in this section. An analysis about the influence of those parameters in the most important radicals and molecular species is also discussed. Data comparing the H_2/air and CH_4/air flames, with an unburned gas temperature of 300 K at 1 atm are shown on figure 4.13.

Hydrogen flames achieves higher temperatures than methane flames in the entire range of ϕ studied. While hydrogen flame has a $T_{b.max}$ of 2396 K, methane flames achieves a maximum temperature of 2234 K, representing a difference of 162 K. This result might

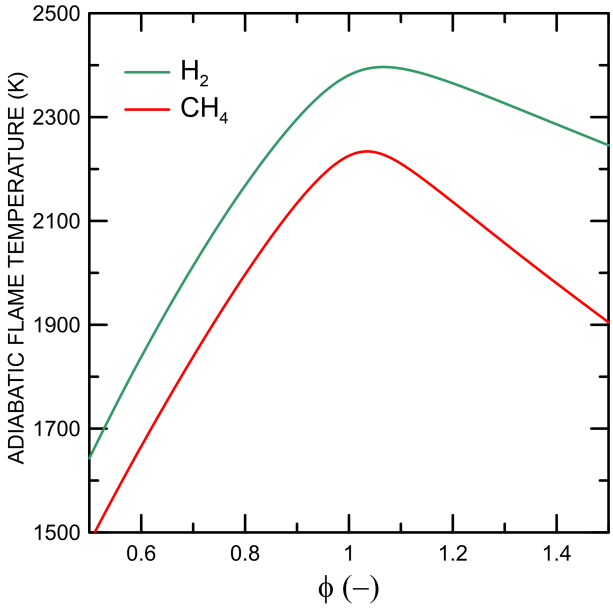

Figure 4.13 GRI-MECH 3.0 mechanism: comparison between the adiabatic flame temperatures of CH_4/air and H_2/air premixtures, at 1 atm and premixture temperature of 300 K.

be justified by the fact that methane combustion generates CO_2 as a product. This species doesn't react, so the presence of it tends to lower the adiabatic flame temperature due to heat loss to it. Another factor that may account for this is that the thermal conductivity of H_2 is much higher than that of CH_4 (186.6 for H_2 [136] versus 34.4 $mW\,m^{-1}\,K^{-1}$ for methane [137], both at 300 K). For hydrogen flames, maximum equivalence ratio is 1.06, while for methane flame this value is lower, that being 1.03, so it is closer to stoichiometry.

Methane flames are also affected by pressure and unburned gas temperature, and their behaviour is similar to H_2 flames. Results are shown on figure 4.14.

Higher pressure generates differences between adiabatic flame temperatures, only on zones of equivalence ratio near stoichiometry. Also, when ϕ is lower than 0.8 and higher than 1.2, the values of temperature for all the pressures are the same. On the zone of equivalence ratio between 0.8 and 1.2, the curves get further away from each other, achieving the highest value of $T_{b.max}$ of 2282 K at 20 atm and the lower value of $T_{b.max}$ of 2218 K at 0.5 atm, representing a difference of 64 K. As happened to H_2, the values of ϕ_{max} decreases with pressure and increases with T_u. Data of $T_{b.max}$ and ϕ_{max} for all tested pressures are presented on table 4.3.

Results obtained when changing unburned gas temperature at 1 atm also agrees with those obtained for H_2, where a difference on T_b from each T_u happens for the entire ϕ range, due to increase on unburned mixture temperature. For the value of T_u of 300 K, at 1 atm, the maximum adiabatic flame temperature achieved is 2233 K, and 2331 K when

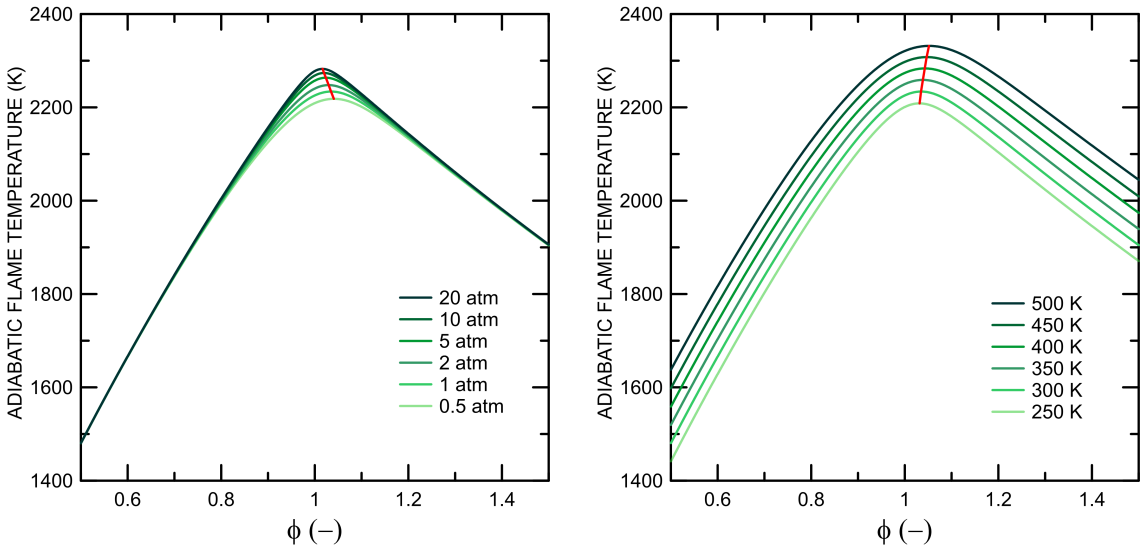

(a) Pressure

(b) Unburned gas temperature

Figure 4.14 GRI-MECH 3.0 mechanism: effect of pressure and unburned gas temperature on the adiabatic flame temperature for $CH_4/O_2/N_2$ premixed flames. **(a)** Effect of pressure, **(b)** effect of unburned gas temperature.

the unburned gas temperature is 500 K, representing a difference of 98 K, showing that a ΔT of 200 K in the unburned gas temperature does not reflect the same increase on the adiabatic flame temperature. The value obtained is lower than the obtained by H_2, that is 100 K, but with just a little difference. For the values of ϕ_{max}, it is possible to notice that it increases along with the unburned gas temperature, starting from 1.03 for T_u of 250 K and reaching 1.05 with an unburned gas temperature of 500 K, which are inline with the results obtained with H_2 flames.

Like in H_2 flames, the concentration of H, O and OH decreases with the increase of pressure. Results are shown on figure 4.15.

Among all radicals, OH has the highest molar fraction in the burned gases, showing that a lot of side reactions occurs with this radical. Atomic hydrogen molar fraction increases when equivalence ratio is higher than 0.8. Under leaner conditions, molecular

Table 4.3 GRI-MECH 3.0 mechanism: computed data of $T_{b.max}$ and ϕ_{max}, of $CH_4/O_2/N_2$ flames, for pressures of 0.5 to 20 atm, unburned gas temperature of 300 K.

Pressure (atm)	0.5	1	2	5	10	20
$T_{b.max}$ (K)	2218	2234	2248	2264	2274	2282
ϕ_{max} (–)	1.04	1.03	1.03	1.03	1.02	1.02

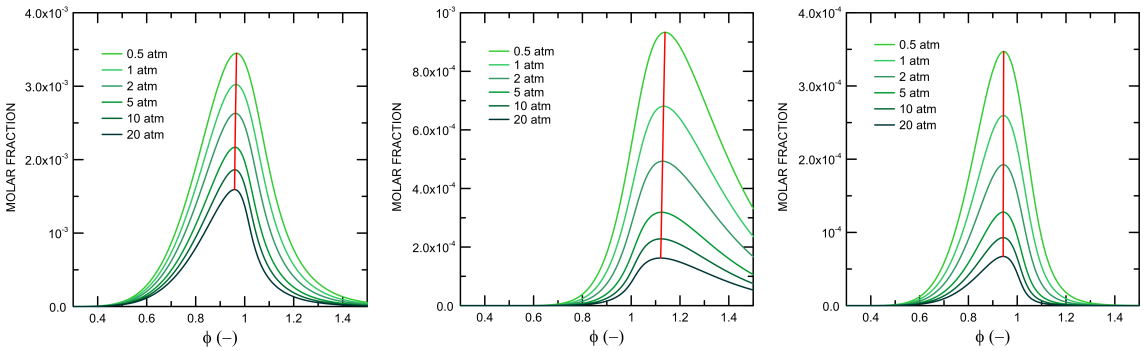

(a) Radical OH **(b)** Radical H **(c)** Radical O

Figure 4.15 GRI-MECH 3.0 mechanism: effect of pressure on radicals molar fraction for a $CH_4/O_2/N_2$ premixture, at 300 K of unburned gas temperature. **(a)** OH radical. **(b)** H radical. **(c)** O radical.

hydrogen molar fraction tends to be insensitive to pressure change. Maximum H radical fraction is achieved in rich condition, with an equivalence ratio of 1.14 at 0.5 atm and 1.12 at 20 atm, showing that the maximum value of molar fraction shifts towards stoichiometry when pressure increases. Atomic oxygen fraction has a peak in lean condition, when the equivalence ratio is 0.94, with that value being the same for all the pressures. For OH radical, the concentration peak is achieved in lean condition as well, with the peaks occurring when ϕ is 0.97 at 0.5 atm and 0.96 at 20 atm, so pressure doesn't affect so much. This analysis is relevant to figure out why pressure induces significantly changes in flame temperature in zones near stoichiometry, as shown for hydrogen as well on section 4.1.3. Oxygenated species have their maximum at lean conditions, while non-oxygenated species have their peak at rich conditions, following a trend that happened to H_2/air flames. The main products from hydrocarbon combustion, that being CO_2 and CO, were also studied. Those results can be seen on figure 4.16.

As for the main products from CH_4 combustion, carbon dioxide content in the burned gas increases toward stoichiometry. When working with lean condition, the excess of oxygen ensures that the reaction between CO and O_2 occurs to form CO_2 and that is why its fraction on the product is higher if compared to the carbon monoxide. The fact that its concentration increases all the way to its peak on the lean condition is due to the reduction of the concentration of oxygen as the equivalence increases. The peak is observed very close to stoichiometry starting at a value of 0.96 for 0.5 atm and 0.99 when pressure increase to 20 atm. After its peak, CO_2 molar fraction starts to decrease and as it does, CO molar fraction starts to increase, because in rich condition there is a excess of fuel. Because of that, there is not enough O_2 to react with CO and incomplete combustion takes place

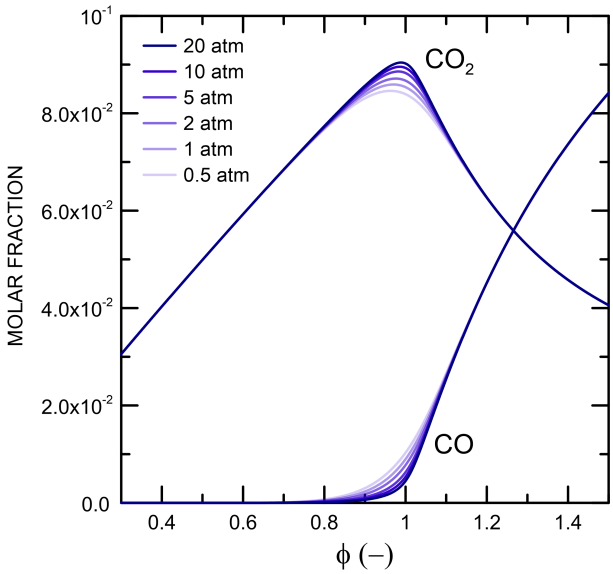

Figure 4.16 GRI-MECH 3.0 mechanism: effect of pressure on the burned gas concentration of CO_2 and CO for a $CH_4/O_2/N_2$ premixed flame and unburned gas temperature of 300 K.

over complete combustion. For carbon monoxide, as pressure increases, the concentration decreases, the opposite to what happens to CO_2. Pressure only affects the concentration of those products near stoichiometry, which is similar to what happened with the adiabatic flame temperature. This might happen because near stoichiometry there is less dissociation reactions as pressure increases, and because of that the concentration near that zone is different as pressure changes. The effect of T_u on OH, H and O radicals concentration produced by CH_4/air combustion is the same observed for the H_2/air. The results are shown on figure 4.17.

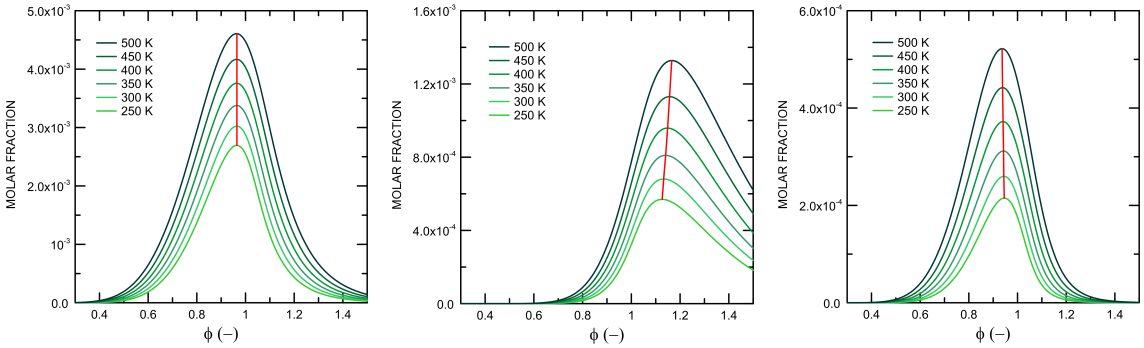

(a) Radical OH **(b)** Radical H **(c)** Radical O

Figure 4.17 GRI-MECH 3.0 mechanism: effect of unburned gas temperature on radicals fraction in burned gases for a $CH_4/O_2/N_2$ premixture, at 1 atm. **(a)** OH radical. **(b)** H radical. **(c)** O radical.

The effect observed is the opposite to what happened to the pressure, where all radicals concentration increases as the unburned gas temperature increases. Again, OH has the highest molar fraction in the burned gases. The equivalence ratio where the concentration reaches its peak has a value of 0.96 for all the tested values of T_u.

Under leaner conditions, molar fraction of atomic hydrogen tends to be insensitive to a change on the unburned gas temperature as well. Maximum H radical fraction is achieved in rich condition, with an equivalence ratio of 1.13 at 250 K and 1.17 at 500 K, showing that an increase on T_u shifts the maximum molar fraction to a rich condition, which is the opposite to what happened to a change on the pressure.

Atomic oxygen concentration has a peak in lean condition, so this follows the trend that oxygenated species have their peak on lean conditions. The peak is observed when the equivalence ratio is 0.94, with that value being the same for all the T_u tested.

The results concerning the effect of T_u on the molar fraction of CO_2 and CO can be seen on figure 4.18. The results obtained are similar to what happens to the pressure, where the peak of CO_2 is observed on lean conditions and the growth of CO also starts in the same conditions. The difference observed is that the increase on T_u causes a decrease in the concentration of CO_2 and a brief increase on the carbon monoxide concentration, which is the opposite to what happens with the pressure increase. The peak on CO_2 molar fraction occurs when the equivalence ratio is about 0.96 and the maximum molar fraction obtained is 0.087 for a unburned gas temperature of 250 K.

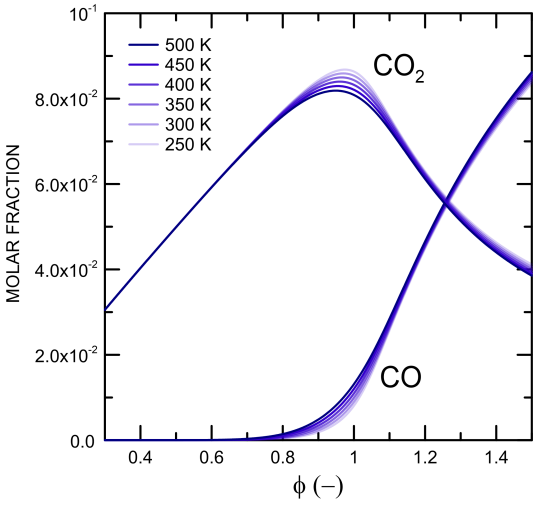

Figure 4.18 GRI-MECH 3.0 mechanism: effect of unburned gas temperature on the concentration of CO_2 and CO in the burned gases. for a $CH_4/O_2/N_2$ flame at 1 atm.

4.1.7 $CH_4/H_2/CO_2$ fuel blends

A study was carried out by blending H_2 with a biogas with no fixed composition of CH_4 and CO_2, despite the normal composition of biogas being tipically 50 to 75 % of

methane and 25 to 50 % of CO_2 [138]. Results are shown in figure 4.19, where each vertex represents one component of the fuel blend and the edges shows the composition of each one on the mixture. It is possible to see that the lowest flame temperatures are attained on lean condition, for the equivalence ratio of 0.7, where is possible to see that as the mixture gets rich on CO_2, flame temperature starts to decrease, which can be seen as the blue color. This makes sense, because carbon dioxide doesn't combust, so no heat is released. Also, the presence of it steals the heat generated by the combustion of the other two compounds.

When the equivalence ratio is located at rich condition, as showed on with the equivalence ratio of 1.3, flame temperature is higher than the one in lean. The upper zone, where it gets near CO_2 vertex, is similar to the one showed in the lean zone. As happened before, the highest temperature is achieved as the composition gets rich in H_2 and the middle zone is hotter than the one observed for ϕ of 0.7. So, for the same distance from stoichiometry, flames from a blend of hydrogen with biogas at any composition achieves higher temperatures than flames on lean condition. For example, a flame with a fixed composition of CO_2 below 20 % with any percentage of H_2 and CH_4, is 100 to 200 K hotter on rich condition than on lean.

Hotter flames temperatures are achieved when the equivalence ratio is equal to the stoichiometric value. As it is possible to see, the region with low values of T_b (near CO_2 vertex) is smaller if compared to the other 2 cases presented before. Also, on the middle region observed in the triangular diagram, is possible to notice that higher temperatures are reached, indicating that a mixture rich in CO_2 can be used to achieve high temperatures. For example, a mixture that has a composition of 20/40/40 of $CO_2/CH_4/H_2$ has an ndiabatic flame temperature of 2184 K when equivalence ratio is as stoichiometry value, 1823 K when ϕ is 0.7 and 2014 K when equivalence ratio is 1.3, showing a difference of 361 K between the highest and lowest temperature showed.

As said before, the highest flame temperatures were achieved when the equivalence ratio is located at stoichiometric value, so that value has been chosen to see the influence of pressure and temperature on the mixture of H_2/biogas. The ternary diagrams values of T_u increases on the horizontal axis while pressure increases on the vertical axis. As it is possible to see on figure 4.20, lowest flame temperatures are achieved at ambient temperature and pressure. As the unburned gas temperature increases, it is possible to see that overall flame temperature also increases. A noticeable change can be observed in the middle region of the diagrams, where is possible to get higher flame temperatures for T_u of 500 K even for greater CO_2 concentrations. A mixture that has a composition of 20/40/40 of $CO_2/CH_4/H_2$ has

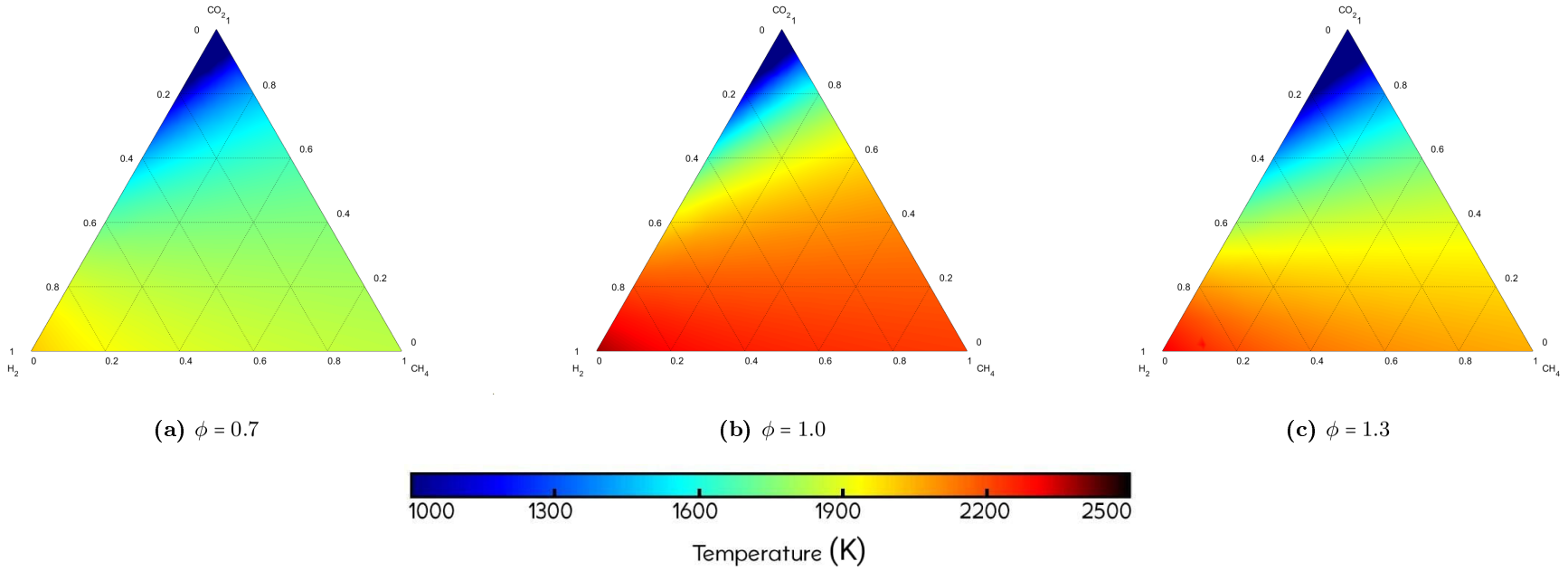

(a) $\phi = 0.7$ **(b)** $\phi = 1.0$ **(c)** $\phi = 1.3$

Figure 4.19 Adiabatic flame temperatures distribution of air premixed ternary fuel mixtures of $H_2/CH_4/CO_2$, at 1 atm and $T_u = 300\,\mathrm{K}$, under three equivalence ratio conditions: (a) lean, (b) stoichiometric, and (c) rich. Data computed using GRI-Mech 3.0.

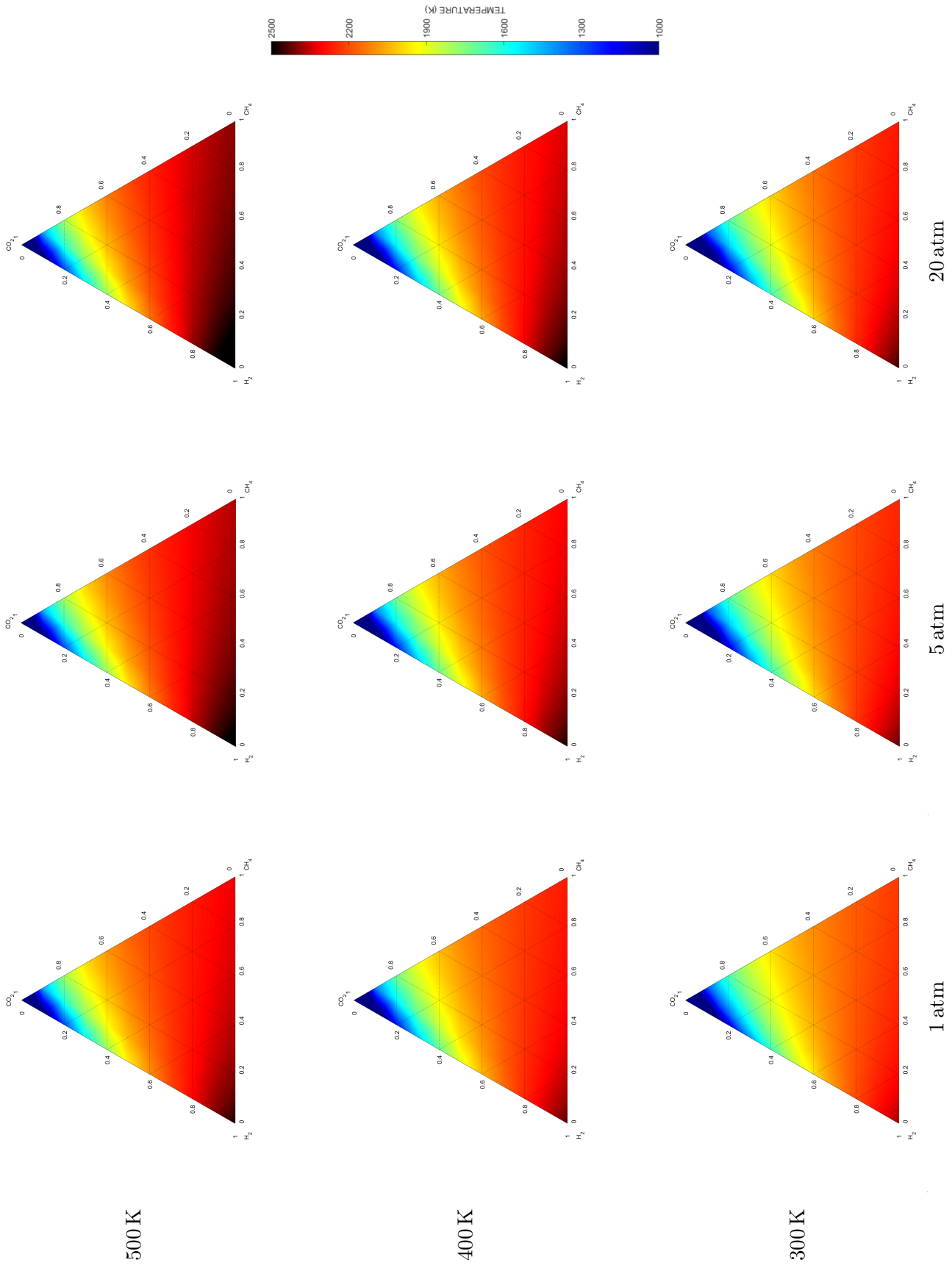

Figure 4.20 Adiabatic flame temperature of $H_2/CH_4/CO_2$ fuel blends premixed with air at stoichiometric equivalence ratio. Effect of pressure and unburned gases temperature.

a adiabatic flame temperature of 2184 K for a unburned gas temperature of 300 K, 2234 K when T_u is at 400 K and 2283 K if the unburned gas temperature is 500 K, showing a increase of 99 K between the highest and lowest temperature showed.

Analysis of the impact of pressure reveals that flame temperature also rises as pressure rises. Using the same fuel composition said before, that being 20/40/40 of $CO_2/CH_4/H_2$, the data obtained at ambient temperature (300 K) shows a adiabatic flame temperature of 2184 K for a pressure of 1 atm, 2212 K for a pressure of 5 atm and 2231 K when pressure has a value of 20 atm, showing a difference of 47 K between the highest and lower pressure tested, meaning a increment of 2.35 $K\,atm^{-1}$. Highest flame temperatures are achieved with a unburned gas temperature of 500 K and pressure of 20 atm.

A brief summary about this section so far is shown on table 4.4.

Table 4.4 Summary of results from section 4.1.

Parameter	Effect	$T_{b.max}$,ϕ_{max}
ϕ (–) [0.3 *to* 1.5]	• ↑ flame temperature through lean condition; • Peak located at rich condition; • ↓ flame temperature after the peak; • Oxigenated species have their peak at lean condition, while non-oxigenated have their peak at rich condition; • Rate of change higher on lean contiion.	• Located at rich combustion condition.
P (atm) [0.3 *to* 20]	• ↑ on pressure = ↑ flame temperature for $0.7 \leq \phi \leq 1.2$; • No difference on flame temperature for $\phi \leq 0.7$ and $\phi \geq 1.2$; • Radicals concentration decrease as pressure increases (less dissociation reactions).	• ↑ of P = ↑ of $T_{b.max}$; • ↑ of P = shift to stoichiometry.
T_u (K) [250 *to* 500]	• ↑ on unburned gas temperature = ↑ flame temperature for all values of ϕ; • An increase of 50 K on T_u doesn't reflect the same increase on T_b, but lower than that; • Radicals concentration increases alongside T_u. More energy to start dissociation reactions.	• ↑of T_u = ↑ of $T_{b.max}$; • ↑ of T_u = shift to rich zone.
Fuel composition [H_2, CH_4, CO_2]	• $H_2/O_2/N_2$ flames are hotter than $CH_4/O_2/N_2$ flames (162 K at peak); • Less number of dissociation reactions and no presence of CO and CO_2 on $H_2/O_2/N_2$ flames; • The addition of CO_2 decreases flame temperature, but can be used in the fuel mixture.	• H_2 values of $T_{b.max}$ are higher than CH_4. • H_2 values of ϕ_{max} are higher than CH_4.

4.1.8 Empirical equations

The empirical method used to predict the adiabatic flame temperature based on detailed kinetic combustion mechanism can be complicated in some ways. A lot of computational effort has to be done to estimate it and also a lot of coefficients (namely the NASA polynomials) are used. With the empirical data obtained for $H_2/O_2/N_2$ flames, using curve fitting technique, empirical equations to compute adiabatic flame temperature are proposed in this section, with the objective to make flame temperature calculation with less effort and accurate results. The development of the equation was done through two approaches. The first one was performed using polynomial equations, while increasing the number of terms, observing and comparing with the results generated by GRI-MECH 3.0. The second approach was done with a more complex equation that comprises the variation of ϕ, T_u and pressure. The conditions tested were for an equivalence ratio between 0.3 and 1.5, T_u from 250 to 500 K and pressure in range of 0.5 to 20 atm, using a premixture of $H_2/O_2/N_2$.

4.1.8.1 Empirical equations approach

A polynomial equation type was tested to predict the adiabatic flame temperature of $H_2/O_2/N_2$ mixture at 300 K and 1 atm in dependence on equivalence ratio. The empirical equation approach could be made by dividing the results in 3 separated zones, that being $\phi \leq 0.7$, $0.7 \leq \phi \leq 1.2$ and $1.2 \leq \phi$, but in this work the aim was to describe the adiabatic flame temperature with just one equation, ranging all ϕ values tested. It started with a simple four coefficients and ends with a seven coefficients equation, with an analysis on how the number of coefficients affect the prediction accuracy, comparing the analytical results with the ones obtained using GRI-MECH 3.0. Polynomial relations proposed are equations (26) to (29), starting with the one with 4 coefficients to the one with 7.

$$T_b = a_0 + b_0\phi^{2.5} + c_0e^{\phi} + d_0ln\phi \tag{26}$$

$$T_b = a_0 + b_0\phi + c_0\phi^{2.5} + d_0e^{\phi} + e_0\ln\phi \tag{27}$$

$$T_b = a_0 + b_0\phi + c_0\phi^2 + d_0\phi^3 + e_0\phi^4 + f_0\phi^5 \tag{28}$$

$$T_b = a_0 + b_0\phi + c_0\phi^2 + d_0\phi^3 + e_0\phi^4 + f_0\phi^5 + g_0\phi^6 \tag{29}$$

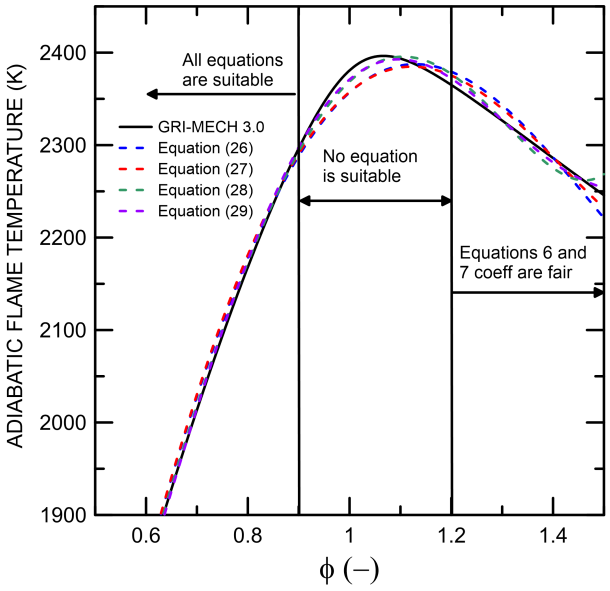

Figure 4.21 Comparison of adiabatic flame temperature at 300 K and 1 atm generated by GRI-MECH 3.0 and polynomials equation (26) to (29). (—) GRI-MECH 3.0, (- -) equation (26), (- -) equation (27), (- -) equation (28), (- -) equation (29).

The values for all coefficients, mean deviation (K), and the difference from the values of ϕ_{max} obtained by GRI-MECH 3.0 and from the empirical equations are shown on table 4.5.

A graphical comparison of polynomials predictions with kinetic calculations are shown on figure 4.21. On lean condition, below $\phi \leq 0.9$, analytic predictions by equations (26) to (29) are satisfactory. On rich condition, above $\phi = 1.2$, the results obtained also agrees, with a better fitting with the seven coefficient equation. On the region near stoichiometry, with ϕ between 0.9 and 1.2, its possible to see that all of the 4 proposed equations have a big deviation from the values obtained by GRI-MECH 3.0. The most important one is the shift of the value of ϕ_{max} to rich zone, although the value of maximum adiabatic flame temperatures being almost the same from GRI-MECH 3.0, and the best fitting equation being the one with most polynomials. The results shows that a increase on the number of polynomials also generates better results, with a minimization of the deviation from results obtained by the empirical and GRI-MECH 3.0, while also decreasing the difference on ϕ_{max} between those.

Table 4.5 Coefficients a_0 to g_0 of equations (26) to (29), related errors (K) and values of $\Delta\phi_{max}$, for a premixed $H_2/O_2/N_2$ flame at 1 atm and unburned gas temperature of 300 K.

Eq.	a_0	b_0	c_0	d_0	e_0	f_0	g_0	Deviation (K)	$\Delta\phi_{max}$
(26)	−6953.79	−5208.24	5341.235	−1012.87	–	–	–	11.8	0.06
(27)	−8242.81	−621.185	−5981.71	6328.682	−1166.28	–	–	11.5	0.05
(28)	69.339 19	5775.215	−10 369.1	14 918.5	−10 847.6	2822.443	–	4.3	0.04
(29)	−1095.4	15 867.64	−44 584.3	73 272.93	−63 956.4	27 421.9	−4555.46	4.5	0.03

Maximum value of adiabatic flame temperature obtained by GRI-MECH 3.0 is 2396 K, while for empirical equations (26) to (29), the values obtained are 2387, 2384, 2395 and 2392 K, which indicates that the predictions of the adiabatic flame temperature is close to the one obtained using GRI-MECH 3.0. The big discrepancy is observed when analyzing values of ϕ_{max}. The value of ϕ_{max} obtained by GRI-MECH 3.0 is 1.06, while the ones from empirical equations (26)-(29)the values obtained are 1.13, 1.12, 1.10 and 1.09 respectively. This shows that equation (29) generates better results to represent the combustion of $H_2/O_2/N_2$ premixture, at the temperature and pressures said before.

4.1.8.2 Comprehensive equation

The set of polynomial equations presented in the previous section had a limitation of being valid for 1 atm and 300 K of unburned gas temperature. A new empirical equation type was developed to include a range of pressure and unburned gas temperature. It was tested a rational relation approach of 19 coefficients, represented by equation (30). It is optimized for $H_2/O_2/N_2$ flames, unburned gas temperature in range of 250 to 500 K, pressure in range of 0.5 to 20 atm and ϕ between 0.3 and 1.5.

$$T_b = \left(\frac{a_0 + b_0\phi^2 + c_0\phi^4 + d_0\phi^6}{1 + e_0\phi^2 + f_0\phi^4 + g_0\phi^6} \right) + [\alpha(T_u - 300)] \tag{30}$$

In equation (30), α is a variable that correct the change of T_b when T_u varies. Coefficients a_0 to g_0 are dependent on the pressure, and can be written as:

$$a_0^2 = a_1 + a_2 \ln P$$

$$b_0 = b_1 + b_2 \ln P + b_3/P$$

$$c_0 = (c_1 + c_3 \ln P)/(1 + c_2 \ln P)$$

$$d_0^2 = d_1 + d_2 \ln P$$

$$e_0^{-1} = e_1 + e_2 \ln P + e_3/P^{0.5}$$

$$f_0^{-1} = f_1 + f_2(\ln P)^2 + f_3/P^{0.5}$$

$$g_0 = (g_1 + g_3 P^{0.5})/(1 + g_2 P^{0.5})$$

Coefficients of equation (30) for $H_2/O_2/N_2$ flames are found on table 4.6. Those coefficients were calculated using a curve fitting technique, where a solver was used to

Table 4.6 Coefficients a_n to g_n ($n = 1$ to 3) of equation (30), for a premixed $H_2/O_2/N_2$ flame. Values were tested for ϕ from 0.3 to 1.5, T_u from 250 to 500 K and pressure from 0.5 to 20 atm.

n	a_n	b_n	c_n	d_n	e_n	f_n	g_n
1	477 813.9	9761.543	−10 843.8	49 761 441.00	0.333 394	−0.165 57	2.857 595
2	−10 229.1	115.1237	0.143 141	5 693 916.00	−0.003 32	0.000 429	0.463 496
3	-	76.043 34	−3141.23	–	−0.024 61	−0.051 92	1.821 571

minimize the sum fo the error between values from GRI-MECH 3.0 and equation (30). For a $H_2/O_2/N_2$ flame, the value of α is 0.6.

A comparison from the results obtained by GRI-MECH 3.0, equations (29) and (30) was performed, with an T_u of 300 K, at 1 atm and equivalence ratio in range of 0.5 to 1.5 and the results can be seen on figure 4.22.

The results obtained by equation (30) fits adequately the kinetic data from GRI-MECH 3.0, with a mean temperature deviation of 1.5 K and maximum deviation of 7.2 K. The ϕ_{max} predicted by equation (30) is almost the same from GRI-MECH 3.0, with the former one having a value of 1.08 and the latter one 1.07. That is an improvement if compared to the ϕ_{max} obtained from equation (30). The maximum adiabatic flame temperature obtained by equation (30) was also a improvement, with a value of 2393 K obtained, a small difference from the 2396 K obtained by GRI-MECH 3.0, which isn't a significant deviation.

A second analysis has been performed about the influence of unburned gas temperature, at 1 atm, on the adiabatic flame temperature of $H_2/O_2/N_2$ flames as predicted by equation (30). The results can be seen on figure 4.23. For lower values of unburned gas temperature ($T_u \leq 400$), equation (30) fits well the kinetic data, on the lean and rich con-

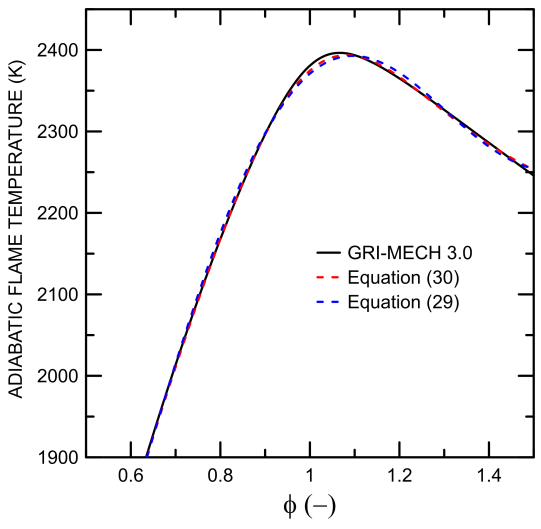

Figure 4.22 Predictions of adiabatic flame temperature of $H_2/O_2/N_2$ flames, with the unburned gas temperature of 300 K, and 1 atm. (—) GRI-MECH 3.0, (- -) equation (29), (- -) equation (30).

dition, even near stoichiometry. The ϕ_{max} generated by equation (30) are 1.08 for all the unburned gas temperatures tested, while the results generated by the kinetic mechanism are 1.07, 1.08 and 1.09 for the values of T_u of 300, 400 and 500 K. The predicted values of equivalence ratio at $T_{b.max}$ are really closer, which is a good signal, showing that it can generate results that are reliable.

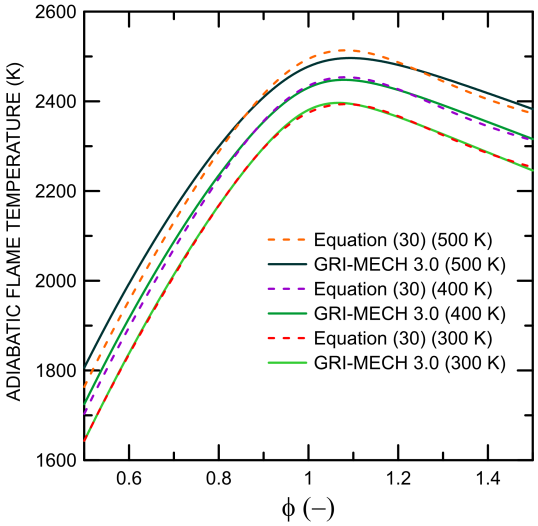

Figure 4.23 Predictions of adiabatic flame temperature of $H_2/O_2/N_2$ premixture, with an unburned gas temperature from 300 to 500 K, at 1 atm. Continuous line (—) are data computed by GRI-MECH 3.0, dashed lines (- - -) are predictions from equation (30).

The values of maximum adiabatic flame temperatures are also really close between equation (30) and GRI-MECH 3.0. $T_{b.max}$ obtained by equation (30) are 2393, 2453 and 2513 K for the unburned gas temperatures of 300, 400 and 500 K, while the ones gotten by GRI-MECH 3.0 are 2396, 2447 and 2496 K for the same values of T_u. It represents a deviation of 3, 5 and 17 K for the same unburned gas temperatures said before, which indicates that for higher values of T_u the error in $T_{b.max}$ predictions by equation (30) increases.

Another analysis of equation (30) was done, by changing the pressure. The comparisons were performed using pressure of 1, 5 and 20 atm, while also varying the unburned gas temperature. For an unburned gas temperature of 300 K and pressures of 1 and 5 atm the equation (30) generated results that fits the ones from the kinetic approach, while for higher pressure of 20 atm the deviations increased. Results are shown on figure 4.24a

For the values of maximum equivalence ratio, the results from equation (30) and GRI-MECH 3.0 were concordant. While for the pressures of 1 and 5 atm, the results obtained were 1.08 and 1.07, which is really close from the ones generated by GRI-MECH 3.0, that being 1.07 and 1.05. But the distance between the values of ϕ_{max} increases alongside P, as for the pressure of 20 atm, the value of maximum equivalence ratio obtained was 1.06 for equation (30), while for the simulator it is 1.03. This indicates that the difference in the value of ϕ_{max} is not so trustworthy as the pressure increases.

For the values of maximum flame temperatures obtained, it's possible to infer that the results generated were very satisfactory. The results gotten by equation (30) were 2393, 2437 and 2458 K for the pressures of 1, 5 and 20 atm, while the ones gotten by GRI-MECH 3.0 were 2396, 2438 and 2463 K.

For unburned gas temperature of 400 K, a little discrepancy on the lean zone can be observed, with a ΔT of 28 K until a equivalence ratio of 0.8. For the equivalence ratio between 0.8 and 1.2 the results are concordant from the ones extracted from GRI-MECH 3.0 and after that, the values tend to separate from each other. For that condition of T_u, the value of ϕ_{max} also agrees between equation (30) and GRI-MECH 3.0. The values of maximum equivalence ratio obtained by equation (30) were 1.08, 1.07 and 1.06 for pressures of 1, 5 and 20 atm, while from GRI-MECH 3.0, the values were 1.08, 1.06 and 1.04 for the same unburned gas temperatures. As for the maximum adiabatic flame temperatures, the results from the second equation shows a concordance with values from the simulator, with a maximum difference of 10 K between those values. Results are shown on figure 4.24b

The results obtained for the unburned gas temperature of 500 K while varying the pressure were not satisfactory as the ones gotten from T_u of 300 and 400 K. The only satisfactory results obtained are related to ϕ_{max} and the $T_{b.max}$, while the results generated for the lean and rich condition are not so concordant from equation (30) and GRI-MECH 3.0. The values of maximum equivalence obtained for equation (30) were 1.08, 1.07 and 1.06, for the pressures of 1, 5 and 20 atm, while the others from the simulator were 1.09, 1.07 and 1.05, for the same pressures, showing a good prediction by the empirical equation

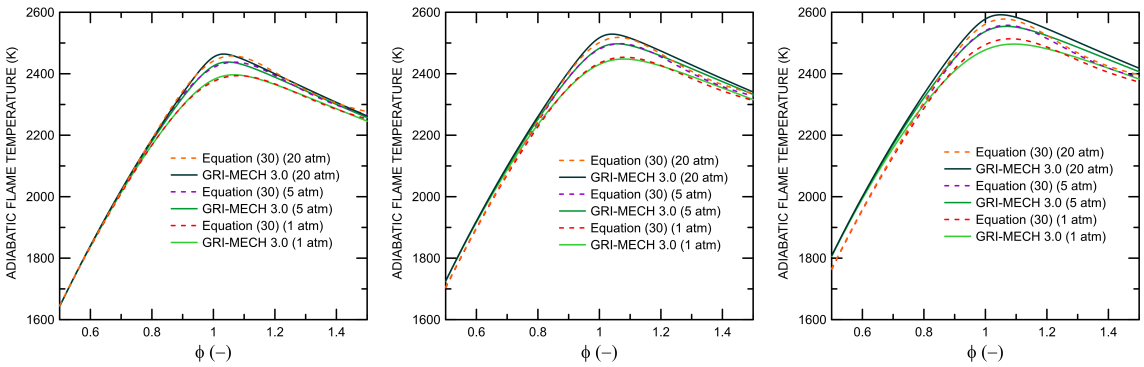

(a) T_u = 300 K **(b)** T_u = 400 K **(c)** T_u = 500 K

Figure 4.24 Effect of pressure, from 1 to 20 atm, on the adiabatic flame temperature, for $H_2/O_2/N_2$ flames, unburned gas temperatures from 300 to 500 K. **(a)** T_u = 300 K, **(b)** T_u = 400 K, **(c)** T_u = 500 K. Continuous line (—) are results from GRI-MECH 3.0, dashed lines (- - -) are results from equation (30).

on that. As for the maximum adiabatic flame temperature, the results gotten by equation (30) were 2513, 2557 and 2578 K for the pressures cited before, while for results from GRI-MECH 3.0 were 2496, 2554 and 2591 K for the same pressures. The maximum differences between those temperatures were 17 K, which is not a high deviation. The poor results from the equation (30) comes from lean and rich condition, specifically before a equivalence ratio of 0.9 and after 1.2, where a difference of 55 K can be observed throughout the lean zone, while a average difference of 20 K can be observed in the rich zone. So, equation (30) can be said to generate good results on the region of ϕ between 0.9 and 1.2. Results shown on figure 4.24c.

The profile of mean deviation and maximum deviation between GRI-MECH 3.0 and equation (30) results of the adiabatic flame temperature can be seen on figure 4.25. Mean deviation from those results increase alongside the unburned gas temperature and pressure, so the results from equation (30) are less concordant, or do not generate reliable results. For example, while unburned gas temperature is 300 K and pressure is at standard conditions, mean deviation is about 2 K. On the other hand for T_u of 500 K and a pressure of 20 atm the mean deviations can go up to 33 K. Those results can be seen on figure 4.25a. The maximum deviation on the other hand only increases alongside unburned gas temperature, and just a bit with pressure. This indicates that equation (30) equation generates better results with changes in pressure and less with changes in the unburned gas temperature. Results can be seen on figure 4.25b.

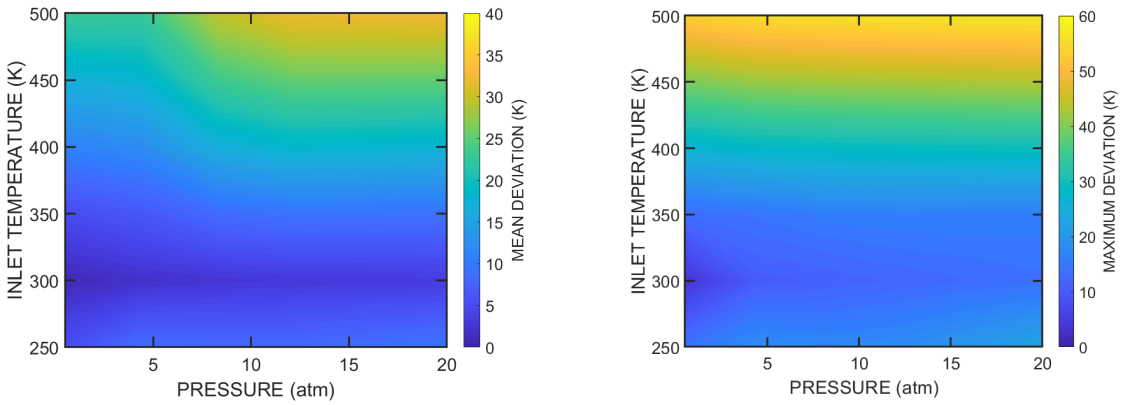

(a) Mean deviation

(b) Maximum deviation

Figure 4.25 Mean and maximum deviations in the predictions of adiabatic temperature of $H_2/O_2/N_2$ flames between the values generated by kinetic calculations using GRI-MECH 3.0 and equation (30), $\phi = 1.0$. **(a)** Mean temperature deviation (K), **(b)** maximum temperature deviation (K).

4.2 Laminar flame speed

In this section, studies concerning the influence of simulation parameters, kinetic mechanism validation, equivalence ratio, from 0.3 to 3.0, pressure, from 0.5 to 5 atm, unburned gas temperature, from 298 to 443 K, as well as the composition of fuel on the laminar flame speed (S_L) were made. The laminar flame speed is an important parameter for a premixed flame since it encapsulates the core information of the combustible mixture's diffusivity, reactivity, and exothermicity [124].

4.2.1 Numerical code coefficients

The numerical code used to compute laminar flame (algorithm 3.2) speed require numerical parameters, namely the domain width (m), which is a system characteristic, slope, ratio and curve, which are associated to the numerical model, to produce the output data. It is fundamental that the results generated by the kinetic mechanism are independent from the numerical parameters from the calculation method. Tests were performed by changing the values of width, slope, ratio and curve, using GRI-MECH 3.0, for the values of ϕ of 0.7, 1.0 and 1.3, using a premixture of $H_2/O_2/N_2$, with a unburned gas temperature of 300 K, at 1 atm. Results are shown on figure 4.26.

Normalization of the results was done dividing the flame speed obtained with a certain set of numerical parameters, by the S_L obtained using the default code set. Computed data shows that the alterations of width (figure 4.26a) and slope (figure 4.26b) doesn't influence significantly the predicted values of S_L. The deviation gotten when changing the width was always lower than ±0.5 %, so the default value of 0.03 m generates trustworthy results. When looking at values when changing slope, one can that the deviation gotten is also lower than ±0.5 %, and it suggests that the default value generates good results.

The deviation obtained from adjusting ratio demonstrates that any value other than 2 can be used, as the same result is obtained for all tested values. However because the flame speed remains constant, the default value of 3 was used. The deviation obtained from the curve values is less than 0.5 %, which is a modest number, hence the default value of 0.12 was kept. Its shows that the default values from the code generates feasible results, and so, those values were adopted for the rest of the work.

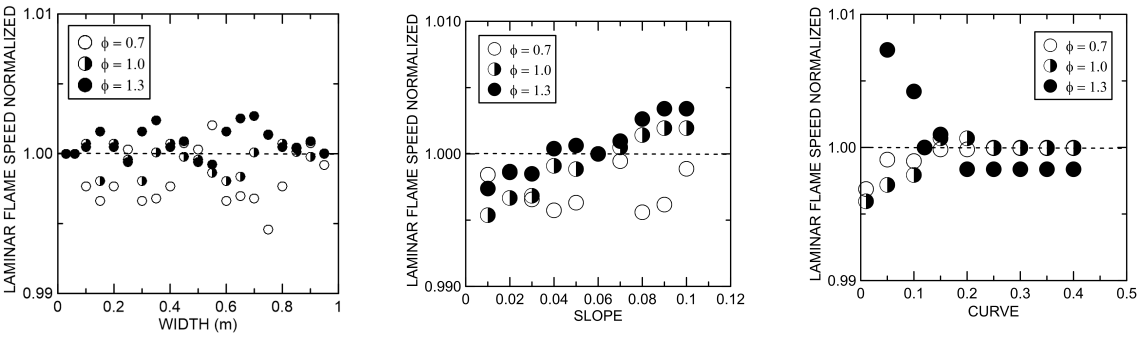

(a) Width **(b)** Slope **(c)** Curve

Figure 4.26 GRI-MECH 3.0 mechanism: effect of main numerical code coefficients on the computed values of laminar flame speed (normalized), for a $H_2/O_2/N_2$ flame, unburned gas temperature of 300 K, at 1 atm. Equivalence ratio of 0.7, 1.0 and 1.3. Coefficients tested: **(a)** Width, **(b)** Slope and **(c)** Curve.

4.2.2 Kinetic mechanism validation

All the kinetic mechanisms cited in chapter 3 were developed for different fuels and may generate different outputs. In this section, kinetic mechanism output validation and comparison with data from literature will be presented. The kinetic mechanisms tested were GRI-MECH 3.0, San Diego Mech, Qin Mech and Boivin Mech. The conditions were an unburned gas temperature of 300 K, at 1 atm, using $H_2/O_2/N_2$ flame, and equivalence ration varying from 0.3 to 3.0.

The results from the literature show great dispersion of results, although agreement is observed between the values extracted from Kwon *et al.* [139], Scholte *et al.* [140], and Dong *et al.* [141]. It is observed that in lean condition the dispersion of the results is not so remarkable, being the same more visible in rich combustion conditions. This dispersion of results may be a result of different techniques, conditions and operation errors that can occur during the experimentation. Moreover, the maximum values of the laminar flame speed $S_{L.max}$ are different from each other. The results generated by the kinetic mechanisms show that they satisfactorily describe the behaviour of the flame speed, and also show a dispersion of results similar to the experimental values. The results are shown on figure 4.27.

Maximum laminar flame speed ($S_{L.max}$) obtained by Boivin, San Diego Mech, GRI-MECH 3.0 and Qin Mech are shown on table 4.7. The point where the laminar flame speed reach its maximum ($\phi_{SL.max}$) were the same for all mechanisms tested, with a value of 1.65. Results shows a good agreement on the value of $\phi_{SL.max}$, but a deviation on the value of $S_{L.max}$ on Qin Mech if compared to the other kinetic mechanisms.

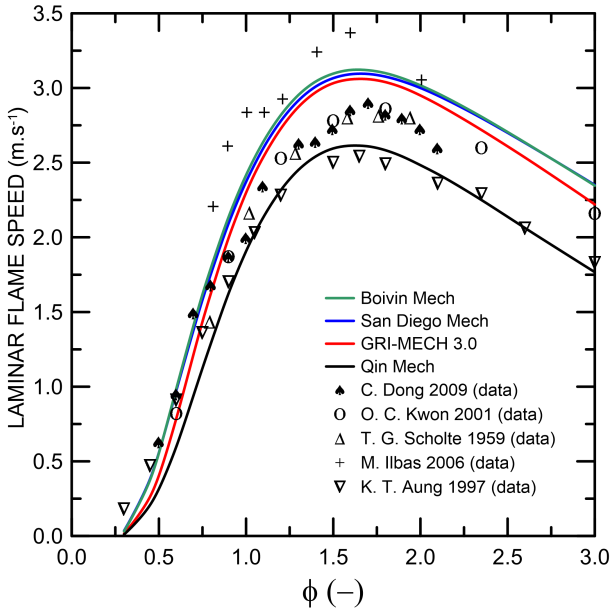

Figure 4.27 Laminar flame speed, of $H_2/O_2/N_2$ flames with unburned gas temperature of 300 K, at 1 atm. Lines: kinetic simulation results. Symbols: bibliographic data [139–143].

On lean condition, it is possible to observe an increase on the laminar flame speed alongside the increase of ϕ, all the way to stoichiometry and further away on rich condition. On rich combustion is possible to see a increase of laminar flame speed all the way to a peak value, and after that, it's possible to see that laminar flame speed starts to decrease.

A study was made to compare the values of ϕ where the laminar flame speed and adiabatic flame temperature had their peaks. Results are shown on figure 4.28. Results shows that the maximum peaks for those parameters weren't the same equivalence ratio, as the adiabatic flame temperature had it peak with a equivalence ratio of 1.06, while the laminar flame speed had it peak with a ϕ of 1.65, so the second one is shifted towards the rich zone if compared to the first. No justification in the literature has been found to explain this phenomenon, but when studying at the combustion of the H_2, one see that there is no formation of CO_2 or CO. Those are oxygenated species, and as seen earlier, have their peak near the stoichiometry. Other factors, such as the transport properties

Table 4.7 Numerical results of $S_{L.max}$, using Boivin Mech, San Diego Mech, GRI-MECH 3.0 and Qin Mech. $H_2/O_2/N_2$ flame, unburned gas temperature of 300 K at 1 atm. $\phi_{SL.max}$ obtained for all mechanisms was 1.65.

Kinetic mechanism	Boivin Mech	San Diego Mech	GRI-MECH 3.0	Qin Mech
$S_{L.max}$ ($m\,s^{-1}$)	3.12	3.09	3.06	2.61

used in the simulation also have an impact on this prediction. New studies should be done to better understand this phenomenon.

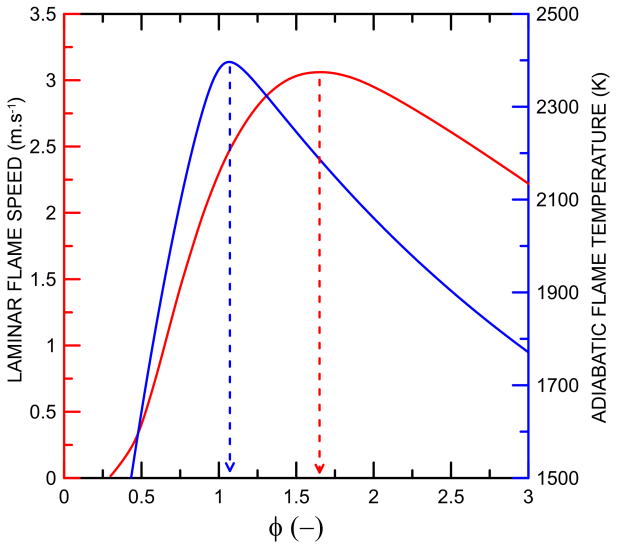

Figure 4.28 GRI-MECH 3.0 mechanism: distribution of laminar flame speed and adiabatic flame temperature of $H_2/O_2/N_2$ flame, unburned gas temperature of 300 K, at 1 atm, where: (—) is the laminar flame speed (left axis) and (—) is the adiabatic flame temperature (right axis).

4.2.3 Effect of pressure

GRI-MECH 3.0 and Boivin Mech showed satisfactory results simulating the laminar flame speed of $H_2/O_2/N_2$ flame, with a unburned gas temperature 300 K, at 1 atm. So a study to see the effect of pressure, with a T_u of 300 K was performed using those kinetic mechanism. The study was performed using pressure in range of 0.5 to 20 atm.

A direct comparison on the laminar flame speed at 1 and 20 atm shows that it decreases as pressure increases, while also shifting $\phi_{SL.max}$ towards stoichiometry. This behaviour is the opposite to what happened to the adiabatic flame temperature, and this might be explained by the decrease on the concentration of radicals H and OH, as showed on section 4.1.3 and proposed by B. J. Zhong [144]. Results shows that lower pressure (0.5 atm) generates higher flame speeds, when the values of ϕ are between 1.5 and 2.0. Also, when working at lean combustion and increasing pressure, one can see that S_L values drops significantly. For the same ϕ of 1, the S_L has a value of 2.29 $m\,s^{-1}$ for a pressure of 1 atm, and 0.96 $m\,s^{-1}$ for a pressure of 20 atm (figure 4.29a). Maximum laminar flame speed obtained at 0.5, 1, 5 and 20 atm were 3.06, 3.01, 2.92 and 1.78 $m\,s^{-1}$ respectively, while the values of $\phi_{SL.max}$ obtained were 1.65 at 0.5 and 1 atm, 1.6 at 5 atm and 1.5 at 20 atm. Results are shown on figure 4.29.

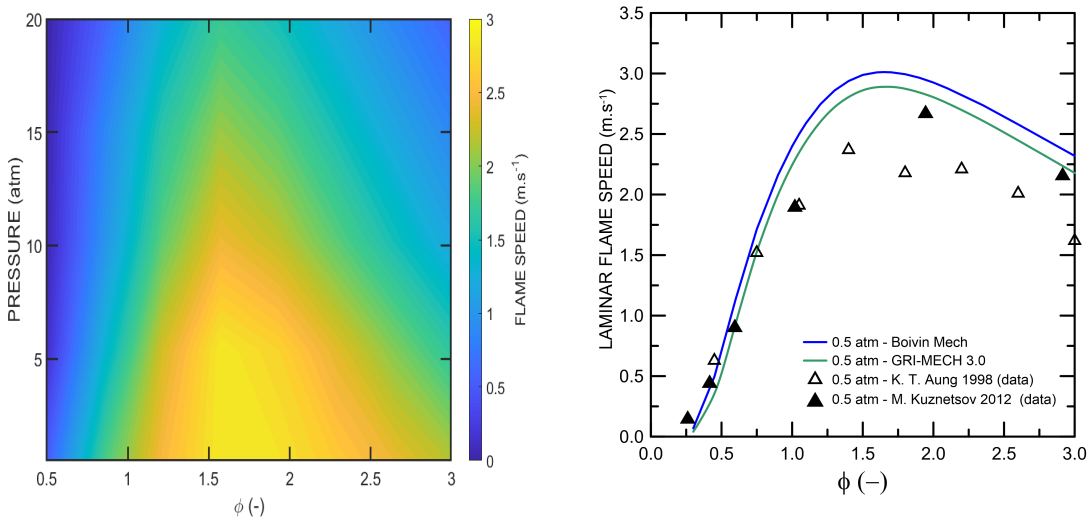

(a) ϕ and P vs S_L

(b) 0.5 atm comparison

Figure 4.29 Effect of pressure, from 0.5 to 5 atm, on the laminar flame speed, using Boivin and GRI-MECH 3.0, for a $H_2/O_2/N_2$ flame, with unburned gas temperature of 300 K, in function of equivalence ratio, where: **(a)**ϕ and P vs S_L. **(b)** 0.5 atm comparison. Lines: kinetic simulation results. Symbols: bibliographic reference data [145, 146].

As no experimental data was found to compare the results at elevated pressure ($P \geq$ 1 atm), only a comparison with data at 0.5 atm was conducted. After a direct comparison (fig. 4.29b), it can be seen that the values of S_L were lower than the one gotten by the simulation, but the behaviour is similar between them. In conclusion, GRI-MECH 3.0 and Boivin don't predict with a good accuracy the results of S_L at low pressures.

4.2.4 Effect of unburned gas temperature

The unburned gas temperature is a further variable that has been researched and has an impact on laminar flame speed. The study was carried out for a T_u varying from 300 to 443 K, while maintaining a constant pressure of 1 atm, using GRI-MECH 3.0 as the kinetic mechanism. GRI-MECH 3.0 showed satisfactory results, because of it, was the only kinetic mechanism used in this study.

Results shows that an increase on T_u increases S_L as well, that being observed on lean and rich conditions. This comes to what is expected, as dissociation reactions that produce free radicals are accelerated by high temperatures. The combustion reaction is started by these radicals, which is why the laminar flame speed increases. Similarly, as the unburned gas temperature rises, the adiabatic flame temperature rises, and reaction rates increase [130, 148]. Qualitative results obtained by simulations are similar to the

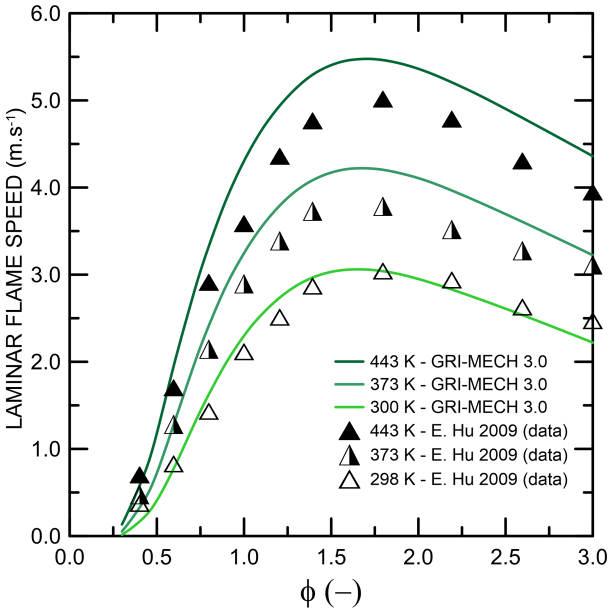

Figure 4.30 GRI-MECH 3.0 mechanism: effect of unburned gas temperature (from 300 to 443 K), at 1 atm, using a $H_2/O_2/N_2$ premixture. Lines: kinetic simulation results. Symbols: bibliographic data [147].

ones observed by experimental data extracted from E. Hu *et al.* [147], but quantitative results are only similar with the unburned gas temperature of 298 K. Results are shown on figure 4.30.

A increase on T_u also shifts $\phi_{SL.max}$ towards rich zone, starting with a value of 1.65 at 300 K and ending with 1.7 at 443 K. Also, the values of $S_{L.max}$ obtained are 3.06, 4.22 and 5.47 $m\,s^{-1}$ for a unburned gas temperature of 300, 373 and 443 K respectively. Data obtained are shown on table 4.8.

Table 4.8 GRI-MECH 3.0 mechanism: values of $S_{L.max}$ ($m\,s^{-1}$) and $\phi_{SL.max}$, with unburned gas temperatures of 300, 373 and 443 K, at 1 atm, with a $H_2/O_2/N_2$ premixture.

T_u (K)	$S_{L.max}$ ($m\,s^{-1}$)	$\phi_{SL.max}$ (–)
300	3.06	1.65
373	4.22	1.65
443	5.47	1.70

4.2.5 Methane flames

In this section, computation of methane laminar flame speed will be analyzed. Simulations were performed with $CH_4/O_2/N_2$ premixture, unburned gas temperature of 300 K at 1 atm, using GRI-MECH 3.0, San Diego Mech and Qin Mech as kinetic mechanisms. Results were compared with published data.

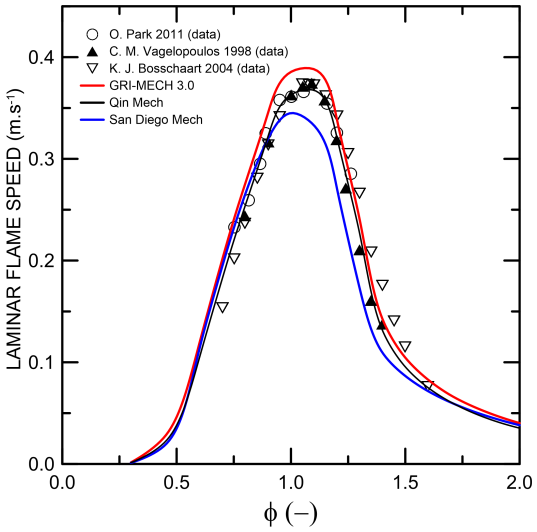

Figure 4.31 Laminar flame speed of a $CH_4/O_2/N_2$ premixture, with an unburned gas temperature of 300 K, at 1 atm. Lines: kinetic simulation results. Symbols: published experimental data [149–151].

The behaviour observed on the laminar flame speed from methane combustion with O_2 and N_2 is similar to what happened with hydrogen flames. First, an increase on the flame speed all the way in the lean zone, reaching a peak this time closer to stoichiometry. After the peak, on the rich zone, flame speed tens to decrease as ϕ increases. The results from the kinetic mechanisms used are satisfactory, as all of them presents good qualitative and quantitative values, if compare to results from K. J. Bosschaart [149], C. M. Vagelopoulos [150] and O. Park [151]. Results are shown on figure 4.31.

The laminar flame speed obtained for methane combustion is lower when compared to hydrogen combustion. The values of $S_{L.max}$ observed were lower than $0.4\,\mathrm{m\,s^{-1}}$ as predicted with all kinetic mechanisms tested. Hydrogen flames could reach values higher than $3\,\mathrm{m\,s^{-1}}$, and this must be due to transport properties and lower adiabatic flame temperature if compared to hydrogen (see section 4.1.6). Also, the values of $\phi_{SL.max}$ are closer to stoichiometry than the one observed by hydrogen combustion. The values of $S_{L.max}$ and $\phi_{SL.max}$ are found on table 4.9.

Also, the value of ϕ_{max} and $\phi_{SL.max}$ are closer in methane combustion, with the first one being 1.03 and second one 1.10 (figure 4.32).

Table 4.9 Values of $S_{L.max}$ and $\phi_{SL.max}$ for different kinetic mechanisms, with a premixture of $CH_4/O_2/N_2$, unburned gas temperature of 300 K at 1 atm.

Kinetic mechanism	$S_{L.max}$ ($\mathrm{m\,s^{-1}}$)	$\phi_{SL.max}$ (–)
GRI-MECH 3.0	0.38	1.10
San Diego Mech	0.34	1.00
Qin Mech	0.37	1.10

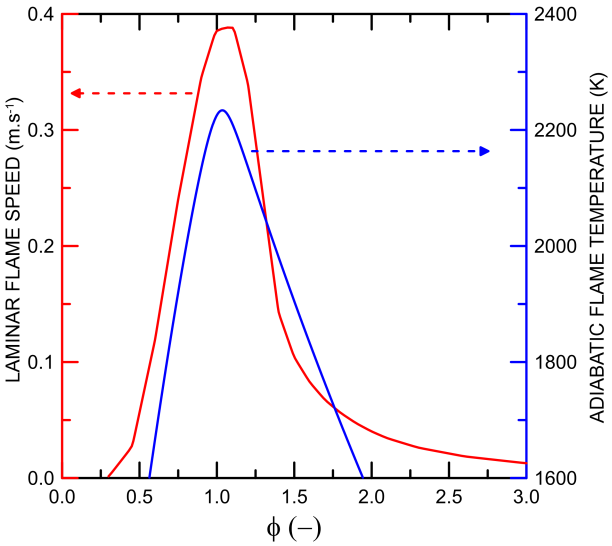

Figure 4.32 GRI-MECH 3.0 mechanism: comparison between the values of $\phi_{SL.max}$ and ϕ_{max}, from a premixture of $CH_4/O_2/N_2$, with an unburned gas temperature of 300 K, at 1 atm, where: (—) is the laminar flame speed (left axis) and (—) is the adiabatic flame temperature (right axis).

4.2.6 Fuel blends of $H_2/CH_4/O_2/N_2$

Another study of this work, was to observe the laminar flame speed of a fuel blend composed by hydrogen and methane. It was performed with a unburned gas temperature of 300 K, at 1 atm, O_2/N_2 as the oxidant, using GRI-MECH 3.0, San Diego Mech and Qin Mech.

A first look on a equimolar mixture of a fuel composed by H_2/CH_4, shows that the laminar flame speed is closer to the one gotten with a $CH_4/O_2/N_2$ premixture (see section 4.2.5) than the one with a $H_2/O_2/N_2$ premixture (see section 4.2.2). This indicates that methane has more weight on this property than hydrogen. All the results obtained by simulation had good agreement in a qualitative and quantitative way, when comparing the results with experimental data from N. Donohoe [152] and E. Hu [153]. Those results are shown on figure 4.33.

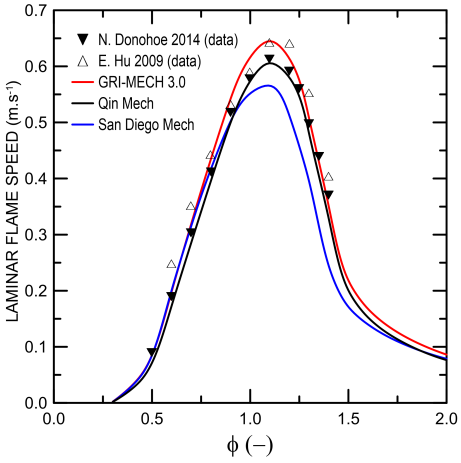

Figure 4.33 Laminar flame speed of a CH_4/H_2 (50/50 molar)$/O_2/N_2$ flame, using GRI-MECH 3.0, Qin Mech and San Diego Mech with an unburned gas temperature of 300 K at 1 atm. Lines: kinetic simulation results. Symbols: Bibliographic reference data [152, 153].

Values of $S_{L.max}$ appears near stoichiometry, as happened to pure methane flames and they are higher than the ones gotten with CH_4 flames. Results of $S_{L.max}$ and $\phi_{SL.max}$ are shown on table 4.10.

Table 4.10 Values of $S_{L.max}$ and $\phi_{SL.max}$ simulated by GRI-MECH 3.0, San Diego Mech, Qin Mech, for CH_4/H_2 (50/50 molar)$/O_2/N_2$ flame, unburned gas temperature of 300 K, at 1 atm.

Kinetic mechanism	$S_{L.max}$ (ms^{-1})	$\phi_{SL.max}$ (–)
GRI-MECH 3.0	0.64	1.10
San Diego Mech	0.56	1.10
Qin Mech	0.60	1.10

A brief summary about this section so far is shown on table 4.11.

Table 4.11 Summary of results from section 4.2.

Parameter	Effect	$S_{L.max}$,$\phi_{SL.max}$
Kinetic mechanism	• Agreement on S_L between experimental and numerical results from GRI-MECH 3.0, San Diego Mech, Qin Mech and Boivin Mech.	• Discrepancy on the values of $S_{L.max}$, but agreement on $\phi_{SL.max}$ for all fuels tested.
ϕ (–) [0.3 *to* 3.0]	• ↑ flame speed through lean condition; • Peak located at rich condition; • ↓ flame speed after the peak.	• Located at rich combustion condition.
P (atm) [0.3 *to* 20]	• ↑ on pressure = ↓ flame speed.	• ↑ of P = ↓ of $S_{L.max}$; • ↑ of P = shift to stoichiometry.
T_u (K) [250 *to* 500]	• ↑ on unburned gas temperature = ↑ flame speed.	• ↑ of T_u = ↑ of $S_{L.max}$; • ↑ of T_u = shift to rich zone.
Fuel composition [H_2, CH_4]	• $H_2/O_2/N_2$ flames has higher flame speed than $CH_4/O_2/N_2$ flames (about 9 to 10 times higher); • Fuel mix of H_2/CH_4 50 % molar has properties more similar to $CH_4/O_2/N_2$ flame.	• H_2 values of $S_{L.max}$ are higher than CH_4; • H_2 values of $\phi_{SL.max}$ are higher than CH_4.

4.3 Flame stability

The stability and operation limits of a laminar flame, using natural gas (NG) fuel with addition of hydrogen will be discussed in this section. The composition of the natural gas used in the calculations was 95.0 % of CH_4, 3.3 % of ethane (C_2H_6), 1.0 % of N_2 and 0.7 % of CO_2 [154]. To provide a baseline for comparison, the tests were first carried out for a pure NG/air laminar flame. In a second phase, the influence of the addition of H_2 in a mixture with NG/air was also studied. The mixture where hydrogen is added to natural gas is called hydrogen enriched natural gas (HENG). Numerical simulation were performed with an unburned gas temperature of 300 K, at 1 atm, varying the equivalence ratio, from 0.7 (lean), 1.0 (stoichiometric) and 1.3 (rich), and hydrogen percentage on the fuel (0, 20 and 40 %).

4.3.1 Natural gas flame

To find the operation limits of a flame, a set of calculations must be performed, so that the constraints will define the range of diameters where the flame is stable to flow fluctuations (figure 3.9 on section 3.4). The first analysis was done with NG/air flame, at stoichiometry, to observe its stability region and optimum operation area. The conditions used is shown on table 4.12.

Table 4.12 GRI-MECH 3.0 mechanism: simulation values of equivalence ratio, laminar flame speed, flashback and blowoff gradients, dynamic viscosity and density from the unburned gas mixture. Conditions: $CH_4/O_2/N_2$ flame, T_u = 300 K, at 1 atm.

Parameter	ϕ (–)	S_L ($m\,s^{-1}$)	g_F (s^{-1})	g_B (s^{-1})	μ ($kg\,m^{-1}\,s-1$)	ρ ($kg\,m^{-3}$)
Value	1.00	0.39	461.00	1986.00	1.891×10^{-5}	1.111

NG/air flames tends to be stable for tube diameters in range of 4.0 to 26.0×10^{-3} m (blue lines region), which is a wide rage of work. The optimum area (grey area), where the flame is stable even with flow velocities fluctuation, has a value of 66.2×10^{-4} $m^2\,s^{-1}$ and is located in a diameter in range of 8.0 to 13.0 $\times10^{-3}$ m. Those values will be used to compare with HENG. Results are shown on figure 4.34.

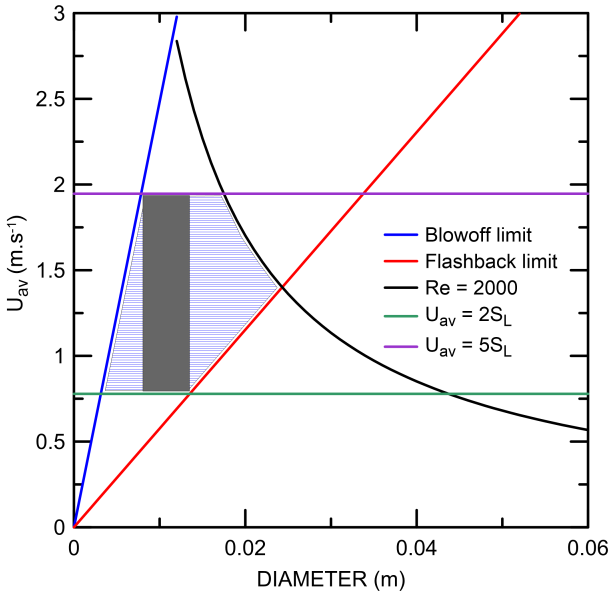

Figure 4.34 Glassman diagram for a $CH_4/O_2/N_2$ flame, T_u of 300 K, 1 atm, at stoichiometry. Blue stripped area shows the stability limits; Grey solid area is the optimum area.

4.3.2 Hydrogen enriched natural gas flame

In a second analysis, addition of H_2 to a mixture with NG was performed to observe changes in the operating limits. In addition, the effect of the equivalence ratio was also studied. The values H_2 content on HENG tested were 0, 20, 40 %, while the values of ϕ tested were 0.7, 1.0, 1.3. The conditions used in the test are summarized on table

As can be seen, there is a variety of results, depending on the equivalence ratio and hydrogen content on HENG. First, it is possible to notice that the increase on H_2 content in HENG decreases the optimum diameter range (except on lean conditions). Also, when ϕ increases, from lean conditions to stoichiometry, burner diameter decreases. After that, it is possible to notice that the burner diameter range increases again (ϕ>1.0). The results are shown on figure 4.35.

The largest diameters where the flame is stable are found when there is no H_2 in the fuel blend. Maximum diameter obtained was in those conditions, with it varying from 18 to 54×10^{-3}m. Maximum admission flows are achieved at stoichiometry and 40 % of H_2 (2.71 m s^{-1}), and this is because hydrogen flame speed is higher when compared to CH_4, and because of H_2 content increment, the admission flow also increases. On the other hand, lower admission flow is achieved at lean condition and pure methane fuel (1.01 m s^{-1}).

When comparing the optimum operation areas, one can see that highest diameter ranges are achieved at rich conditions. Highest range of optimum diameters are observed with an equivalence ratio of 1.3 and 0 % H_2 content, with the diameter in range of 4.0 to 24.0×10^{-3} m. Between all H_2 content on HENG simulated, the highest area is attained when hydrogen content is 40 %. Areas obtained on rich conditions are 16.7×10^{-3} m^2 s^{-1},

15.4×10^{-3} $m^2\,s^{-1}$ and 18.4×10^{-3} $m^2\,s^{-1}$ for a hydrogen content of 0.0, 20.0 and 40.0 % respectively.

Table 4.13 GRI-MECH 3.0 mechanism: simulation values of equivalence ratio, H_2 content on HENG, laminar flame speed, flashback and blowoff gradients, dynamic viscosity and density from the unburned gas mixture. Conditions: HENG/air flame, T_u = 300 K, at 1 atm.

Parameter	H_2 content (%)	S_L ($m\,s^{-1}$)	g_F (s^{-1})	g_B (s^{-1})	μ ($kg\,m^{-1}\,s-1$)	ρ ($kg\,m^{-3}$)
ϕ = 0.7	0	0.20	83.87	175.20	1.820×10^{-5}	1.136
	20	0.23	157.27	461.2	1.822×10^{-5}	1.121
	40	0.28	230.67	747.20	1.824×10^{-5}	1.101
ϕ = 1.0	0	0.39	461.00	1986.00	1.891×10^{-5}	1.111
	20	0.45	781.00	3766.00	1.888×10^{-5}	1.091
	40	0.54	1101.00	5546.00	1.884×10^{-5}	1.064
ϕ = 1.3	0	0.24	152.87	3796.80	1.786×10^{-5}	1.109
	20	0.30	262.27	7070.80	1.789×10^{-5}	1.084
	40	0.41	371.67	10344.80	1.794×10^{-5}	1.049

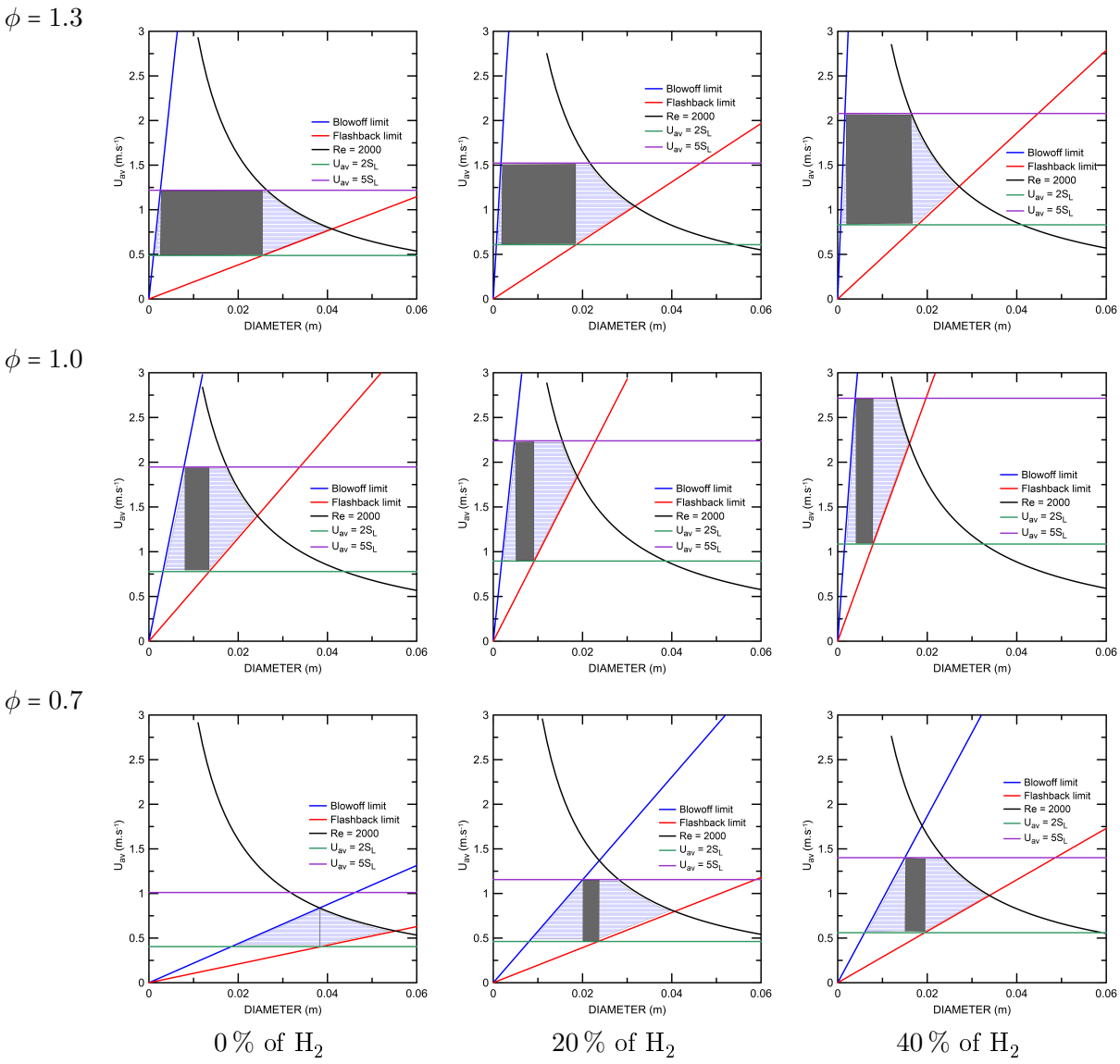

Figure 4.35 Compilation of Glassman diagrams for a HENG/air flame, T_u of 300 K, 1 atm. Equivalence ratio tested: 0.7, 1.0 and 1.3; H_2 content tested: 0.0, 20.0 and 40.0 %. Blue stripped area shows the stability limits; Grey solid area is the optimum area.

Chapter 5

Conclusions and future work

5.1 Conclusions

In this master's thesis, it was investigated the flame behaviuor of H_2, CH_4, H_2/CH_4, H_2/Biogas and HENG, using O_2/N_2 (1/3.728) as oxidant. The main conclusion will be divided into the three sections: *i*) adiabatic flame temperature, *ii*) laminar flame speed, and *iii*) flame stability and operation limits.

Regarding the adiabatic flame temperature, it was observed the high influence of the equivalence ratio (ϕ), where it was noted an increase in T_b toward stoichiometry, and its peak value in rich burning condition, just above the stoichiometry. After the maximum, the decrease in T_b was observed with the increase of ϕ in the rich zone. It was also noticed that the most relevant intermediary radicals formed were O, OH, H, HO_2 and the H_2O_2 species. All the five tested kinetic mechanisms tested showed excellent results when compared the simulations with the literature data.

Regarding the variation of the tested conditions, it was observed that pressure and T_b were directly proportional, besides making ϕ_{max} shift towards stoichiometry. It was also observed that increasing pressure decreases dissociation reactions (decreasing flame radical concentration), which mostly happen near stoichiometry. Increasing the temperature of the unburned gases also causes the adiabatic flame temperature to increase, being mainly associated with the preheating of the fuel mixture. In addition ϕ_{max} value shifts towards the rich zone. The increase in T_u also decreases the dissociation reactions. In general, it can be said that $T_{b.max}$ increases directly proportionally with T_u and pressure, while ϕ_{max} increases along with T_u but decreases with increasing pressure.

The rate of change of adiabatic flame temperature in the lean zone tends to increase with increasing pressure and decrease with increasing T_u, and the same effect can be observed at rich conditions. When comparing the adiabatic temperature of CH_4 and H_2 flames, it was observed that H_2 flames were always hotter, being 162 K hotter when reaches

the maximum adiabatic temperature. Also, the ϕ_{max} value of the methane flame was closer to stoichiometry compared to the flame of H_2.

As for the effects generated by T_u and by pressure in the CH_4 flames, the same behaviour cited for the H_2 flames was observed. The lower temperature of the CH_4 flame may be due to the formation of CO and CO_2, since they can "steal" the full heat generated by the flame. The CO is a product species that should be avoided, since it is toxic.

When comparing flames of H_2, CH_4, mixture of H_2/CH_4 (50/50 molar) and biogas, the following trend was observed regarding flame temperature: H_2 > mixture of H_2/CH_4 (50/50 molar) > CH_4 > biogas. As for the mixture of H_2/biogas, it was observed that higher values of T_b were obtained for high T_u, P and higher H_2 content. Thus one can take advantage of the CO_2 rich biogas in a mixture with H_2.

Among the proposed empirical equations, polynomial approximations with a higher number of polynomial terms show good results, but only the rational equation (30) was able to effectively replicate the values of T_b when changes of T_u, P and ϕ were imposed. The minimum mean error obtained, when compared to the results generated by GRI-MECH 3.0 was 5 K and the maximum was 35 K, obtaining better results for low pressures and T_u.

Regarding the flame speed, the values of the simulation parameters (width, slope, curve, ratio) used were appropriate, since the sensitivity tests caused a maximum deviation of ±0.5 % (figure 4.26). Furthermore, all the kinetic mechanisms tested (except Qin Mech) generated feasible results, as they were in agreement with the literature results.

For H_2 flames, under T_u conditions of 300 K and 1 atm, the peak of the maximum flame velocity was not at the same equivalence ratio value as the maximum adiabatic temperature, being 1.06 for the former and 1.65 for the later. As for the change in system pressure, it was observed that the GRI-MECH 3.0 and Boivin mechanism do not generate satisfactory results at pressures below atmospheric. As for the change in T_u, it was observed that the GRI-MECH 3.0 kinetic mechanism showed results that were in line with literature data.

For the CH_4 flames, all the kinetic mechanisms showed fair results when compared to the literature, where it can also be observed that the S_L peak was in an equivalence ratio close to that of the T_b peak. It was observed that the H_2 flames have a higher flame speed than the CH_4 flames (3.06 $m\,s^{-1}$ for H_2 and 0.38 $m\,s^{-1}$ for CH_4, when comparing the maximum flame speed, using GRI-MECH 3.0).

As for flame stabilization and operation limits, it was observed that increasing the content of H_2 in HENG decreases the optimal diameter range, with the exception of poor

burning conditions. Increasing ϕ, requires a decrease in the burner diameter ($0.7 \leq \phi \leq 1.0$) and then increases it again (1.0 to 1.3). The highest admission flow was for ϕ conditions of 1.0 and with 40.0 % of H_2 in HENG. The lowest admission flow was obtained at ϕ conditions of 0.7 and with H_2 content of 0.0 % at HENG. For ϕ values, increasing it generates larger optimal diameter ranges. The largest optimal operation area, on the other hand, was obtained for rich firing condition (ϕ of 1.3) and 40.0 % of H_2 in HENG, obtaining the value of 18.4×10^{-3} $m^2 s^{-1}$

5.2 Future work

It would be fascinating to see how all the variables investigated in this paper affect the concentration of NO_x in a study on the effects of H_2 flames in the future. As those subjects weren't covered in this work, new areas of research could include the examination of H_2 fuel blends with other hydrocarbons or fuels like ammonia. It may be interesting to understand the causes of the shift in the value of $\phi_{SL.max}$ to the rich zone for $H_2/O_2/N_2$ flame. Also, as there is currently no information available on the impact of high pressure on laminar flame speed of $H_2/O_2/N_2$ flame, new experimental and simulation work could be done to provide new information to the scientific community.

Appendix A

Work Disclosure

This thesis was published as a poster in iFEQB 2020/2021 and 2021/2022.

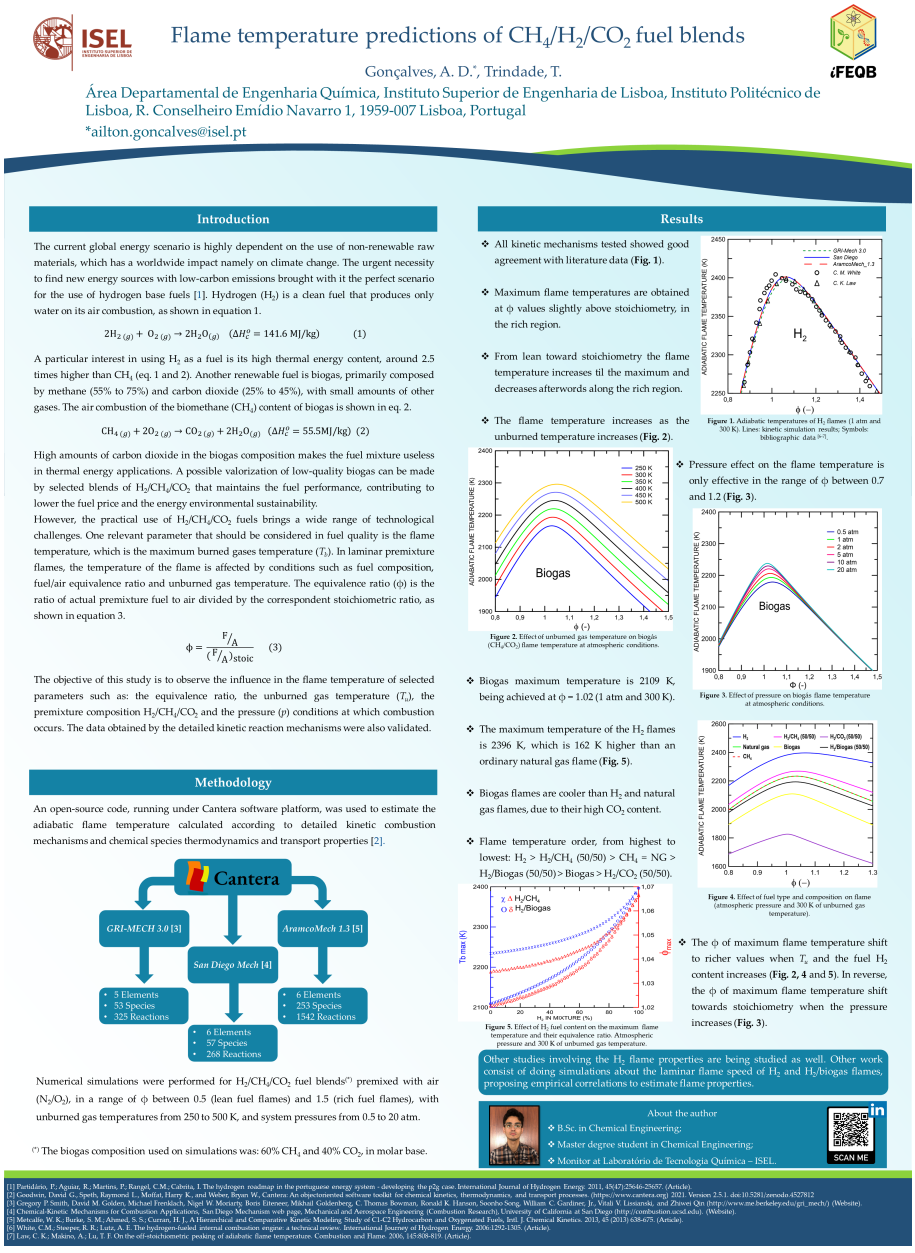

Figure A.1 iFEQB 2020/2021 poster.

Laminar flame stability, operation limit and adiabatic flame temperature prediction of $H_2/CH_4/O_2/N_2$ fuel blend

Gonçalves, A. D.*, Trindade, T.
Departamento de Engenharia Química, Instituto Superior de Engenharia de Lisboa, Instituto Politécnico de Lisboa, R. Conselheiro Emídio Navarro 1, 1959-007 Lisboa, Portugal
*ailton.goncalves@isel.pt

Introduction

The current global energy scenario is highly dependent on the use of non-renewable raw materials, which has severe impacts namely on worldwide climate changes. The urgent demand of new energy solutions having low-carbon emissions brought with it the perfect scenario for the use of hydrogen base fuels [1]. Hydrogen (H_2) is a clean fuel that produces only water on its air combustion.

$$2H_{2\,(g)} + O_{2\,(g)} \rightarrow 2H_2O_{(g)}$$

A particular interest in using H_2 as a fuel is its high thermal energy content (141.6 MJ/kg), around 2.5 times higher than CH_4 (55.5 MJ/kg). Several studies are being carried out for a better understanding of the phenomena related to hydrogen flames, as well as its mixture with other gases, such as methane. One of these studies is related to the calculation of its adiabatic flame temperature, important to characterize the quality of the fuel, determine the applicability of a certain fuel, among other important factors. This is affected by fuel composition, unburned gases temperature (T_u), pressure and the equivalence ratio (Φ), which is the ratio of actual premixture fuel to air divided by the correspondent stoichiometric ratio.

$$\Phi = \frac{F/A}{(F/A)_{stoic}}$$

A relevant topic is related to the operating limits, stability, and design of burners in which H_2 containing fuels will be used. It is important to design Bunsen type burners such as cooking stoves, as well as other combustion systems that uses laminar flames. The design of those burners is done based on Glassman diagrams [2], that considers the laminar flame speed (S_L) and phenomenon like flame blowoff and flashback, while working in laminar conditions (N_{Re} < 2000).

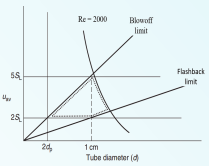

Figure 1. Glassman stability diagram highlights the operation limits of Bunsen burner [2].

Methodology

An open-source code, running under Cantera software platform, was used to estimate the adiabatic flame temperature and laminar flame speed calculated according to detailed kinetic combustion mechanisms and chemical species thermodynamics and transport properties [3].

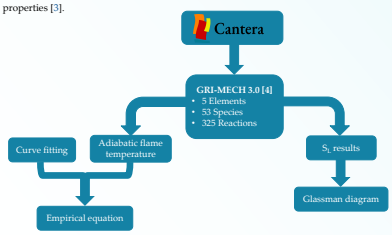

Numerical simulations were performed for pure H_2 and H_2/CH_4 fuel blend premixed with air (N_2/O_2). On the study concerning the adiabatic flame temperature, conditions were in a range of ϕ between 0.5 (lean fuel flames) and 1.5 (rich fuel flames), with unburned gas temperatures from 250 to 500 K, and system pressures from 1 to 20 atm. On the study concerning the stability and operation limits, the H_2 molar content in the fuel was varied from 0 to 40 % with the unburned gas temperature of 300 K and 1 atm.

Results

1. Flame temperature at adiabatic conditions:

Empirical equation looks like: $T_b = \left(\frac{a_0+b_1\Phi^2+c_1\Phi^4+d_0\Phi^{4^*}}{1+e_0\Phi^2+f_0\Phi^4+g_0\Phi^{4^*}}\right) + [-\alpha(300 - T_u)]$

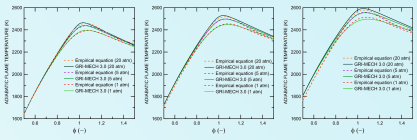

(a) 300 K **(b) 400 K** **(c) 500 K**

Figure 2. Effect of pressure, from 1 to 20 atm on adiabatic flame temperature, using a $H_2/O_2/N_2$ premixed flame for an unburned gas temperatures from 300 to 500 K, using GRI-MECH 3.0 and the empirical equation, where: **(a)** T_u=300 K, **(b)** T_u=400 K, **(c)** T_u=500 K.

- The flame temperature data predicted by the proposed empirical equation fairly agrees with the detailed computed results by GRI-MECH 3.0.
- As the unburned gas temperature and pressure increase, the empirical predictions of flame temperature deviations increases.
- The flame temperature mean deviation starts at a value of 1.4 K (300 K and 1 atm), with a maximum of 33.1 K (500 K and 20 atm).
- The flame temperature maximum deviation starts at value of 7.3 K (300 K and 1 atm), with a maximum of 57.4 K (500 K and 20 atm).

2. Flame stability region:

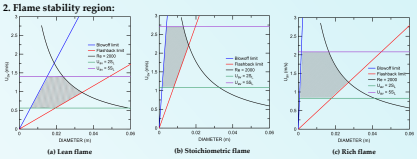

(a) Lean flame **(b) Stoichiometric flame** **(c) Rich flame**

Figure 3. Effect of the equivalence ratio on the stability area, with data produced by GRI-MECH 3.0. Conditions used were T_u of 300 K, at 1 atm, with a fuel mixture of H_2/CH_4 (40/60 % mol.), where: **(a)** Φ=0.7, **(b)** Φ=1.0, **(c)** Φ=1.3.

- The flame stability region increases toward rich flame conditions.
- At stoichiometry, the burner diameters of stable flame conditions is the lowest, starting at 4 mm and ending at 16 mm.

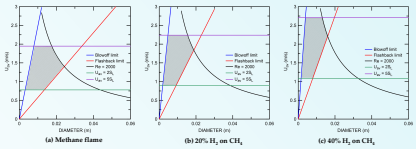

(a) Methane flame **(b) 20% H_2 on CH_4** **(c) 40% H_2 on CH_4**

Figure 4. Effect of H_2 content in the fuel mixture with CH_4 on the stability area, with data produced by GRI-MECH 3.0. Conditions used were T_u of 300 K, at 1 atm, at stoichiometry, where: **(a)** H_2 =0 %, **(b)** H_2 =20 %, **(c)** H_2 =40 %.

- The characteristic size of burner diameter in the flame stability region decreases as the H_2 content in the fuel increases.
- Flame stability area increases as the H_2 content on the fuel increases, but the diameter size range where the stability is achieved tends to decrease.
- Larger flame stability area and burner diameter size range are achieved for richer flames and higher H_2 content in fuel.

About the author
- B.Sc. in Chemical Engineering;
- Master degree student in Chemical Engineering;
- Monitor at Laboratório de Tecnologia Química – ISEL.

SCAN ME

[1] Partidário, P.; Agpiar, R.; Martins, P.; Rangel, C.M.; Cabrita, I. The hydrogen roadmap in the portuguese energy system - developing the p2g case. International Journal of Hydrogen Energy. 2011, 45(47):25646-25657.
[2] Glassman, I.; Yetter, R. A.; Glumac, N. G. Combustion, 5th edition. Academic press, Elsevier. 2015, ISBN 978-0-12-407913-7.
[3] Goodwin, David G., Speth, Raymond L., Moffat, Harry K., and Weber, Bryan W., Cantera: An object-oriented software toolkit for chemical kinetics, thermodynamics, and transport processes. (https://www.cantera.org) 2021. Version 2.5.1. doi:10.5281/zenodo.4527812
[4] Gregory P. Smith, David M. Golden, Michael Frenklach, Nigel W. Moriarty, Boris Eiteneer, Mikhail Goldenberg, C. Thomas Bowman, Ronald K. Hanson, Soonho Song, William C. Gardiner, Jr., Vitali V. Lissianski, and Zhiwei Qin (http://www.me.berkeley.edu/gri_mech/)

Figure A.2 iFEQB 2021/2022 poster.

Bibliography

[1] P. Partidário, R. Aguiar, P. Martins, C. M. Rangel, and I. Cabrita. The hydrogen roadmap in the portuguese energy system – Developing the P2G case. *International Journal of Hydrogen Energy*, 45(47):25646–25657, sep 2020.

[2] Secretaria de Estado Adjunta e da Energia. EN-H2 estratégia nacional para o hidrogénio. https://participa.pt/pt/consulta/en-h2-estrategia-nacional-para-o-hidrogenio, jul 2020.

[3] B. van Ruijven, J. F. Lamarque, D. P. van Vuuren, T. Kram, and H. Eerens. Emission scenarios for a global hydrogen economy and the consequences for global air pollution. *Global Environmental Change*, 21(3):983–994, aug 2011.

[4] United Nations. Framework convention on climate change COP21 Paris agreement. https://unfccc.int/process-and-meetings/the-paris-agreement/the-paris-agreement, dec 2016.

[5] M. Crippa, D. Guizzardi, M. Muntean, D. Schaaf, E. Solazzo, F. Monforti-Ferrario, J. Olivier, and E. Vignati. Fossil co2 emissions of all world countries - 2020 report. Other KJ-NA-30358-EN-N (online),KJ-NA-30358-EN-C (print), Luxembourg, 2020.

[6] K. O. Yoro and M. O. Daramola. CO_2 emission sources, greenhouse gases, and the global warming effect. In *Advances in Carbon Capture*, pages 3–28. Elsevier, 2020.

[7] J. P. Lesschen, M. van den Berg, H. J. Westhoek, H. P. Witzke, and O. Oenema. Greenhouse gas emission profiles of european livestock sectors. *Animal Feed Science and Technology*, 166-167:16–28, jun 2011.

[8] P. Friedlingstein *et. al.* Global carbon budget 2020. *Earth System Science Data*, 12(4):3269–3340, dec 2020.

[9] M. Niermann, S. Timmerberg, S. Drunert, and M. Kaltschmitt. Liquid organic hydrogen carriers and alternatives for international transport of renewable hydrogen. *Renewable and Sustainable Energy Reviews*, 135:110171, jan 2021.

[10] R. Derwent, P. Simmonds, S. O'Doherty, A. Manning, W. Collins, and D. Stevenson. Global environmental impacts of the hydrogen economy. *International Journal of Nuclear Hydrogen Production and Applications*, 1(1):57, 2006.

[11] H. Price, L. Jaeglé, A. Rice, P. Quay, P. C. Novelli, and R. Gammon. Global budget of molecular hydrogen and its deuterium content: Constraints from ground station, cruise, and aircraft observations. *Journal of Geophysical Research*, 112(D22), nov 2007.

[12] T. K. Tromp. Potential environmental impact of a hydrogen economy on the stratosphere. *Science*, 300(5626):1740–1742, jun 2003.

[13] K. H. Rosenlof. Changes in water vapor and aerosols and their relation to stratospheric ozone. *Comptes Rendus Geoscience*, 350(7):376–383, nov 2018.

[14] N. P. Brandon and Z. Kurban. Clean energy and the hydrogen economy. *Philosophical Transactions of the Royal Society A: Mathematical, Physical and Engineering Sciences*, 375(2098):20160400, jun 2017.

[15] FreedomCAR and Fuel Partnership. *Hydrogen Production. Overview of Technology Options.* jan 2009.

[16] J.D. Holladay, J. Hu, D.L. King, and Y. Wang. An overview of hydrogen production technologies. *Catalysis Today*, 139(4):244–260, jan 2009.

[17] I. Dincer and C. Acar. Review and evaluation of hydrogen production methods for better sustainability. *International Journal of Hydrogen Energy*, 40(34):11094–11111, sep 2015.

[18] M. Ahmed and I. Dincer. A review on photoelectrochemical hydrogen production systems: Challenges and future directions. *International Journal of Hydrogen Energy*, 44(5):2474–2507, jan 2019.

[19] R. Figaj and L. Vanoli. Chapter 13 - Hybrid and novel solar hydrogen systems. In *Solar Hydrogen Production*, pages 487–510. Academic Press, 2019.

[20] O. Bičáková and P. Straka. Production of hydrogen from renewable resources and its effectiveness. *International Journal of Hydrogen Energy*, 37(16):11563–11578, aug 2012.

[21] J. Baeyens, H. Zhang, J. Nie, L. Appels, R. Dewil, R. Ansart, and Y. Deng. Reviewing the potential of bio-hydrogen production by fermentation. *Renewable and Sustainable Energy Reviews*, 131:110023, oct 2020.

[22] A. Kadier, P. Jain, B. Lai, M. S. Kalil, S. Kondaveeti, K. F. S. Alabbosh, I. M. Abu-Reesh, and G. Mohanakrishna. Biorefinery perspectives of microbial electrolysis cells (MECs) for hydrogen and valuable chemicals production through wastewater treatment. *Biofuel Research Journal*, 7(1):1128–1142, mar 2020.

[23] S. G. Simoes, J. Catarino, A. Picado, T. F. Lopes, S. di Berardino, F. Amorim, F. Gírio, C.M. Rangel, and T. P. de Leão. Water availability and water usage solutions for electrolysis in hydrogen production. *Journal of Cleaner Production*, 315:128124, sep 2021.

[24] R. Kothari, D. Buddhi, and R.L. Sawhney. Comparison of environmental and economic aspects of various hydrogen production methods. *Renewable and Sustainable Energy Reviews*, 12(2):553–563, feb 2006.

[25] M. Ghazvini, M. Sadeghzadeh, M. H. Ahmadi, S. Moosavi, and F. Pourfayaz. Geothermal energy use in hydrogen production: A review. *International Journal of Energy Research*, aug 2019.

[26] I. A. Gondal, S. A. Masood, and M. Amjad. Review of geothermal energy development efforts in pakistan and way forward. *Renewable and Sustainable Energy Reviews*, 71:687–696, may 2017.

[27] R. Moradi and K. M. Groth. Hydrogen storage and delivery: Review of the state of the art technologies and risk and reliability analysis. *International Journal of Hydrogen Energy*, 44(23):12254–12269, may 2019.

[28] B. G. Pollet, I. Staffell, J.L. Shang, and V. Molkov. Fuel-cell (hydrogen) electric hybrid vehicles. In *Alternative Fuels and Advanced Vehicle Technologies for Improved Environmental Performance*, pages 685–735. Elsevier, 2014.

[29] B. Viswanathan. Hydrogen storage. In *Energy Sources*, pages 185–212. Elsevier, 2017.

[30] P. Song, Y. Sui, T. Shan, J. Hou, and X. Wang. Assessment of hydrogen supply solutions for hydrogen fueling station: A shanghai case study. *International Journal of Hydrogen Energy*, 45(58):32884–32898, nov 2020.

[31] H. Nazir, N. Muthuswamy, C. Louis, S. Jose, J. Prakash, Marthe E. Buan, C. Flox, S. Chavan, X. Shi, P. Kauranen, T. Kallio, G. Maia, K. Tammeveski, N. Lymperopoulos, E. Carcadea, E. Veziroglu, A. Iranzo, and A. M. Kannan. Is the H_2 economy realizable in the foreseeable future? part II: H_2 storage, transportation, and distribution. *International Journal of Hydrogen Energy*, 45(41):20693–20708, aug 2020.

[32] J. B. von Colbe, J. R. Ares, J. Barale, M. Baricco, C. Buckley, G. Capurso, N. Gallandat, D. M. Grant, M. N. Guzik, I. Jacob, E. H. Jensen, T. Jensen, J. Jepsen, T. Klassen, M. V. Lototskyy, K. Manickam, A. Montone, J. Puszkiel, S. Sartori, D. A. Sheppard, A. Stuart, G. Walker, C. J. Webb, H. Yang, V. Yartys, A. Zuttel, and M. Dornheim. Application of hydrides in hydrogen storage and compression: Achievements, outlook and perspectives. *International Journal of Hydrogen Energy*, 44(15):7780–7808, mar 2019.

[33] P. Xu, J. Zheng, H. Chen, and P. Liu. Optimal design of high pressure hydrogen storage vessel using an adaptive genetic algorithm. *International Journal of Hydrogen Energy*, 35(7):2840–2846, apr 2010.

[34] C. R. Matos, J. F. Carneiro, and Patrícia P. Silva. Overview of large-scale underground energy storage technologies for integration of renewable energies and criteria for reservoir identification. *Journal of Energy Storage*, 21:241–258, feb 2019.

[35] AMS composite cylinders. Choosing the right gas cylinder - type 1, type 2, type 3 or type 4? https://ams-composites.com/choosing-the-right-gas-cylinder-type-1-type-2-type-3-or-type-4/, sep 2020.

[36] H. Barthelemy, M. Weber, and F. Barbier. Hydrogen storage: Recent improvements and industrial perspectives. *International Journal of Hydrogen Energy*, 42(11):7254–7262, mar 2017.

[37] A. Peschel. Industrial perspective on hydrogen purification, compression, storage, and distribution. *Fuel Cells*, 20(4):385–393, aug 2020.

[38] J. Zheng, X. Liu, P. Xu, P. Liu, Y. Zhao, and J. Yang. Development of high pressure gaseous hydrogen storage technologies. *International Journal of Hydrogen Energy*, 37(1):1048–1057, jan 2012.

[39] R. Gerboni. Introduction to hydrogen transportation. In *Compendium of Hydrogen Energy*, volume 2, chapter 11, pages 283–299. Elsevier, 2016.

[40] I. A. Hassan, H. S. Ramadan, M. A. Saleh, and D. Hissel. Hydrogen storage technologies for stationary and mobile applications: Review, analysis and perspectives. *Renewable and Sustainable Energy Reviews*, 149:111311, oct 2021.

[41] R. R. Ratnakar, N. Gupta, K. Zhang, C. van Doorne, J. Fesmire, B. Dindoruk, and V. Balakotaiah. Hydrogen supply chain and challenges in large-scale LH2 storage and transportation. *International Journal of Hydrogen Energy*, 46(47):24149–24168, jul 2021.

[42] S. M. Aceves, F. Espinosa-Loza, E. Ledesma-Orozco, T. O. Ross, A. H. Weisberg, T. C. Brunner, and O. Kircher. High-density automotive hydrogen storage with cryogenic capable pressure vessels. *International Journal of Hydrogen Energy*, 35(3):1219–1226, feb 2010.

[43] Z. Yanxing, G. Maoqiong, Z. Yuan, D. Xueqiang, and S. Jun. Thermodynamics analysis of hydrogen storage based on compressed gaseous hydrogen, liquid hydrogen and cryo-compressed hydrogen. *International Journal of Hydrogen Energy*, 44(31):16833–16840, jun 2019.

[44] R. K. Ahluwalia, T.Q. Hua, J. K. Peng, S. Lasher, K. McKenney, J. Sinha, and M. Gardiner. Technical assessment of cryo-compressed hydrogen storage tank systems for automotive applications. *International Journal of Hydrogen Energy*, 35(9):4171–4184, may 2010.

[45] R. K. Ahluwalia, T.Q. Hua, and J.K. Peng. On-board and off-board performance of hydrogen storage options for light-duty vehicles. *International Journal of Hydrogen Energy*, 37(3):2891–2910, feb 2012.

[46] A. Turnbull. Stress corrosion cracking in metals – mechanisms. In *Reference Module in Materials Science and Materials Engineering*. Elsevier, dec 2015.

[47] N. A. A. Rusman and M. Dahari. A review on the current progress of metal hydrides material for solid-state hydrogen storage applications. *International Journal of Hydrogen Energy*, 41(28):12108–12126, jul 2016.

[48] L. George and S. K. Saxena. Structural stability of metal hydrides, alanates and borohydrides of alkali and alkali- earth elements: A review. *International Journal of Hydrogen Energy*, 35(11):5454–5470, jun 2010.

[49] F. Costanzo, P. L. Silvestrelli, and F. Ancilotto. Physisorption, diffusion, and chemisorption pathways of H_2 molecule on graphene and on (2,2) carbon nanotube by first principles calculations. *Journal of Chemical Theory and Computation*, 8(4):1288–1294, mar 2012.

[50] J. O. Abe, A. P. I. Popoola, E. Ajenifuja, and O. M. Popoola. Hydrogen energy, economy and storage: Review and recommendation. *International Journal of Hydrogen Energy*, 44(29):15072–15086, jun 2019.

[51] X. Li, H. Zang, J. Wang, J. Wang, and H. Zhang. Design of tetraphenyl silsesquioxane based covalent-organic frameworks as hydrogen storage materials. *J. Mater. Chem. A*, 2(43):18554–18561, aug 2014.

[52] J. R. Morse, D. A. Zugell, E. Patterson, J. W. Baldwin, and H. D. Willauer. Hydrogenated graphene: Important material properties regarding its application for hydrogen storage. *Journal of Power Sources*, 494:229734, may 2021.

[53] C. Liu, Q. H. Yang, Y. Tong, H. T. Cong, and H. M. Cheng. Volumetric hydrogen storage in single-walled carbon nanotubes. *Applied Physics Letters*, 80(13):2389–2391, apr 2002.

[54] P. A. Anderson. Storage of hydrogen in zeolites. In *Solid-State Hydrogen Storage*, pages 223–260. Elsevier, 2008.

[55] Z. Abdin and K. R. Khalilpour. Single and polystorage technologies for renewable-based hybrid energy systems. In *Polygeneration with Polystorage for Chemical and Energy Hubs*, pages 77–131. Elsevier, 2019.

[56] Y. Kojima. Hydrogen storage materials for hydrogen and energy carriers. *International Journal of Hydrogen Energy*, 44(33):18179–18192, jul 2019.

[57] H. T. Hwang, A. Al-Kukhun, and A. Varma. Hydrogen for vehicle applications from hydrothermolysis of ammonia borane: Hydrogen yield, thermal characteristics, and ammonia formation. *Industrial & Engineering Chemistry Research*, 49(21):10994–11000, sep 2010.

[58] J. Yang, A. Sudik, C. Wolverton, and D. J. Siegel. High capacity hydrogen storage materials: attributes for automotive applications and techniques for materials discovery. *Chem. Soc. Rev.*, 39(2):656–675, 2010.

[59] Y. Ma, X. R. Wang, T. Li, J. Zhang, J. Gao, and Z.Y. Sun. Hydrogen and ethanol: Production, storage, and transportation. *International Journal of Hydrogen Energy*, 46(54):27330–27348, aug 2021.

[60] Z. Wu, F. Yang, Z. Bao, S. N. Nyamsi, and Z. Zhang. Improvement in hydrogen storage characteristics of mg-based metal hydrides by doping nonmetals with high electronegativity: A first-principle study. *Computational Materials Science*, 78:83–90, oct 2013.

[61] Y. Wang, X. C. Adroher, J. Chen, X. G. Yang, and T. Miller. Three-dimensional modeling of hydrogen sorption in metal hydride hydrogen storage beds. *Journal of Power Sources*, 194(2):997–1006, dec 2009.

[62] S. H. Hong and M. Y. Song. Hydrogen desorption and absorption properties of Pd and MgO or nano-sized ni-added MgH_2 + $LiBH_4$ composites. *Materials Research Bulletin*, 48(9):3453–3458, sep 2013.

[63] R. K. Jain, A. Jain, S. Agarwal, N. P. Lalla, V. Ganesan, D. M. Phase, and I. P. Jain. Hydrogenation behaviour of ce-based AB5 intermetallic compounds. *Journal of Alloys and Compounds*, 440(1-2):84–88, aug 2007.

[64] L. J. Ma, J. Jia, H. S. Wu, and Y. Ren. Ti–η2-(c2h2) and HCC–TiH as high capacity hydrogen storage media. *International Journal of Hydrogen Energy*, 38(36):16185–16192, dec 2013.

[65] M. Reuß, T. Grube, M. Robinius, P. Preuster, P. Wasserscheid, and D. Stolten. Seasonal storage and alternative carriers: A flexible hydrogen supply chain model. *Applied Energy*, 200:290–302, aug 2017.

[66] P. Preuster, C. Papp, and P. Wasserscheid. Liquid organic hydrogen carriers (LOHCs): Toward a hydrogen-free hydrogen economy. *Accounts of Chemical Research*, 50(1):74–85, dec 2016.

[67] CMB Hydroville. How is hydrogen transported. http://hydroville.be/en/waterstof/hoe-transporteer-je-waterstof/, aug 2021.

[68] A. Rodl, C. Wulf, and M. Kaltschmitt. Assessment of selected hydrogen supply chains—factors determining the overall GHG emissions. In *Hydrogen Supply Chains*, pages 81–109. Elsevier, 2018.

[69] N. Bouwkamp, A. Burgunder, D. Casey, A. Elgowainy, L. Fisher, J. Merritt, E. Miller, G. Petitpas, A. Rohatgi, N. Rustagi, J. Simnick, H. Soto, and J. Vickers. Hydrogen delievery technical team roadmap. Technical report, Office of Energy Efficiency & Renewable Energy, jul 2017.

[70] Hydrogen U.S. department of energy and Fuel Cell Technologies Office. Liquid hydrogen delievery. https://www.energy.gov/eere/fuelcells/liquid-hydrogen-delivery, aug 2021.

[71] E. Ohaeri, U. Eduok, and J. Szpunar. Hydrogen related degradation in pipeline steel: A review. *International Journal of Hydrogen Energy*, 43(31):14584–14617, aug 2018.

[72] H. Nykyforchyn, O. Tsyrulnyk, O. Zvirko, and M. Hredil. Role of hydrogen in operational degradation of pipeline steel. *Procedia Structural Integrity*, 28:896–902, 2020.

[73] G. P. Tiwari, A. Bose, J. K. Chakravartty, S. L. Wadekar, M. K. Totlani, R. N. Arya, and R. K. Fotedar. A study of internal hydrogen embrittlement of steels. *Materials Science and Engineering: A*, 286(2):269–281, jul 2000.

[74] M. Iannuzzi, A. Barnoush, and R. Johnsen. Materials and corrosion trends in offshore and subsea oil and gas production. 1(1), jul 2017.

[75] K. Stolzenburg and R. Mubbala. Hydrogen liquefaction report. Technical report, IDEALHY, dec 2013.

[76] Z. Abdin, A. Zafaranloo, A. Rafiee, W. Mérida, W. Lipiński, and K. R. Khalilpour. Hydrogen as an energy vector. *Renewable and Sustainable Energy Reviews*, 120:109620, mar 2020.

[77] I. Staffell, D. Scamman, A. V. Abad, P. Balcombe, P. E. Dodds, P. Ekins, N. Shah, and K. R. Ward. The role of hydrogen and fuel cells in the global energy system. *Energy & Environmental Science*, 12(2):463–491, 2019.

[78] IEA. The future of hydrogen. Technical report, International Energy Agency, Paris, 2019.

[79] A. de Klerk. *Fischer-Tropsch Refining*. Wiley-VCH Verlag GmbH & Co. KGaA, jul 2011.

[80] H. Liu. *Ammonia Synthesis Catalysts: Innovation and Practice*. World Scientific Pub Co. Inc., May 2013.

[81] U.S Energy Information Administration. Hydrogen explained; use of hydrogen. https://www.eia.gov/energyexplained/hydrogen/use-of-hydrogen.php, sep 2021.

[82] Office of Energy Efficiency & Renewable Energy. Hydrogen: A clean, flexible energy carrier. https://www.energy.gov/eere/articles/hydrogen-clean-flexible-energy-carrier, feb 2017.

[83] J. Ogden, A. M. Jaffe, D. Scheitrum, Z. McDonald, and M. Miller. Natural gas as a bridge to hydrogen transportation fuel: Insights from the literature. *Energy Policy*, 115:317–329, apr 2018.

[84] P. E. Dodds, I. Staffell, A. D. Hawkes, F. Li, P. Grunewald, W. McDowall, and P. Ekins. Hydrogen and fuel cell technologies for heating: A review. *International Journal of Hydrogen Energy*, 40(5):2065–2083, feb 2015.

[85] M. Haruta and H. Sano. Catalytic combustion of hydrogen I—its role in hydrogen utilization system and screening of catalyst materials. *International Journal of Hydrogen Energy*, 6(6):601–608, jan 1981.

[86] M. Haruta and H. Sano. Catalytic combustion of hydrogen—III. advantages and disadvantages of a catalytic heater with hydrogen fuel. *International Journal of Hydrogen Energy*, 7(9):737–740, jan 1982.

[87] J. Warnatz, U. Maas, and R. W. Dibble. *Combustion : physical and chemical fundamentals, modeling and simulation, experiments, pollutant formation*. Springer, Berlin, Germany, 2006.

[88] K. Kuo. *Principles of combustion*. John Wiley & Sons, Inc., Hoboken, New Jersey, 2 edition, jan 2005.

[89] V. N. Kondratiev. "combustion". https://www.britannica.com/science/combustion.Accessed22January2022, jan 2022.

[90] S. R. Turns. *An introduction to combustion: concepts and applications*. McGraw-Hill, New York, 3 edition, jan 2012.

[91] A. Williams. Flames. In *A-to-Z Guide to Thermodynamics, Heat and Mass Transfer, and Fluids Engineering*. Begellhouse, feb 2011.

[92] U. Ahmed. *Flame Turbulence Interaction In Premixed Turbulent Combustion*. PhD thesis, School of Mechanical Aerospace and Civil Engineering of The University of Manchester, Manchester, England, sep 2013.

[93] S. Elias. *Encyclopedia of geology*. Academic Press, an imprint of Elsevier, Amsterdam, 2021.

[94] G. P. Smith, D. M. Golden, M. Frenklach, N. W. Moriarty, B. Eiteneer, M. Goldenberg, C. T. Bowman, R. K. Hanson, S. Song, W. C. Gardiner, Jr., V. V. Lissianski, and Z. Qin. The NASA polynomials. http://combustion.berkeley.edu/gri-mech/version30/text30.html, aug 2021.

[95] S. Benaissa, B. Adouane, S. M. Ali, and A. Mohammad. Effect of hydrogen addition on the combustion characteristics of premixed biogas/hydrogen-air mixtures. *International Journal of Hydrogen Energy*, 46(35):18661–18677, may 2021.

[96] R. Li, Z. Luo, T. Wang, F. Cheng, H. Lin, and X. Zhu. Effect of initial temperature and h2 addition on explosion characteristics of H_2-poor/CH_4/air mixtures. *Energy*, 213:118979, dec 2020.

[97] Y. Wang, A. Movaghar, Z. Wang, Z. Liu, W. Sun, F. N. Egolfopoulos, and Z. Chen. Laminar flame speeds of methane/air mixtures at engine conditions: Performance of different kinetic models and power-law correlations. *Combustion and Flame*, 218:101–108, aug 2020.

[98] S. Wang, Z. Wang, Y. He, X. Han, Z. Sun, Y. Zhu, and M. Costa. Laminar burning velocities of $CH_4/O_2/N_2$ and oxygen-enriched $CH_4/O_2/CO_2$ flames at elevated pressures measured using the heat flux method. *Fuel*, 259:116152, jan 2020.

[99] R. W. Francisco and A. M. Oliveira. Measurement of the adiabatic flame speed and overall activation energy of a methane enriched $H_2/CO/CO_2/N_2$ low heating value mixture. *International Journal of Hydrogen Energy*, 45(53):29533–29545, oct 2020.

[100] Mechanical and University of California at San Diego Aerospace Engineering (Combustion Research). Chemical-kinetic mechanisms for combustion applications, san diego mechanism web page. http://combustion.ucsd.edu, 2016. Version 2.5.1.

[101] R. B. Bramlette and C. D. Depcik. Review of propane-air chemical kinetic mechanisms for a unique jet propulsion application. *Journal of the Energy Institute*, 93(3):857–877, jun 2020.

[102] A. I. Korsakova, V. V. Gubernov, A. V. Kolobov, V. Bykov, and U. Maas. Stability of rich laminar hydrogen-air flames in a model with detailed transport and kinetic mechanisms. *Combustion and Flame*, 163:478–486, jan 2016.

[103] C. Xu and A. A. Konnov. Validation and analysis of detailed kinetic models for ethylene combustion. *Energy*, 43(1):19–29, jul 2012.

[104] A. Paykani. Comparative study on chemical kinetics mechanisms for methane-based fuel mixtures under engine-relevant conditions. *Energies*, 14(10):2834, may 2021.

[105] Z. Qin, V. V. Lissianski, H. Yang, W. C. Gardiner, S. G. Davis, and H. Wang. Combustion chemistry of propane: A case study of detailed reaction mechanism optimization. *Proceedings of the Combustion Institute*, 28(2):1663–1669, jan 2000.

[106] W. K. Metcalfe, S. M. Burke, S. S. Ahmed, and H. J. Curran. A hierarchical and comparative kinetic modeling study of C_1 - C_2 hydrocarbon and oxygenated fuels. *International Journal of Chemical Kinetics*, 45(10):638–675, aug 2013.

[107] X. Yang, Z. Peng, Y. Ding, and Y. Du. Temperature and OH concentration measurements by ultraviolet broadband absorption of OH(x) in laminar methane/air premixed flames. *Fuel*, 288:119666, mar 2021.

[108] B. Koroglu, O. M. Pryor, J. Lopez, L. Nash, and S. S. Vasu. Shock tube ignition delay times and methane time-histories measurements during excess CO_2 diluted oxy-methane combustion. *Combustion and Flame*, 164:152–163, feb 2016.

[109] K. Kuppa, A. Goldmann, T. Schoffler, and F. Dinkelacker. Laminar flame properties of C_1-C_3 alkanes/hydrogen blends at gas engine conditions. *Fuel*, 224:32–46, jul 2018.

[110] H. Nakamura, H. Takahashi, T. Tezuka, S. Hasegawa, K. Maruta, and K. Abe. Effects of CO-to-H_2 ratio and diluents on ignition properties of syngas examined by weak flames in a micro flow reactor with a controlled temperature profile. *Combustion and Flame*, 172:94–104, oct 2016.

[111] E. Hu, X. Li, X. Meng, Y. Chen, Y. Cheng, Y. Xie, and Z. Huang. Laminar flame speeds and ignition delay times of methane–air mixtures at elevated temperatures and pressures. *Fuel*, 158:1–10, oct 2015.

[112] P. Boivin. *Reduced-Kinetic Mechanims for Hydrogen and Syngas Combustion Including Autoignition.* PhD thesis, Escuela Politecnica Superior, Sevilla, Spain, dec 2011.

[113] P. Boivin, A. L. Sánchez, and F. A. Williams. Four-step and three-step systematically reduced chemistry for wide-range H_2–air combustion problems. *Combustion and Flame*, 160(1):76–82, jan 2013.

[114] P. Boivin, C. Jiménez, A. L. Sánchez, and F. A. Williams. An explicit reduced mechanism for H_2-air combustion. *Proceedings of the Combustion Institute*, 33(1):517–523, jan 2011.

[115] P. Boivin, C. Jiménez, A. L. Sánchez, and F. A. Williams. A four-step reduced mechanism for syngas combustion. *Combustion and Flame*, 158(6):1059–1063, jun 2011.

[116] B. J. McBride, S. Gordon, and M. A. Reno. Coefficients for calculating thermodynamic and transport properties of indivivual species. Technical report, NASA - National Aeronautics and Space Administration, oct 1993.

[117] A. Burcat and B. Ruscic. Third millenium ideal gas and condensed phase thermochemical database for combustion (with update from active thermochemical tables). Technical report, sep 2005.

[118] H. H. Carstensen and A. M. Dean. Chapter 4 the kinetics of pressure-dependent reactions. In *Comprehensive Chemical Kinetics*, pages 101–184. Elsevier, 2007.

[119] D. G. Goodwin, R. L. Speth, H. K. Moffat, and B. W. Weber. Cantera: An object-oriented software toolkit for chemical kinetics, thermodynamics, and transport processes. https://www.cantera.org, 2021. Version 2.5.1.

[120] R. J. Kee, F. M. Rupley, J. A. Miller, M. E. Coltrin, J. F. Grcar, E. Meeks, H. K. Moffat, A. E. Lutz, G. D. Lewis, M. D. Smooke, J. Warnatz, G. H. Evans, R. S. Larson, R. E. Mitchell, L. R. Petzold, W. C. Reynolds, M. Caracotsios, W. E. Stewart, P. Glarborg, C. Wang, and O. Adigun. Transport, a software package for the evaluation of gas-phase, multicomponent transport properties. Technical report, CHEMKIN Collection, San Diego, 2000.

[121] M. R. Riazi. Chapter 8—Applications: Estimation of transport properties. In *Characterization and Properties of Petroleum Fractions*, pages 329–329–36. ASTM International, jan 2015.

[122] Y. Liu, T. Wall, S. Khare, and R. Gupta. Oxy-fuel heat transfer characteristics and impacts on boiler design. In *Oxy-Fuel Combustion for Power Generation and Carbon Dioxide (CO2) Capture*, pages 166–194. Elsevier, 2011.

[123] S. Gordon and B. J. McBride. Computer program for calculation of complex chemical equilibrium compositions and applications. part 1: Analysis. Technical report, NASA - National Aeronautics and Space Administration, oct 1994.

[124] C. T. Chong and J. H. Ng. Combustion performance of biojet fuels. In *Biojet Fuel in Aviation Applications*, pages 175–230. Elsevier, 2021.

[125] Rubenildo Vieira Andrade, Laura Andrea Cortabarria Castañeda, Diego Mauricio Yepes Maya, Paulo Sergio Pedroso Cesar Corrêa Junior, Luis Roberto Mello e Pinto, Electo Eduardo Silva Lora, Cristina Aparecida Vilas Bôas de Sales Oliveira, and Bruno Augusto Pinto. Assessment of laminar flame velocity of producer gas from biomass gasification using the bunsen burner method. *International Journal of Hydrogen Energy*, 45(20):11559–11568, apr 2020.

[126] Akshay A. Kadam, Abhinandan D. Kadam, Nikhil P. Daphale, and M. Sreedhar Babu. Experimental measurement of laminar flame velocities of LPG–air mixtures with cylindrical flame tube method. In *Recent Advances in Mechanical Infrastructure*, pages 297–303. Springer Singapore, 2021.

[127] R.A. Strehlow and Joseph G. Stuart. An improved soap bubble method of measuring flame velocities. *Symposium (International) on Combustion*, 4(1):329–336, jan 1953.

[128] D. Razus, D. Oancea, and N. I. Ionescu . Burning velocity determination by spherical bomb technique. ii: Propylene-air mixtures of various compositions, pressures and temperatures. *Revue Roumaine de Chimie*, 45:319–330, 04 2000.

[129] O. A. Powell, P. Papas, and C. Dreyer. Laminar burning velocities for hydrogen-, methane-, acetylene-, and propane-nitrous oxide flames. *Combustion Science and Technology*, 181(7):917–936, jun 2009.

[130] I. Glassman, R. A. Yetter, and N. G. Glumac. *Combustion*. Academic Press, Amsterdam, 5 edition, 2014.

[131] R. J. Kee, M. E. Coltrin, P. Glarborg, and H. Zhu. Laminar flames. In Wiley, editor, *Chemically Reacting Flow: Theory, Modeling, and Simulation.*, chapter chapter 15, pages 521–547. Wiley, sep 2017.

[132] E. Shashi Menon. Fluid flow in pipes. In *Transmission Pipeline Calculations and Simulations Manual*, pages 149–234. Elsevier, 2015.

[133] D. Vozone. Master thesis-flashback and blowoff stability analysis of hydrogen enriched natural gas using bunsen flames, jul 2021.

[134] C. K. Law, A. Makino, and T. Lu. On the off-stoichiometric peaking of adiabatic flame temperature. *Combustion and Flame*, 145(4):808–819, jun 2006.

[135] C. M. White, R. Steeper, and A. Lutz. The hydrogen-fueled internal combustion engine: a technical review. *International Journal of Hydrogen Energy*, 31(10):1292–1305, aug 2006.

[136] R. Hellmann, E. Bich, E. Vogel, A. S. Dickinson, and V. Vesovic. Calculation of the transport and relaxation properties of methane. II. thermal conductivity, thermomagnetic effects, volume viscosity, and nuclear-spin relaxation. *The Journal of Chemical Physics*, 130(12):124309, mar 2009.

[137] J. B. Mehl, M. L. Huber, and A. H. Harvey. Ab initio transport coefficients of gaseous hydrogen. *International Journal of Thermophysics*, 31(4-5):740–755, jan 2010.

[138] Yin Li, Christopher P. Alaimo, Minji Kim, Norman Y. Kado, Joshua Peppers, Jian Xue, Chao Wan, Peter G. Green, Ruihong Zhang, Bryan M. Jenkins, Christoph F. A. Vogel, Stefan Wuertz, Thomas M. Young, and Michael J. Kleeman. Composition and toxicity of biogas produced from different feedstocks in california. *Environmental Science & Technology*, 53(19):11569–11579, sep 2019.

[139] O. C. Kwon and G. M. Faeth. Flame/stretch interactions of premixed hydrogen-fueled flames: measurements and predictions. *Combustion and Flame*, 124(4):590–610, mar 2001.

[140] T. G. Scholte and P. B. Vaags. Burning velocities of mixtures of hydrogen, carbon monoxide and methane with air. *Combustion and Flame*, 3:511–524, jan 1959.

[141] C. Dong, Q. Zhou, Q. Zhao, Y. Zhang, T. Xu, and S. Hui. Experimental study on the laminar flame speed of hydrogen/carbon monoxide/air mixtures. *Fuel*, 88(10):1858–1863, oct 2009.

[142] M. Ilbas, A. Crayford, I. Yilmaz, P. Bowen, and N. Syred. Laminar-burning velocities of hydrogen–air and hydrogen–methane–air mixtures: An experimental study. *International Journal of Hydrogen Energy*, 31(12):1768–1779, sep 2006.

[143] K. T. Aung, M. I. Hassan, and G. M. Faeth. Flame stretch interactions of laminar premixed hydrogen/air flames at normal temperature and pressure. *Combustion and Flame*, 109(1-2):1–24, apr 1997.

[144] B. J. Zhong, Z. M. Zeng, and H. S. Peng. The pressure dependence of laminar flame speed of 2-methyl-2-butene/air flames in the 0.1–1.0 MPa range. *Combustion Science and Technology*, 190(11):1886–1899, may 2018.

[145] K. T. Aung, M. I. Hassan, and G. M. Faeth. Effects of pressure and nitrogen dilution on flame/stretch interactions of laminar premixed h2/o2/n2 flames. *Combustion and Flame*, 112(1-2):1–15, jan 1998.

[146] M. Kuznetsov, S. Kobelt, J. Grune, and T. Jordan. Flammability limits and laminar flame speed of hydrogen–air mixtures at sub-atmospheric pressures. *International Journal of Hydrogen Energy*, 37(22):17580–17588, nov 2012.

[147] E. Hu, Z. Huang, J. He, and H. Miao. Experimental and numerical study on laminar burning velocities and flame instabilities of hydrogen–air mixtures at elevated pressures and temperatures. *International Journal of Hydrogen Energy*, 34(20):8741–8755, oct 2009.

[148] M. Baloo, B. M. Dariani, M. Akhlaghi, and M. AghaMirsalim. Effects of pressure and temperature on laminar burning velocity and flame instability of iso-octane/methane fuel blend. *Fuel*, 170:235–244, apr 2016.

[149] K. J. Bosschaart and L. P. H. de Goey. The laminar burning velocity of flames propagating in mixtures of hydrocarbons and air measured with the heat flux method. *Combustion and Flame*, 136(3):261–269, feb 2004.

[150] C. M. Vagelopoulos and F. N. Egolfopoulos. Direct experimental determination of laminar flame speeds. *Symposium (International) on Combustion*, 27(1):513–519, jan 1998.

[151] O. Park, P. S. Veloo, N. Liu, and F. N. Egolfopoulos. Combustion characteristics of alternative gaseous fuels. *Proceedings of the Combustion Institute*, 33(1):887–894, 2011.

[152] N. Donohoe, A. Heufer, W. K. Metcalfe, H. J. Curran, M. L. Davis, O. Mathieu, D. Plichta, A. Morones, E. L. Petersen, and F. Guthe. Ignition delay times, laminar flame speeds, and mechanism validation for natural gas/hydrogen blends at elevated pressures. *Combustion and Flame*, 161(6):1432–1443, jun 2014.

[153] E. Hu, Z. Huang, J. He, C. Jin, and J. Zheng. Experimental and numerical study on laminar burning characteristics of premixed methane–hydrogen–air flames. *International Journal of Hydrogen Energy*, 34(11):4876–4888, jun 2009.

[154] B. Viswanathan. Natural gas. In *Energy Sources*, pages 59–79. Elsevier, 2017.